

Efficient computation of Fourier-Bessel transforms for transverse-momentum dependent parton distributions and other functions

Markus Diehl and Oskar Grocholski

Deutsches Elektronen-Synchrotron DESY, Notkestr. 85, 22607 Hamburg, Germany

We present a method for the numerical computation of Fourier-Bessel transforms on a finite or infinite interval. The function to be transformed needs to be evaluated on a grid of points that is independent of the argument of the Bessel function. We demonstrate the accuracy of the algorithm for a wide range of functions, including those that appear in the context of transverse-momentum dependent parton distributions in Quantum Chromodynamics.

arXiv:2405.08616v2 [hep-ph] 20 Aug 2024

Contents

1	Introduction	3
2	Developing the method	4
2.1	The original Levin method	4
2.2	Rescaling: general form	5
2.3	Rescaling with $r(z) = z$	6
2.3.1	Solution if f_1 or f_2 are powers of z	7
2.3.2	Behaviour of solutions at large z	9
3	Final form of the method	10
3.1	Behaviour of solutions at small and large z	11
3.2	Discretisation on Chebyshev grids	13
3.2.1	Solving the linear equation system	16
3.2.2	Examples of variable transforms	17
3.3	Summary of the algorithm	18
3.4	Implementation in BestLime	19
4	Numerical studies	19
4.1	Control parameters for solving the linear equation system	19
4.2	Benchmarks: grids and precision	22
4.3	Computation time	24
5	Numerical studies for TMD-like functions	25
5.1	Integrands	25
5.2	Choosing interpolation grids	29
5.2.1	Variable transformations	30
5.2.2	Number of subgrids	30
5.2.3	Transformation parameters and number of grid points	30
5.3	Estimating the integration error	35
5.4	Comparison with the method of Kang et al.	35
6	Formally divergent integrals	40
6.1	Defining the integral	43
6.2	Numerical accuracy	45
7	Summary	48
A	Useful relations for Bessel and Lommel functions	49
A.1	Bessel functions	49
A.2	Lommel functions	50
B	Integrands with a Gaussian decrease in z	52
C	Chebyshev interpolation	53
D	Fourier-Bessel integrals as distributions	55
	References	56

1 Introduction

The Fourier-Bessel transform — also known as Hankel transform — appears in many branches of physics; in particular it arises from the multi-dimensional Fourier transform of functions with rotational symmetry. It has the form

$$I(q) = \int_{z_a}^{z_b} dz J_\nu(qz) \tilde{f}(z), \quad (1.1)$$

where J_ν is a Bessel function of the first kind. In general the integration runs from 0 to ∞ , but it may be reduced to a finite interval by the support properties of $\tilde{f}(z)$.

In Quantum Chromodynamics, the Fourier-Bessel transform prominently appears in the context of transverse-momentum dependent parton distributions (TMDs), where cross sections are proportional to integrals of the form (1.1) with $\nu = 0, 1, 2, 3$ and $\tilde{f}(z)$ equal to $z^{\nu+1}$ times the product of two TMDs,¹ see e.g. section 2.11 in [1]. The integration limits are 0 and ∞ in that case. The method proposed in [2] involves similar integrals over TMDs from 0 to some finite value, and from that finite value to ∞ . A more involved application is given by two-parton TMDs, which appear in the description of double parton scattering [3]. In this case, two nested Fourier transforms occur, the radial parts of which can be converted into two nested Fourier-Bessel integrals, $\int dz_1 \int dz_2 J_{\nu_1}(q_1 z_1) J_{\nu_2}(q_2 z_2) \tilde{f}(z_1, z_2)$.

In the cases just mentioned, one typically needs to compute the transform (1.1) for many settings of external parameters, namely longitudinal parton momentum fractions and hard scales. For uncertainty estimates on TMDs fitted to data (using the Hessian method or replicas) one must repeat the calculation for many TMD sets. The numerical computation of the integrands itself can be rather costly; at small transverse distances z it involves Mellin convolutions in the longitudinal momentum fractions, with lengthy kernels at higher perturbative orders (see section 2.8 in [1] and references therein).

In the TMD context, the variable q in (1.1) is a measured transverse momentum, for instance of the produced lepton pair in the Drell-Yan process. The process to be described is characterised by a hard scale Q , which can range from a few GeV for semi-inclusive deep inelastic scattering or non-resonant Drell-Yan production to about 100 GeV for the production of a W , Z , or Higgs boson. For the production of a pair of such bosons, the hard scale Q is given by the invariant mass of the pair and can be significantly larger. The TMD formalism describes cross sections in the region $q \ll Q$, whilst a description in terms of conventional collinear parton distributions is adequate for $q \sim Q$. A smooth transition between the two regimes typically requires evaluating the TMD expression for q up to order Q , see section 4.7 in [1] for an overview and [4] for a recent example.

In summary, the calculation of cross sections with TMDs may involve a large number of Fourier-Bessel transforms of complicated functions for a possibly wide range of q values. In such a scenario, integration methods with nodes that depend on q come at a rather high computational cost since the integrand needs to be computed many times. This is the case for the method of Ogata [5], which is used for TMDs for instance in the codes `artemide` [6] or `ResBos2` [7], the latter employing the algorithm of Kang et al. [8].² A method using fixed nodes in z for a whole set of q values is the discrete Hankel transform, see [9, 10] for a mathematical description and [11] for an application in hadron physics. Accessing high q requires a large number of nodes in this method.

In the present work, we adapt a method for oscillatory integrands due to Levin [12, 13] to the specific case of Fourier-Bessel transforms. We show that high accuracy can be achieved

¹We note that in the TMD literature, the spatial distance is usually called b rather than z .

²The respective codes and documentation can be found at <https://github.com/VladimirovAlexey/artemide-public> for [6] and at <https://github.com/UCLA-TMD/Ogata> and <https://ucla-tmd.github.io/Ogata> for [8].

by combining this method with Chebyshev interpolation (which was already done in [14, 15], albeit not for Bessel weighted integrals). Specifically, we present a method to compute integrals of the form

$$I(q) = \int_{z_a}^{z_b} dz J_\nu(qz) \left(\frac{1+z}{z} \right)^\nu f(z), \quad \nu \geq 0, \quad q > 0, \quad z_a < z_b \quad (1.2)$$

with the following specifications:

- z_a may be zero or positive, and z_b may be finite or ∞ .
We find that it can be useful for both accuracy and computation time to evaluate the integral over $z \in [0, \infty]$ as the sum of integrals over two or more subintervals.
- ν may be integer or non-integer. Notice that for half integer ν , the integral (1.2) can be rewritten in terms of the spherical Bessel functions $j_n(x) = \sqrt{\pi/(2x)} J_{n+1/2}(x)$.
- $f(z)$ must be finite on the full integration interval, including the end points z_a and z_b . To obtain accurate integrals, $f(z)$ should be sufficiently smooth and not have fast oscillations. We will see that a non-analytic behaviour like $f(z) \sim z^{1-\delta}$ at $z = 0$ is amenable to the method if δ is not too large, although the accuracy tends to degrade with increasing δ .
- The function $f(z)$ is evaluated on a discrete set of n points from z_a to z_b (specified in section 3.2). We find that with a suitable choice of discretisation grid, good integration accuracy can be obtained for a rather wide range of q .

We have implemented this method in a C++ library named BESTLIME,³ which can be downloaded from [16] and is briefly discussed in sections 3.4 and 4.3 of the present paper. Although our primary physics motivation is the application to TMDs, we think that the method may be of interest to other domains. We show in section 4.2 that it can handle a large variety of functions $f(z)$.

Our paper is organised as follows. In section 2 we develop our method starting from the original one in [13], and in section 3 we present its final form. We discuss general numerical aspects in section 4 and integrals appearing in TMD cross sections in section 5. In section 6 we consider integrals from 0 to ∞ that do not converge but can be defined in the distributional sense. Our findings are summarised in section 7. Various mathematical details are given in appendix A to appendix D.

2 Developing the method

2.1 The original Levin method

To begin with, let us present the original method of Levin [13] for the case of Fourier-Bessel integrals. We use a slightly different notation than the cited work. The integral to be evaluated has the form

$$I(q) = \int_{z_a}^{z_b} dz \left[\tilde{\omega}_1(z, q) \tilde{f}_1(z) + \tilde{\omega}_2(z, q) \tilde{f}_2(z) \right] \quad (2.1)$$

with weights

$$\tilde{\omega}_1(z, q) = J_\nu(qz), \quad \tilde{\omega}_2 = J_{\nu+1}(qz), \quad (2.2)$$

³Bessel transformation with Levin's integration method.

where it is assumed that the functions $\tilde{f}_1(z)$ and $\tilde{f}_2(z)$ are *not* strongly oscillating. The Fourier-Bessel transform (1.1) is obtained by setting $\tilde{f}_1 = \tilde{f}$ and $\tilde{f}_2 = 0$. Setting $\tilde{f}_1 = 0$ and $\tilde{f}_2 = \tilde{f}$ instead, one obtains the analogue of (1.1) for $J_{\nu+1}$ instead of J_ν . This requires only a minor additional computational effort; a bonus that is preserved by our adaptation of Levin's method.

To proceed, we introduce the vector notation

$$\tilde{\omega} = (\tilde{\omega}_1, \tilde{\omega}_2)^T, \quad \tilde{\mathbf{f}} = (\tilde{f}_1, \tilde{f}_2)^T, \quad (2.3)$$

where a superscript T denotes transposition. Using the relations (A.1), one readily derives

$$\frac{d}{dz} \tilde{\omega}(z, q) = \tilde{A}^T(z, q) \cdot \tilde{\omega}(z, q) \quad (2.4)$$

with the matrix

$$\tilde{A}(z, q) = \begin{pmatrix} \nu/z, & q \\ -q, & -(\nu+1)/z \end{pmatrix}. \quad (2.5)$$

If one finds a solution for the system

$$\tilde{\mathbf{f}}(z) = \left[\frac{d}{dz} + \tilde{A}(z, q) \right] \tilde{\mathbf{h}}(z, q) \quad (2.6)$$

of ordinary differential equations (ODEs), one can evaluate the integral as

$$I(q) = \int_{z_a}^{z_b} dz \tilde{\omega}^T(z, q) \cdot \tilde{\mathbf{f}}(z) = \left[\tilde{\omega}^T(z, q) \cdot \tilde{\mathbf{h}}(z, q) \right]_{z_a}^{z_b}, \quad (2.7)$$

where we use the common notation

$$\left[F(z, q) \right]_{z_a}^{z_b} = F(z_b, q) - F(z_a, q). \quad (2.8)$$

This is readily seen by inserting (2.6) in the first expression of (2.7), integrating by parts, and then using (2.4).

As argued in [12, 13], the system (2.6) has one particular solution with functions $\tilde{h}_i(z, q)$ that are not rapidly oscillating. One can find this solution by collocation, which consists in approximating $\tilde{h}_1(z, q)$ and $\tilde{h}_2(z, q)$ by a linear combination of n basis functions $b_i(z)$ and by determining the coefficients of these functions by evaluating the system (2.6) at a set of n suitably chosen collocation points z_i . This yields a coupled system of linear equations that can be solved by standard linear algebra methods (see section 3.2.1 for details). For the method to give accurate results, it is essential that the approximation of \tilde{h}_1 and \tilde{h}_2 is sufficiently precise, in particular at the end points z_a and z_b , where these functions are evaluated in the final result (2.7).

As it stands, this method is not suitable for a lower integration boundary $z_a = 0$, where the diagonal elements of \tilde{A} diverge. We circumvent this problem by rescaling, as described in the next subsection.

2.2 Rescaling: general form

The representation (2.7) of $I(q)$ remains valid if one replaces $\tilde{\mathbf{f}}$, $\tilde{\mathbf{h}}$ and $\tilde{\omega}$ by the rescaled functions

$$\begin{aligned} \mathbf{f}(z) &= r^\nu(z) \tilde{\mathbf{f}}(z), & \mathbf{h}(z) &= r^\nu(z) \tilde{\mathbf{h}}(z), \\ \omega(z, q) &= r^{-\nu}(z) \tilde{\omega}(z, q), \end{aligned} \quad (2.9)$$

where $r(z)$ will be specified below. Using the explicit form (2.5) of \tilde{A} , one can rewrite the system of ODEs (2.6) as

$$\begin{aligned} f_1 &= \frac{d}{dz} h_1 + qh_2 + \nu \left[\frac{1}{z} - \frac{r'}{r} \right] h_1, \\ f_2 &= \frac{d}{dz} h_2 - qh_1 - \left[\frac{\nu + 1}{z} + \nu \frac{r'}{r} \right] h_2, \end{aligned} \quad (2.10)$$

where we have omitted the arguments z or (z, q) of the functions and abbreviated $r' = dr/dz$. The singularity at $z = 0$ in the first equation of (2.10) is removed if

$$r(z) \sim z \quad \text{for } z \rightarrow 0, \quad (2.11)$$

and the singularity in the second equation is avoided by setting

$$h_2(z, q) = r(z) h_3(z, q). \quad (2.12)$$

The final form of the ODE system then reads

$$\begin{aligned} f_1 &= \frac{d}{dz} h_1 + qr h_3 + \nu \left[\frac{1}{z} - \frac{r'}{r} \right] h_1, \\ f_2 &= r \frac{d}{dz} h_3 - qh_1 - \left[(\nu + 1) \frac{r}{z} + (\nu - 1) r' \right] h_3, \end{aligned} \quad (2.13)$$

and the integral $I(q)$ is given by

$$\begin{aligned} I(q) &= \int_{z_a}^{z_b} dz r^{-\nu}(z) \left[J_\nu(qz) f_1(z) + J_{\nu+1}(qz) f_2(z) \right] \\ &= \left[J_\nu(qz) r^{-\nu}(z) h_1(z, q) + J_{\nu+1}(qz) r^{-\nu+1}(z) h_3(z, q) \right]_{z_a}^{z_b}. \end{aligned} \quad (2.14)$$

We will show that if $f_1(z)$ and $f_2(z)$ are sufficiently well-behaved at $z \rightarrow 0$, the solutions $h_1(z, q)$ and $h_3(z, q)$ of (2.13) are well behaved at $z \rightarrow 0$ as well. This enables one to solve the system by collocation with basis functions that have a Taylor expansion in z around $z = 0$. We anticipate that our method will use basis functions with this property, postponing details to section 3.2.

2.3 Rescaling with $r(z) = z$

The main purpose of this subsection is to explicitly solve the system (2.13) of ODEs for particular choices of f_1 and f_2 . This is an intermediate step, and a reader mainly interested in final version of our method may skip forward to section 3.

In the present subsection, we set

$$r(z) = z, \quad (2.15)$$

such that the system of ODE takes the rather simple form

$$f_1 = \frac{d}{dz} h_1 + qz h_3, \quad (2.16)$$

$$f_2 = z \frac{d}{dz} h_3 - qh_1 - 2\nu h_3. \quad (2.17)$$

One can eliminate h_1 by taking the derivative of (2.17) and then inserting dh_1/dz from (2.16). The result is

$$z^2 \frac{d^2}{dz^2} (z^{-\nu} h_3) + z \frac{d}{dz} (z^{-\nu} h_3) + (q^2 z^2 - \nu^2) (z^{-\nu} h_3) = z^{1-\nu} (qf_1 + f_2') \quad (2.18)$$

with $f_2' = df_2/dz$.

If one sets $f_1 = f_2 = 0$, this is the Bessel equation for the function $z^{-\nu} h_3$. The *homogeneous* solution of equations (2.16) and (2.17) is therefore given by

$$\begin{pmatrix} h_1 \\ h_3 \end{pmatrix} \Big|_{\text{hom}} = c_J \begin{pmatrix} -(qz)^{\nu+1} J_{\nu+1}(qz) \\ q (qz)^\nu J_\nu(qz) \end{pmatrix} + c_Y \begin{pmatrix} -(qz)^{\nu+1} Y_{\nu+1}(qz) \\ q (qz)^\nu Y_\nu(qz) \end{pmatrix} \quad (2.19)$$

with arbitrary coefficients c_J and c_Y , where Y_ν denotes the Bessel functions of the second kind. We obtained the solution for h_1 by inserting the one for h_3 into (2.17) and using the relations (A.1) and (A.2).

At small z , the Bessel functions J_ν and Y_ν can be represented as sums of different power series in z^2 , some of which are multiplied by functions of z . To represent this in a compact form, we write

$$\sigma(x) = \sum_{k=0}^{\infty} a_k x^k \quad (2.20)$$

to denote a power series in the variable x . It is understood that the series may terminate, so that one has a polynomial in x . We use the notation (2.20) in a similar way as the familiar symbol $\mathcal{O}(x)$, i.e., different occurrences of $\sigma(x)$ (even within a single formula) may have different coefficients a_k , and these coefficients may depend on variables other than x (such as q and ν in our context).

With this notation, the Bessel functions can be written in the form (A.6), which implies a small- z behaviour

$$\begin{pmatrix} h_1 \\ h_3 \end{pmatrix} \Big|_{\text{hom}} = \begin{pmatrix} \sigma(z^2) + z^{2\nu+2} \sigma(z^2) + z^{2\nu+2} \ln(z) \sigma(z^2) \\ \sigma(z^2) + z^{2\nu} \sigma(z^2) + z^{2\nu} \ln(z) \sigma(z^2) \end{pmatrix} \quad (2.21)$$

of the homogeneous solution (2.19), where we assumed $\nu \geq 0$. The terms with $\ln(z)$ only appear for integer values of ν . We see that the homogeneous solutions are non-analytic at $z = 0$, except for half-integer ν . Recalling that the basis functions we will use for collocation have a Taylor expansion around $z = 0$, we require

$$\nu \geq 1 \quad (2.22)$$

when using (2.14), which ensures that the functions (2.21) and their first derivatives in z are finite at that point. Integrals with J_ν for $\nu < 1$ can be evaluated using integration by parts, as specified in equation (3.5) below.

2.3.1 Solution if f_1 or f_2 are powers of z

Let us first consider the case where $f_2 = 0$ and

$$f_1(z) = c_1 z^{\mu+\nu}, \quad (2.23)$$

which corresponds to the integral of $c_1 z^\mu J_\nu(qz)$ in (2.14). Notice that a finite value of $f_1(z)$ at $z = 0$ requires $\mu + \nu \geq 0$.

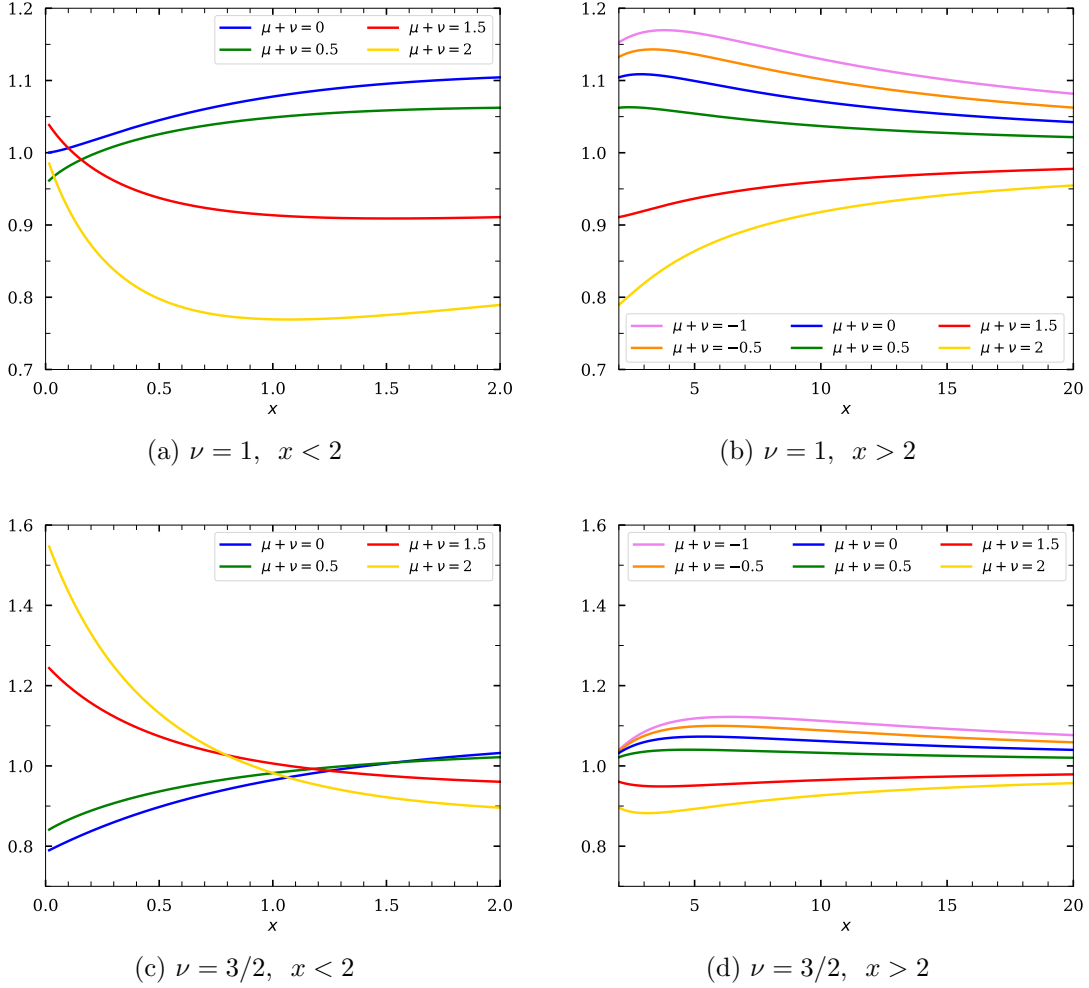


Figure 1: Lommel functions of the second kind, scaled as specified in (2.24). The functions for $\mu + \nu = 1$ are not shown, since according to (A.17) they are identical to 1.

The r.h.s. of (2.18) now equals $c_1 q z^{1+\mu}$, and we recognise the Lommel differential equation (A.10) for the function $z^{-\nu} h_3$ (up to a constant on the r.h.s.). The equation is solved by $c_1 q^{-\mu}$ times the Lommel functions of the first or second kind, $s_{\mu,\nu}(qz)$ or $S_{\mu,\nu}(qz)$, which differ by a linear combination $c_J J_\nu(qz) + c_Y Y_\nu(qz)$ of the homogeneous solutions, see (A.12).

It turns out that it is the Lommel functions of the second kind that are free of fast oscillations in z . This is illustrated for selected values of μ and ν in figure 1. In the plots, we have scaled the functions as

$$x^\nu (1+x)^{1-\mu-\nu} S_{\mu,\nu}(x) \quad (2.24)$$

for clarity. According to (A.19) the scaled functions tend to 1 for $x \rightarrow \infty$, and according to (A.24) they have a finite limit for $x \rightarrow 0$ if $\mu + \nu \geq 0$ and $\nu \geq 1$.

The corresponding solution for h_1 is readily obtained by inserting the one for h_3 into (2.17). Using the relations (A.14), we obtain

$$\begin{pmatrix} h_1 \\ h_3 \end{pmatrix} \Big|_{f_1} = \tilde{c}_1 \begin{pmatrix} (\mu - \nu - 1)(qz)^{\nu+1} S_{\mu-1,\nu+1}(qz) \\ q(qz)^\nu S_{\mu,\nu}(qz) \end{pmatrix} \quad (2.25)$$

with $\tilde{c}_1 = c_1 q^{-\mu-\nu-1}$.

We now turn to the case where $f_1 = 0$ and

$$f_2(z) = c_2 z^{\mu+\nu}, \quad (2.26)$$

which corresponds to the integral of $c_2 z^\mu J_{\nu+1}(qz)$ in (2.14). The r.h.s. of (2.18) then equals $(\mu + \nu) c_2 z^\mu$, and the equation is again solved by Lommel functions, but with the first index decreased by 1 and with a different overall factor:

$$\begin{pmatrix} h_1 \\ h_3 \end{pmatrix} \Big|_{f_2} = (\mu + \nu) \tilde{c}_2 \begin{pmatrix} (\mu - \nu - 2) (qz)^{\nu+1} S_{\mu-2, \nu+1}(qz) \\ q (qz)^\nu S_{\mu-1, \nu}(qz) \end{pmatrix} - \tilde{c}_2 \begin{pmatrix} (qz)^{\mu+\nu} \\ 0 \end{pmatrix} \quad (2.27)$$

where $\tilde{c}_2 = c_2 q^{-\mu-\nu-1}$. The solution for $\mu + \nu = 0$ is trivial to verify.

By virtue of (A.24), the functions in (2.25) and (2.27) have series expansions

$$\begin{pmatrix} h_1 \\ h_3 \end{pmatrix} \Big|_{f_1} = \begin{pmatrix} \sigma(z^2) + z^{\mu+\nu+1} \sigma(z^2) + z^{2\nu+2} \sigma(z^2) + z^{2\nu+2} \ln(z) \sigma(z^2) \\ \sigma(z^2) + z^{\mu+\nu+1} \sigma(z^2) + z^{2\nu} \sigma(z^2) + z^{2\nu} \ln(z) \sigma(z^2) \end{pmatrix} \quad (2.28)$$

and

$$\begin{pmatrix} h_1 \\ h_3 \end{pmatrix} \Big|_{f_2} = \begin{pmatrix} \sigma(z^2) + z^{\mu+\nu} \sigma(z^2) + z^{2\nu+2} \sigma(z^2) + z^{2\nu+2} \ln(z) \sigma(z^2) \\ \sigma(z^2) + z^{\mu+\nu} \sigma(z^2) + z^{2\nu} \sigma(z^2) + z^{2\nu} \ln(z) \sigma(z^2) \end{pmatrix}, \quad (2.29)$$

respectively. In addition to terms already present in the homogeneous solution (2.21), we thus have a further power series in each function h_1 and h_3 , with a prefactor $z^{\mu+\nu+1}$ for f_1 and a prefactor $z^{\mu+\nu}$ for f_2 .

This implies that the power $\mu + \nu$ of z in (2.23) or (2.26) must be large enough if h_1 and h_3 are to be sufficiently well approximated by basis functions that have a Taylor expansion around $z = 0$. In particular, a finite first derivative of h_1 and h_3 at $z = 0$ requires $\mu + \nu \geq 0$ for f_1 and $\mu + \nu \geq 1$ for f_2 .

2.3.2 Behaviour of solutions at large z

We now turn to the behaviour of the functions h_1 and h_3 in the limit $z \rightarrow \infty$. If $f_1(z)$ or $f_2(z)$ is proportional to $z^{\mu+\nu}$, we can use the solutions (2.25) or (2.27) derived in the previous subsection. According to (A.19), they behave like

$$\begin{pmatrix} h_1 \\ h_3 \end{pmatrix} \Big|_{f_1} = \begin{pmatrix} z^{\mu+\nu-1} \sigma(z^{-2}) \\ z^{\mu+\nu-1} \sigma(z^{-2}) \end{pmatrix}, \quad \begin{pmatrix} h_1 \\ h_3 \end{pmatrix} \Big|_{f_2} = \begin{pmatrix} z^{\mu+\nu} \sigma(z^{-2}) \\ z^{\mu+\nu-2} \sigma(z^{-2}) \end{pmatrix} \quad (2.30)$$

for $z \gg 1$. We postpone the discussion of this result to section 3.1.

Let us now consider functions with an exponential falloff in z , namely

$$f_1(z) = c_1 z^{\mu+\nu} \exp(-\kappa z), \quad f_2(z) = c_2 z^{\mu+\nu} \exp(-\kappa z). \quad (2.31)$$

with $\kappa > 0$. To solve the system of ODEs in (2.16) and (2.17), we make the ansatz

$$h_i(z, q) = \hat{h}_i(z, q) \exp(-\kappa z) \quad (i = 1, 3). \quad (2.32)$$

This leads to the new system

$$\begin{pmatrix} c_1 z^{\mu+\nu} \\ c_2 z^{\mu+\nu} \end{pmatrix} = - \begin{pmatrix} \kappa & -q \\ q & \kappa \end{pmatrix} \cdot \begin{pmatrix} \hat{h}_1 \\ z \hat{h}_3 \end{pmatrix} + \begin{pmatrix} d\hat{h}_1/dz \\ z d\hat{h}_3/dz - 2\nu \hat{h}_3 \end{pmatrix}, \quad (2.33)$$

which can be solved with the ansatz

$$\begin{aligned}\hat{h}_1(z, q) &= z^{\mu+\nu} \sum_{k=0}^{\infty} b_{1,k}(q) z^{-k}, \\ \hat{h}_3(z, q) &= z^{\mu+\nu-1} \sum_{k=0}^{\infty} b_{3,k}(q) z^{-k}.\end{aligned}\tag{2.34}$$

For every single k in the sums, the first term on the r.h.s. of (2.33) is leading at large z , whereas the second term on the r.h.s. is down by one power of z . For the leading coefficients, we readily get

$$\begin{pmatrix} b_{1,0} \\ b_{3,0} \end{pmatrix} = -\frac{1}{\kappa^2 + q^2} \begin{pmatrix} \kappa & q \\ -q & \kappa \end{pmatrix} \cdot \begin{pmatrix} c_1 \\ c_3 \end{pmatrix},\tag{2.35}$$

whereas the subleading coefficients can be obtained recursively as

$$\begin{pmatrix} b_{1,k+1} \\ b_{3,k+1} \end{pmatrix} = \frac{1}{\kappa^2 + q^2} \begin{pmatrix} \kappa & q \\ -q & \kappa \end{pmatrix} \cdot \begin{pmatrix} (\mu + \nu - k) b_{1,k} \\ (\mu - \nu - 1 - k) b_{3,k} \end{pmatrix},\tag{2.36}$$

starting with $k = 0$.

The upshot of this calculation is that if the functions f_1 and f_2 are of the form ‘‘power times exponential’’ at large z , then the solutions at large z have the same form, with the same damping factor κ in the exponential.

In appendix B we show that a similar statement holds if f_1 and f_2 have a Gaussian decrease in z (possibly modified by a power and an exponential in z).

3 Final form of the method

In the previous section, we have shown that the rescaling function $r(z) = z$ leads to well behaved solutions h_1 and h_3 of the differential equations (2.13) in the limit $z = 0$. This choice is however not optimal for the opposite limit $z \rightarrow \infty$, where the requirement that the functions f_1 and f_2 in (2.14) must remain finite at the end points of the integration interval would reduce the class of integrals that can be evaluated. Our final choice of rescaling functions is therefore

$$r(z) = \frac{z}{1+z},\tag{3.1}$$

which interpolates smoothly between the choice $r(z) = z$ at small z and no rescaling as $z \rightarrow \infty$. A more general version would be $r(z) = z/(1 + \alpha z)$ with $\alpha > 0$, but we shall not explore this option here.

We can then compute the integral

$$I(q) = \int_{z_a}^{z_b} dz \left(\frac{1+z}{z} \right)^\nu \left[J_\nu(qz) f_1(z) + J_{\nu+1}(qz) f_2(z) \right]\tag{3.2}$$

as

$$I(q) = \left[J_\nu(qz) \left(\frac{1+z}{z} \right)^\nu h_1(z, q) + J_{\nu+1}(qz) \left(\frac{1+z}{z} \right)^{\nu-1} h_3(z, q) \right]_{z_a}^{z_b},\tag{3.3}$$

where h_1 and h_3 solve the system

$$\begin{aligned} f_1(z) &= \frac{d}{dz} h_1(z, q) + q \frac{z}{1+z} h_3(z, q) + \frac{\nu}{1+z} h_1(z, q), \\ f_2(z) &= \frac{z}{1+z} \frac{d}{dz} h_3(z, q) - q h_1(z, q) - \left[\frac{\nu-1}{(1+z)^2} + \frac{\nu+1}{1+z} \right] h_3(z, q) \end{aligned} \quad (3.4)$$

of ODEs. For convenience, we will call (3.4) the *Levin equations* in the following.

For the reasons given in section 2.3, the relations (3.3) and (3.4) are used for $\nu \geq 1$. To evaluate integrals with Bessel functions of order below 1, we instead use the relation (A.2) and subsequent integration by parts, which gives

$$\begin{aligned} & \int_{z_a}^{z_b} dz J_{\nu-1}(qz) \left(\frac{1+z}{z} \right)^{\nu-1} f_0(z) \\ &= \frac{1}{q} \int_{z_a}^{z_b} dz \frac{d}{dz} \left[z^\nu J_\nu(qz) \right] \frac{1}{z^\nu} \left(\frac{1+z}{z} \right)^{\nu-1} f_0(z) \\ &= \frac{1}{q} \left[J_\nu(qz) \left(\frac{1+z}{z} \right)^{\nu-1} f_0(z) \right]_{z_a}^{z_b} - \frac{1}{q} \int_{z_a}^{z_b} dz J_\nu(qz) \left(\frac{1+z}{z} \right)^\nu f_1(z) \end{aligned} \quad (3.5)$$

with

$$f_1(z) = \frac{z}{1+z} \frac{d}{dz} f_0(z) - \left[\frac{\nu-1}{(1+z)^2} + \frac{\nu}{1+z} \right] f_0(z). \quad (3.6)$$

Since we require $f_0(z)$ to be finite at the integration limits, the boundary terms on the r.h.s. of (3.5) vanish for $z_a = 0$ and $z_b = \infty$. The derivative in (3.6) is computed numerically in our method, as specified in equation (3.25).

3.1 Behaviour of solutions at small and large z

From equation (2.14) it is clear that one obtains the same integral with different rescaling factors by a suitable transformation of the functions f_i and h_i in the system of ODEs. For the choices made in the present and in the previous section, we have

$$\begin{aligned} f_i(z) \Big|_{r=z/(1+z)} &= (1+z)^{-\nu} f_i(z) \Big|_{r=z}, & (i = 1, 2), \\ h_1(z, q) \Big|_{r=z/(1+z)} &= (1+z)^{-\nu} h_1(z, q) \Big|_{r=z}, \\ h_3(z, q) \Big|_{r=z/(1+z)} &= (1+z)^{-\nu+1} h_3(z, q) \Big|_{r=z}. \end{aligned} \quad (3.7)$$

We thus readily obtain the small and large z behaviour of h_i with our final rescaling choice from our results in section 2.3.

For the limit $z \rightarrow 0$, we deduce from (2.28) and (2.29) that

$$\begin{aligned} f_1(z) &\sim z^{\mu+\nu} \sigma(z) \\ \Rightarrow h_3(z, q) &\sim \sigma(z) + z^{\mu+\nu+1} \sigma(z) + z^{2\nu} \sigma(z) + z^{2\nu} \ln(z) \sigma(z) \end{aligned} \quad (3.8)$$

and

$$\begin{aligned} f_2(z) &\sim z^{\mu+\nu} \sigma(z) \\ \Rightarrow h_3(z, q) &\sim \sigma(z) + z^{\mu+\nu} \sigma(z) + z^{2\nu} \sigma(z) + z^{2\nu} \ln(z) \sigma(z), \end{aligned} \quad (3.9)$$

where we recall that $\sigma(z)$ denotes a power series in z in the generic sense explained after equation (2.20). The behaviour of $h_1(z, q)$ is as the one of $h_3(z, q)$ in both (3.8) and (3.9), except that the power $z^{2\nu}$ is replaced with $z^{2\nu+2}$. It is understood that $\mu + \nu \geq 0$, which ensures that f_1 and f_2 remain finite at $z = 0$ and that the integral (3.2) with $z_a = 0$ actually exists.

We recall from our discussion in section 2.3.1 that small non-integer values of $\mu + \nu$ lead to a non-analytic behaviour of h_1 and h_3 at $z = 0$ that is difficult to approximate by functions having a Taylor expansion around that point. We therefore expect our method to become less accurate in this case. The comparison between (3.8) and (3.9) reveals that for an integrand behaving like $z^\mu J_\rho(qz)$ around $z = 0$, one should use (3.2) with $\nu = \rho$ and $f_2 = 0$ if $1 < \mu + \rho < 2$, rather than with $\nu = \rho - 1$ and $f_1 = 0$. The same holds if $0 \leq \mu + \rho < 1$. For $\mu + \rho = 1$ or $\mu + \rho \geq 2$, both options are possible.

For the large- z limit, we can discuss several cases. From (2.30) we deduce that for a power-law behaviour of f_i we have

$$\begin{aligned} f_1(z) \sim z^\mu \sigma(z^{-1}) &\Rightarrow \begin{pmatrix} h_1(z, q) \\ h_3(z, q) \end{pmatrix} \sim \begin{pmatrix} z^{\mu-1} \sigma(z^{-1}) \\ z^\mu \sigma(z^{-1}) \end{pmatrix}, \\ f_2(z) \sim z^\mu \sigma(z^{-1}) &\Rightarrow \begin{pmatrix} h_1(z, q) \\ h_3(z, q) \end{pmatrix} \sim \begin{pmatrix} z^\mu \sigma(z^{-1}) \\ z^{\mu-1} \sigma(z^{-1}) \end{pmatrix}. \end{aligned} \quad (3.10)$$

Both the functions f_i and the solutions h_i remain finite for $z \rightarrow \infty$ provided that $\mu \leq 0$. Our method thus allows the computation of Fourier-Bessel integrals not only for functions f_i with a power-law decrease but also for functions that tend to a finite value at $z \rightarrow \infty$.

For functions with an exponential falloff at large z , we get

$$f_1(z) \text{ or } f_2(z) \sim z^\mu \sigma(z^{-1}) \exp(-\kappa z) \Rightarrow \begin{pmatrix} h_1(z, q) \\ h_3(z, q) \end{pmatrix} \sim \begin{pmatrix} z^\mu \sigma(z^{-1}) \\ z^\mu \sigma(z^{-1}) \end{pmatrix} \exp(-\kappa z) \quad (3.11)$$

for $\kappa > 0$ according to section 2.3.2, whereas for functions with a Gaussian falloff, the results of appendix B imply that

$$\begin{aligned} f_1(z) \sim z^\mu \sigma(z^{-1}) \exp(-\lambda^2 z^2 - \kappa z) &\Rightarrow \begin{pmatrix} h_1(z, q) \\ h_3(z, q) \end{pmatrix} \sim \begin{pmatrix} z^{\mu-1} \sigma(z^{-1}) \\ z^{\mu-2} \sigma(z^{-1}) \end{pmatrix} \exp(-\lambda^2 z^2 - \kappa z), \\ f_2(z) \sim z^\mu \sigma(z^{-1}) \exp(-\lambda^2 z^2 - \kappa z) &\Rightarrow \begin{pmatrix} h_1(z, q) \\ h_3(z, q) \end{pmatrix} \sim \begin{pmatrix} z^{\mu-2} \sigma(z^{-1}) \\ z^{\mu-1} \sigma(z^{-1}) \end{pmatrix} \exp(-\lambda^2 z^2 - \kappa z) \end{aligned} \quad (3.12)$$

for $\lambda > 0$. Both in the exponential and in the Gaussian case, the solutions h_1 and h_3 thus have the same leading behaviour for $z \rightarrow 0$ as the functions f_1 or f_2 , except for a possible downward shift of the power z^μ by one or two units.

Using integration by parts. It remains to discuss the case where one uses integration by parts (3.5) and then evaluates the integral on its r.h.s. by Levin's method.

With (3.6) we find

$$f_0(z) \sim z^{\mu+\nu-1} \sigma(z) \Rightarrow f_1(z) \sim z^{\mu+\nu-1} \sigma(z) \quad (3.13)$$

for $z \rightarrow 0$, so that our method can be applied to integrands behaving like $z^\mu J_\rho(qz)$ with $\mu + \rho \geq 0$ for all $\rho \geq 0$.

At large z we have

$$f_0(z) \sim z^\mu \sigma(z^{-1}) \exp(-\lambda^2 z^2 - \kappa z) \quad \Rightarrow \quad f_1(z) \sim z^\rho \sigma(z^{-1}) \exp(-\lambda^2 z^2 - \kappa z) \quad (3.14)$$

with

$$\rho = \begin{cases} \mu - 1 & \text{if } \lambda = \kappa = 0, \\ \mu & \text{if } \lambda = 0 \text{ and } \kappa > 0, \\ \mu + 1 & \text{if } \lambda > 0. \end{cases} \quad (3.15)$$

One thus gets the same leading exponential or Gaussian behaviour for f_0 and f_1 . A pure power law $f_0 \sim z^\mu$ with $\mu \leq 0$ implies a power-law decrease $f_1 \sim z^{\mu-1}$.

Grand summary. As an upshot of our detailed discussion, we retain that if a set of basis functions is good for approximating the functions f_1 or f_2 in (3.2), or f_0 in (3.5), it can be expected to be good for approximating the solutions h_1 and h_3 of the Levin equations (3.4) and hence allow for an accurate computation of the integrals. A small- z behaviour like $z^{1-\delta}$ with $\delta < 1$ is tolerable for f_0 or f_1 , because the corresponding power of z for h_1 and h_3 is larger by one unit.

3.2 Discretisation on Chebyshev grids

We now discuss in detail how we implement the method of collocation for solving the Levin equations (3.4).

In most examples of Levin's original work [12, 13], the chosen basis functions are polynomials $b_i(z) = (z - z_0)^i$, and the system of ODEs is evaluated at *equispaced* points between z_a and z_b . It was found that the accuracy of the method could be improved by dividing the integration domain into several subintervals. Other options for the basis functions are mentioned in [12]. It is well known that polynomial approximation on equispaced grids suffers from Runge's phenomenon: the approximation becomes poor in the vicinity of the interval end points when one increases the number of grid points (i.e. the polynomial order). This problem is avoided by using suitable grids that are not equispaced. A prominent example is *Chebyshev interpolation*, which is described in detail in [17]. This was indeed used in the context of Levin's method in [14, 15].

Motivated by our experience with interpolating (single and double) parton distributions on Chebyshev grids [18, 19], we adopt Chebyshev interpolation to our present case. Our method involves three steps.

Variable transform. We first define a transformation from z to the variable u that will be used for interpolation with Chebyshev polynomials. The values $u_a = u(z_a)$ and $u_b = u(z_b)$ must both be finite. We require $u(z)$ to be an analytic function with $du/dz > 0$ for all $z \in [z_a, z_b]$, except for the point $z_b = \infty$, where necessarily $du/dz = 0$.

A primary purpose of this transformation is to map an infinite integration interval $[z_a, \infty]$ onto a finite interval in u . On a finite interval in z , one may take the trivial transformation $u = z$. However, even in this case a non-trivial variable transformation can be beneficial, for instance when $f_i(z)$ rises or decreases very steeply.

Depending on the behaviour of $f_i(z)$, different variable transformations $u(z)$ lead to good results of our method. A selection of such transformations is presented in section 3.2.2.

Subintervals. We find that it is often useful to split $[z_a, z_b]$ into k subintervals $[z_0, z_1]$, $[z_1, z_2]$, \dots , $[z_{k-1}, z_k]$ with $z_0 = z_a$ and $z_k = z_b$ and to evaluate the integral on each of them separately. We will see that this benefits both the integration accuracy and the computation time. Following the notation introduced in [18, 19], we write

$$[z_0, z_1, \dots, z_k]_{(n_1, \dots, n_k)} \quad (3.16)$$

to characterise a grid and its subgrids, where z_j are the interval boundaries, and n_j is the number of points on each subgrid. The total number of grid points is then $\sum_{j=1}^k n_j - (k - 1)$, because adjacent subgrids share their end points. In the notation (3.16) it is understood that one and the same variable transform is used on the full interval from z_0 to z_k .

For simplicity, we will continue to present our method for a single integration interval $[z_a, z_b]$, bearing in mind that this may be a subinterval in the sense just described.

Chebyshev interpolation. On each subinterval, we approximate the functions $h_1(z, q)$ and $h_3(z, q)$ using Chebyshev interpolation. A compendium of this method with the formulae needed for our method is given in appendix C. In brief, we approximate

$$h_i(z, q) \approx p_i(u(z), q), \quad (3.17)$$

where $p_i(u, q)$ is the unique polynomial of order N that reproduces the function

$$h_i(z_j, q) = p_i(u_j, q), \quad u_j = u(z_j) \quad (3.18)$$

at the $n = N + 1$ points z_j that correspond to the Chebyshev points u_j on the interval $[u_a, u_b]$, with u_j given in (C.11). Note that these points include the interval boundaries, $z_a = z_0$ and $z_b = z_N$, where the functions h_i are required for evaluating the Fourier-Bessel integral with the master formula (3.3) of our method.

The derivatives of dh_i/dz appearing in the Levin equations (3.4) can be approximated by the derivatives of the interpolants dp_i/dz . When evaluating the equations at the points z_j , these derivatives can be evaluated via a matrix multiplication. In summary, we discretise (3.4) by making the following replacements:

$$\begin{aligned} f_i(z) &\rightarrow f_i(z_j) && (i = 1, 2), \\ h_i(z, q) &\rightarrow p_i(u_j, q) && (i = 1, 3), \\ \frac{d}{dz} h_i(z, q) &\rightarrow \frac{du}{dz}(z_j) \sum_k D_{jk}^u p_i(u_k, q) && (i = 1, 3), \end{aligned} \quad (3.19)$$

where D_{jk}^u is given in (C.12) and du/dz is the Jacobian of the variable transform. The Levin equations are thus replaced by a system of linear equations, which can be written as

$$B(q) \cdot \mathbf{P}(q) = \mathbf{F} \quad (3.20)$$

with the $2n$ -dimensional vectors

$$\begin{aligned} \mathbf{F} &= (f_1(z_0), f_1(z_1), \dots, f_1(z_N), f_2(z_0), f_2(z_1), \dots, f_2(z_N))^T, \\ \mathbf{P}(q) &= (p_1(z_0, q), p_1(z_1, q), \dots, p_1(z_N, q), p_3(z_0, q), p_3(z_1, q), \dots, p_3(z_N, q))^T \end{aligned} \quad (3.21)$$

and the $2n$ -dimensional square matrix

$$B(q) = \begin{pmatrix} B^{aa} & B^{ab}(q) \\ B^{ba}(q) & B^{bb} \end{pmatrix} \quad (3.22)$$

with diagonal blocks

$$\begin{aligned} B_{jk}^{aa} &= \frac{du}{dz}(z_j) D_{jk}^u + \frac{\nu}{1+z_j} \delta_{jk}, \\ B_{jk}^{bb} &= \frac{z_j}{1+z_j} \frac{du}{dz}(z_j) D_{jk}^u - \left[\frac{\nu-1}{(1+z_j)^2} + \frac{\nu+1}{1+z_j} \right] \delta_{jk} \end{aligned} \quad (3.23)$$

and off-diagonal blocks

$$B_{jk}^{ab}(q) = q \frac{z_j}{1+z_j} \delta_{jk}, \quad B_{jk}^{ba}(q) = -q \delta_{jk}, \quad (3.24)$$

where j and k run from 0 to N in all cases.

Note that up to this point, the only approximation we have made was to replace the derivatives of h_i at the points z_j by the derivatives of their approximants p_i . If we use the integration-by-parts identity (3.5), then we also invoke Chebyshev interpolation to approximately compute the derivative df_0/dz in the definition (3.6) of f_1 . The values of f_1 at the grid points are thus obtained from the corresponding values of f_0 as

$$\begin{aligned} f_1(z_j) &\approx \sum_k C_{jk} f_0(z_k), \\ C_{jk} &= \frac{z_j}{1+z_j} \frac{du}{dz}(z_j) D_{jk}^u - \left[\frac{\nu-1}{(1+z_i)^2} + \frac{\nu}{1+z_i} \right] \delta_{jk}. \end{aligned} \quad (3.25)$$

In section 3.1 we investigated in detail how the small- z behaviour of h_1 and h_3 is related to the small- z behaviour of f_1 or f_2 . Since we require the variable transformation between u and z to be analytic and to have a finite derivative at $z=0$, the interpolation polynomials $p_i(u(z), q)$ in u have a Taylor expansion around $z=0$. To obtain a good approximation when discretising the Levin equations, we hence need that h_1 and h_3 can be sufficiently well approximated by a Taylor series around $z=0$, with the first n Taylor coefficients being free and the remaining ones fixed by the variable transform.

A corresponding statement holds for the small- z behaviour of $f_0(z)$ when using integration by parts. Notice that if one has $f_0 \sim z^{1-\delta}$ with $0 < \delta < 1$, one gets a divergent first derivative of f_0 at $z=0$, which is however multiplied with z in (3.6) and thus can be accommodated within our setup.

Using quadrature. We will see that the matrix B in (3.20) becomes ill-conditioned when q becomes small. As described in the next subsection, this can in part be dealt with by linear algebra methods. On the other hand, there is no compelling need to use the Levin method when the integrand in (3.2) is not rapidly oscillating in the integration interval $[z_a, z_b]$. In our algorithm, we therefore replace the Levin method with Clenshaw-Curtis quadrature if for a given q one has

$$qz_b \leq j_\nu, \quad (3.26)$$

where j_ν is the first zero of the Bessel function $J_\nu(x)$. We find that this yields a high integration accuracy and also saves computing time. The quadrature result is obtained as the sum

$$I(q) \approx \sum_j w_j^z \left(\frac{1+z_j}{z_j} \right)^\nu \left[J_\nu(qz_j) f_1(z_j) + J_{\nu+1}(qz_j) f_2(z_j) \right], \quad (3.27)$$

where $I(q)$ is defined in (3.2) and the weights are given by

$$w_j^z = \left(\frac{du}{dz}(z_j) \right)^{-1} w_j^u \quad (3.28)$$

with w_j^u from (C.13).

3.2.1 Solving the linear equation system

The system (3.20) has a unique solution if the matrix B is nonsingular. By taking increasingly fine interpolation grids, i.e. increasingly high order of the interpolation polynomials $p_i(u, q)$, one should eventually approach the limit of the original Levin equations, which has an infinity of solutions. One can hence expect that for sufficiently fine interpolation grids, the matrix B is close to singular. This poses a challenge to the numerical solution of (3.20).

The work in [14, 15] contains a detailed analysis of the linear equation system for a different set of integrals, along with a strategy for its solution. We follow a rather similar strategy in the present work, selecting one out of two algorithms to solve (3.20).

Our default algorithm uses the LU decomposition (see e.g. [20, Chapter 2.3]), which represents B in the form

$$B = \Pi \cdot L \cdot U, \quad (3.29)$$

where Π is a permutation matrix, L is a lower diagonal matrix with all diagonal elements equal to 1, and U an upper diagonal matrix. The product of the diagonal elements U_{ii} is equal to $\det(B)$, so that at least one of these elements is zero when B is singular. If this is not the case, the solution of $B \cdot \mathbf{P} = \mathbf{F}$ is obtained by successively solving

$$L \cdot \mathbf{G} = \Pi^{-1} \cdot \mathbf{F}, \quad U \cdot \mathbf{P} = \mathbf{G}, \quad (3.30)$$

which can be done by forward and backward substitution, respectively. The second step involves the inverse diagonal elements $1/U_{ii}$ of U and becomes numerically unstable when B is close to singular. As criterion for this case, we use

$$\min_i(|U_{ii}|) \leq r_{LU}^{\max} \max_i(|U_{ii}|), \quad (3.31)$$

where r_{LU}^{\max} can be chosen by the user.

If (3.31) is satisfied for a given matrix B , we use the singular value (SV) decomposition. In this case, B is represented as

$$B = U \cdot S \cdot V^T, \quad (3.32)$$

where U and V are orthogonal⁴ and $S = \text{diag}(S_{ii})$ is diagonal and positive semidefinite.

For nonsingular B , the solution of $B \cdot \mathbf{P} = \mathbf{F}$ is then readily given by

$$\mathbf{P} = V \cdot \text{diag}(1/S_{ii}) \cdot U^T \cdot \mathbf{F}. \quad (3.33)$$

If B is singular, then some of the S_{ii} vanish, and one replaces the corresponding entries $1/S_{ii}$ in (3.33) with zero. As shown e.g. in [20, Chapter 2.6], this yields an approximate solution of (3.20) in the sense that \mathbf{P} obtained in this way minimises $|B \cdot \mathbf{P} - \mathbf{F}|$, i.e. the distance between the vectors on the two sides of the equation. The numerical stability of this procedure is greatly enhanced by also replacing $1/S_{ii}$ with zero when S_{ii} is very small; this is called a *truncated* SV decomposition. We choose to replace an entry $1/S_{ii}$ with zero if it satisfies

$$S_{ii} < r_{SV}^{\max} \max_j(S_{jj}), \quad (3.34)$$

with r_{SV}^{\max} to be chosen by the user.

A numerical computation is typically much faster for the LU decomposition (3.29) than for the SV decomposition (3.32). One should hence take r_{LU}^{\max} as small as can be done without

⁴Note that U denotes different matrices in (3.32) and (3.29).

shorthand	$-u(z)$	$z(u)$	du/dz
inv pow	$(z + z_0)^{-\alpha}$	$ u ^{-1/\alpha} - z_0$	$\alpha (z + z_0)^{-1-\alpha}$
log pow	$\left[\ln \frac{z+z_{\text{hi}}}{z+z_{\text{lo}}}\right]^\alpha$	$\frac{z_{\text{hi}}-z_{\text{lo}} \exp(u ^{1/\alpha})}{\exp(u ^{1/\alpha})-1}$	$\frac{\alpha (z_{\text{hi}}-z_{\text{lo}})}{(z+z_{\text{hi}})(z+z_{\text{lo}})} u ^{(\alpha-1)/\alpha}$
exp	$\exp\left[-\frac{1}{4}mz\right]$	$\frac{4}{m}L(u)$	$\frac{1}{4}m u $
exp sqrt	$\exp\left[1 - \sqrt{1 + mz/2}\right]$	$\frac{2}{m}\left[L^2(u) + 2L(u)\right]$	$\frac{1}{4}m u \left[L(u) + 1\right]^{-1}$
Gauss	$\exp\left[-\frac{1}{4}(m^2z^2 + mz)\right]$	$\frac{1}{2m}\left[\sqrt{16L(u) + 1} - 1\right]$	$\frac{1}{4}m u \sqrt{16L(u) + 1}$

Table 1: Variable transformations suitable for integration over z from 0 to ∞ . It is understood that $\alpha > 0$, $z_0 > 0$, $z_{\text{hi}} > z_{\text{lo}} > 0$, and $m > 0$. All transformations satisfy $u \leq 0$ and $du/dz > 0$ for $u < 0$. At $u = 0$ one has $z = \infty$ and $du/dz = 0$. We abbreviate $L(u) = \ln(1/|u|)$.

compromising the accuracy of the result. Our choice of the control parameters r_{LU}^{\max} and r_{SV}^{\max} is discussed in section 4.1.

The computation time for both the LU and the SV decomposition grows very quickly with the dimension of the matrix B . From this point of view, it is beneficial to split the overall integration region $[z_a, z_b]$ into subintervals, since this allows one to work with smaller matrices B_k on each subinterval k .

3.2.2 Examples of variable transforms

A selection of variable transformations that are suitable for integration over z from 0 to ∞ is presented in table 1. The table has been adapted from table 1 in [19], where the same transformations were used to describe the dependence of double parton distributions on the transverse distance between the two partons.

The following brief characterisation of the different transforms is the result of detailed numerical investigations, part of which will be presented in the next sections.

- The inverse power law transformation in the first row of the table is suitable for integrals with a large- z behaviour like $f(z) \sim z^\mu$ with $\mu \leq 0$.
- The transformation in the second row behaves like $u \approx -\ln^\alpha(z_{\text{hi}}/z)$ for $z_{\text{lo}} \ll z \ll z_{\text{hi}}$ and like an inverse power law $u \approx -\text{const } z^{-\alpha}$ for $z \gg z_{\text{hi}}$. This is useful for functions that involve high powers of $\ln z$, as we will see in section 6.
- The exponential transform in the third row works well for functions that have a Gaussian behaviour $f(z) \sim \exp(-\lambda^2 z^2)$ at large z , possibly modified by an exponential $\exp(-\kappa z)$ times a power of z .
- The exponential transform with a square root in the fourth row works well for $f(z) \sim \exp(-\kappa z)$ at large z , possibly modified by a power of z .

In our study [19] of double parton distributions, we have shown that the Gaussian transformation in the last row yields good *interpolation* accuracy for functions with a Gaussian behaviour at large z . Likewise, we found that the exponential transform in the third row allows for an accurate interpolation of functions with an exponential falloff. As we will see in section 5, the same combinations of variable transforms and integrands work with Levin's method but are less powerful than the combinations specified above.

3.3 Summary of the algorithm

Our complete algorithm naturally proceeds in several steps.

1. The user must specify an interpolation grid, i.e. a variable transform $u(z)$, a subinterval division in z , and the number of grid points per subinterval. Then
 - (a) compute the grid points z_j ,
 - (b) evaluate the values at the grid points for the function(s) to be integrated over, i.e. for $f_1(z)$, $f_2(z)$ or $f_0(z)$ in (3.2) or (3.5),
 - (c) perform steps 2 to 4 for each subinterval and add up the integrals from these subintervals.

2. For a given value of ν
 - (a) compute the values of $[z_j/(1+z_j)]^\rho$ with $\rho = 1, \nu$, and $\nu - 1$ for each grid point,
 - (b) compute the diagonal blocks (3.23) of the matrix B , as well as the matrix C in (3.25),
 - (c) compute the Clenshaw-Curtis weights w_j^z in (3.28).

We recall that for a given ν , the method allows the computation of integrals with $J_{\nu-1}(qz)$, $J_\nu(qz)$, and $J_{\nu+1}(qz)$.

3. For a given value of q
 - (a) determine from (3.26) whether to use quadrature or the Levin method,
 - (b) compute the values of $[(1+z)/z]^\nu J_\nu(qz)$ and $[(1+z)/z]^\nu J_{\nu+1}(qz)$, for all grid points z_j if quadrature is used, and for the interval boundaries otherwise,
 - (c) if the Levin method is used: compute the off-diagonal blocks (3.24) of the matrix B ,
 - (d) if the Levin method is used: set up the linear equation solver by computing the LU and — if needed — the SV decomposition of B .

4. For given values $f_i(z_j)$ on the interpolation grid ($i = 0, 1$, or 2)
 - (a) for integrals with $J_{\nu-1}(qz)$: evaluate the boundary terms at z_a and z_b in (3.5) and compute $f_1(z_j)$ from $f_0(z_j)$ using (3.25),
 - (b) if the Levin method is used: solve the matrix equation (3.20),
 - (c) evaluate the integral from the master formula (3.3) or (3.5).

The time required for step 1b crucially depends on the functions to be integrated; an important feature of our method is that the functions need not be evaluated separately for different values of q . The evaluation of Bessel functions is limited to step 3b and required only once for a given q .

The operations in step 2 need to be done only once for a given choice of ν and the interpolation grid – they should be irrelevant for the overall computing time in a typical workflow. We find step 3d to be by far the most time consuming one. By comparison, all operations in step 4 are fast.

Recalling the use cases mentioned in the introduction, we see that our method (as well as the Levin method in its original form) is particularly efficient for a workflow in which one needs the Fourier-Bessel transform of *many* similar functions at a given value of q . With functions of sufficiently similar shape, one can take a common grid for discretisation. The computationally expensive step 3d has to be carried out once for a given q , after which the much faster steps in 4 can be repeated for each discretised function in turn.

3.4 Implementation in BestLime

We have implemented this algorithm in the C++ library BESTLIME, which is available on [16]. It offers a number of variable transforms $u(z)$, including those in table 1, as well as the possibility to work with user-defined transformations. Routines are provided to compute the integral in (3.2) for given f_1 or f_2 , or the integral in (3.5) for given f_0 , taking as arguments the value of q and the values of the relevant function f_i on the points of the interpolation grid. There are also calls for computing $\int dz J_\rho(qz) \tilde{f}(z)$ with $\rho = \nu, \nu + 1$, or $\nu - 1$. These calls simply multiply $\tilde{f}(z)$ with $[z/(1+z)]^\nu$ or $[z/(1+z)]^{\nu-1}$ and then evaluate the integral in (3.2) or (3.5).

Step 1a and the steps in 2 are carried out once when initialising an integration setup, which is characterised by a discretisation grid and a value $\nu \geq 1$. An integration call invokes the steps in 3 if and only if the requested q differs from its value in the previous call. The results of these steps are stored and reused in subsequent calls at the same q . This enables the workflow described at the end of the previous subsection.

For linear algebra operations, BESTLIME uses the Eigen library [21], specifically the part for dense matrices in Eigen version 3.4.0. In particular, the linear equations are solved using the methods `PartialPivLU` (LU decomposition with partial pivoting) or `BDCSVD` (Bidiagonal Divide and Conquer SVD).

For the computation of Bessel functions (and of the hypergeometric function ${}_2F_1$ in the benchmark comparison of section 4.2), the GNU Scientific Library (GSL) [22] is used.

The methods of BESTLIME that deal with Chebyshev interpolation have been taken from the CHILIPDF library [18, 19], which is under development.

4 Numerical studies

In this section, we investigate several numerical and computational aspects of our integration algorithm. To characterise the interpolation grids, we use the shorthand names for variable transforms in the first column of table 1, along with the notation for grid boundaries and grid points in equation (3.16).

All results in this and the next sections have been obtained with the library BESTLIME. We begin with a brief discussion of the parameters that control the algorithm used for solving the discretised Levin equations (3.20). After this, we present benchmarks for the integration accuracy. Finally, we give an indication of the computation time required by BESTLIME for representative integration setups.

4.1 Control parameters for solving the linear equation system

As explained in section 3.2.1, we use the LU decomposition (3.29) to solve the discretised Levin equations, provided that the matrix B is sufficiently far from being singular. A measure for this is the ratio

$$r_{LU} = \frac{\min_i (|U_{ii}|)}{\max_i (|U_{ii}|)}, \quad (4.1)$$

where U_{ii} denotes the diagonal elements of the matrix U in (3.29). Let us see when this ratio becomes very small.

In the following exercise, we consider grids of the form $[0, z_1, \infty]_{(n_1, n_2)}$ with (n_1, n_2) equal to (16, 32) or (32, 64). We use either the `exp sqrt` transform specified in table 1 with the parameter m ranging from 0.32 to 3.85, or the `exp` transform with m ranging from 0.19 to 2.24. (These settings correspond to the parameter scans presented in section 5.2.3.) Apart

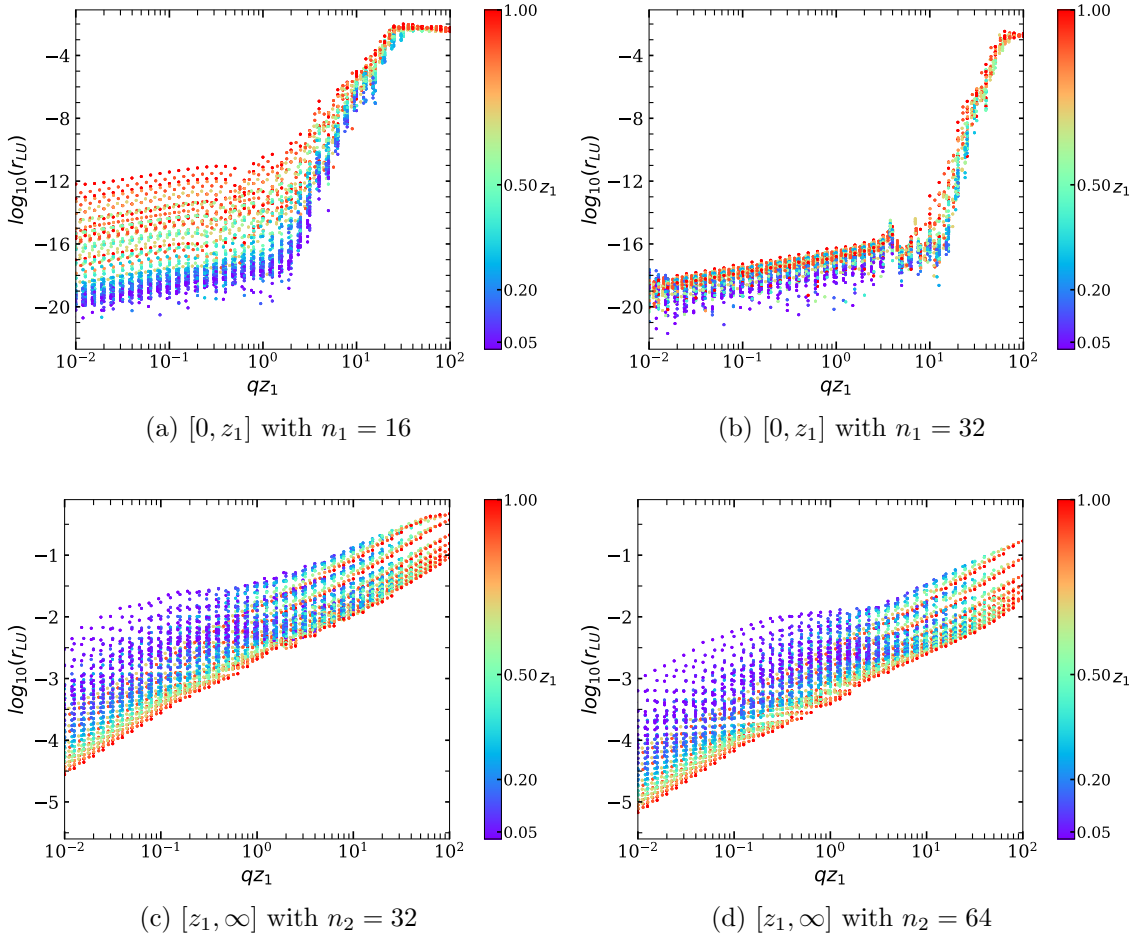


Figure 2: The ratio r_{LU} defined in (4.1) for the matrix B on a given subgrid. The plots in this figure are for $\nu = 1$. See the text for details of the variable transform $u(z)$.

from some details, our results are very similar for different values of ν , and in figures 2 and 3 we show them for $\nu = 1$ and $\nu = 2$, respectively.

We compute B for a wide range of z_1 and q values, with linearly spaced z_1 values between 0.03 and 1 and logarithmically spaced q values between 0.01 and 100. We find r_{LU} to be rather strongly correlated with the product qz_1 of these variables, as shown for the lower subinterval $[0, z_1]$ in the top panels of figures 2 and 3 and for the upper subinterval $[z_1, \infty]$ in the bottom panels of these figures.

On the upper subinterval, r_{LU} is always relatively large, decreasing only slightly when the number of grid points is increased. One can expect the LU decomposition to give reliable numerical results in this range, and our integration benchmarks confirm that this is indeed the case.

The situation is very different in the lower subinterval. Here r_{LU} drops sharply as qz_1 decreases to values of order 1, and it remains very small when qz_1 decreases even further. This confirms our expectation given in section 3.2.1: in a z interval where the Bessel functions $J_\nu(qz)$ and $J_{\nu+1}(qz)$ have only few or no oscillations, the discretised version of the Levin equations approaches the “continuum limit”, in which these equations have an infinite number of solutions.

We checked separately that with a single subinterval $[0, \infty]$ the value of r_{LU} stays above 10^{-6} for $n \leq 96$ points with the variable transformations and q values specified above. For a single interval from 0 to ∞ , one can hence expect the LU method to work well throughout.

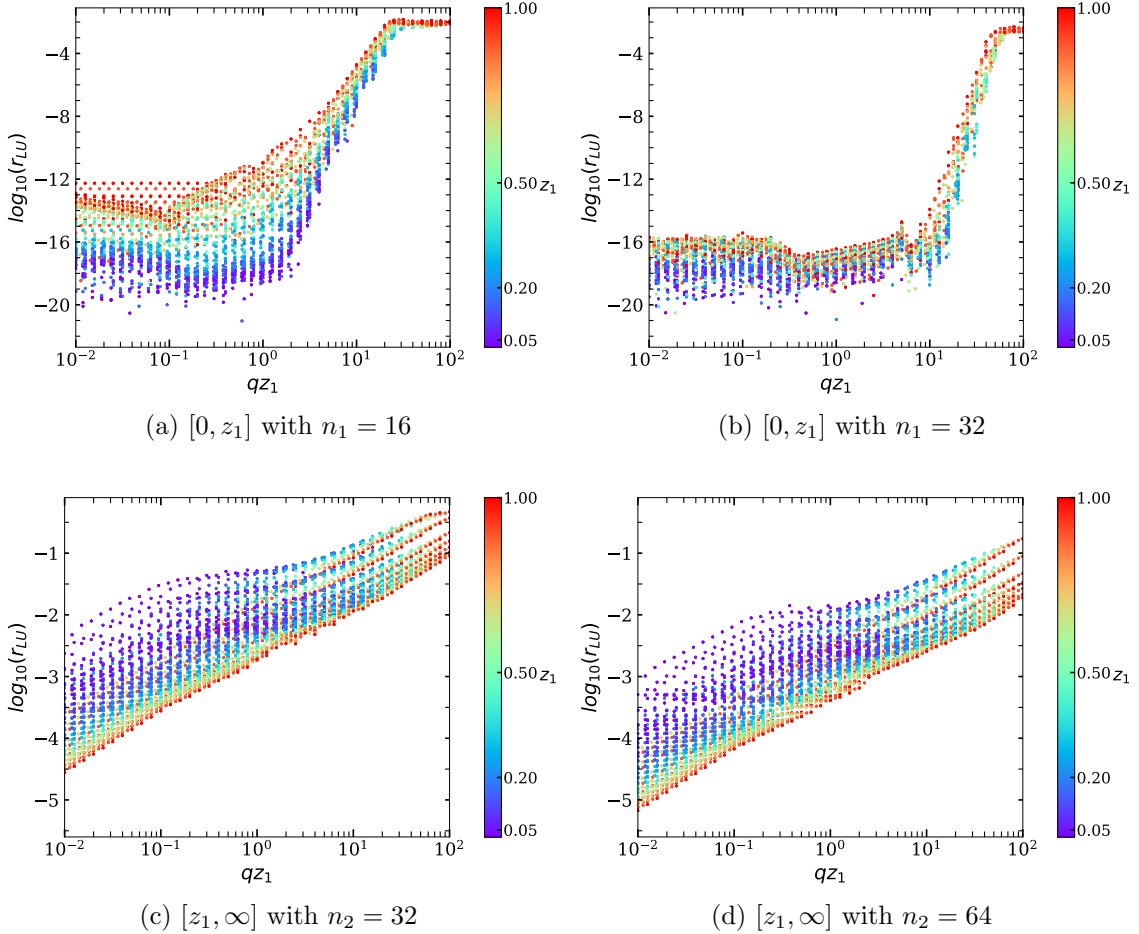


Figure 3: As figure 2, but for $\nu = 2$.

When $r_{LU} \leq r_{LU}^{\max}$, we no longer use the LU decomposition to solve the linear equations and resort to the computationally more stable (and more expensive) SV decomposition. When the latter is used, we also need to choose the threshold r_{SV}^{\max} for truncating small singular values as specified in (3.34).

To set these two control parameters of our method, we disabled the use of quadrature in intervals with $qz_1 \leq j_\nu$ (see the discussion around (3.26)) and monitored how the integration accuracy depends on r_{LU}^{\max} and r_{SV}^{\max} . We performed this monitoring for the integrals in sections 4.2 and 5 and found

$$r_{LU}^{\max} = r_{SV}^{\max} = 10^{-12} \quad (4.2)$$

to be a satisfactory setting. Our choice for r_{LU}^{\max} is conservative in the sense that decreasing it by two orders of magnitude does not degrade the accuracy in the test cases just mentioned. When the use of quadrature in intervals with $qz_1 \leq j_\nu$ is enabled, the integration accuracy is even less dependent on the precise settings of r_{LU}^{\max} and r_{SV}^{\max} . This is because small values of r_{LU} or r_{SV} tend to appear only for small values of qz , when quadrature can be used.

We find that the only settings where the SV decomposition is needed involve very fine subgrids and intermediate values of q (small enough to give a small r_{LU} but large enough to fail our criterion for using quadrature). An example is given in the rightmost column of table 4.

case	$\tilde{f}(z)$	$I(q)$
1a	$z^{\nu+1} K_0(\kappa z)$	$\Gamma(\nu+1) (2q)^\nu / (\kappa^2 + q^2)^{\nu+1}$
1b	$z^{\mu+\nu+1} K_\mu(\kappa z)$	$\Gamma(\mu+\nu+1) (2\kappa)^\mu (2q)^\nu / (\kappa^2 + q^2)^{\mu+\nu+1}$
2	$z^\mu e^{-\kappa z}$	$\frac{\Gamma(\mu+\nu+1)}{\Gamma(\nu+1)} \left(\frac{q}{2}\right)^\nu \kappa^{-\mu-\nu-1} {}_2F_1\left(\frac{\mu+\nu+1}{2}, \frac{\mu+\nu+2}{2}; \nu+1; -\frac{q^2}{\kappa^2}\right)$
3	$e^{-\lambda^2 z^2}$	$\frac{\sqrt{\pi}}{2\lambda} \exp\left(-\frac{q^2}{8\lambda^2}\right) I_{\nu/2}\left(\frac{q^2}{8\lambda^2}\right)$
4	$z^{\nu+1} e^{-\lambda^2 z^2}$	$\frac{1}{q} \left(\frac{q}{2\lambda^2}\right)^{\nu+1} \exp\left(-\frac{q^2}{4\lambda^2}\right)$
5a	$\left(\frac{z}{z^2+b^2}\right)^{\nu+1}$	$\frac{1}{\Gamma(\nu+1)} \left(\frac{q}{2}\right)^\nu K_0(qb)$
5b	$z^{\nu+1} / (z^2 + b^2)^{\mu+\nu+1}$	$\frac{1}{\Gamma(\mu+\nu+1)} \left(\frac{q}{2}\right)^\nu \left(\frac{q}{2b}\right)^\mu K_\mu(qb)$
6a	1	$\frac{1}{q}$
6b	$z^{-\nu}$	$\frac{\Gamma(1/2)}{2\Gamma(\nu+1/2)} \left(\frac{q}{2}\right)^{\nu-1}$
7a	$z^{-\nu+1}$	$\frac{1}{2\Gamma(\nu)} \left(\frac{q}{2}\right)^{\nu-2}$
7b	$z^{-\nu+1}$	$\frac{1}{2\Gamma(\nu)} \left(\frac{q}{2}\right)^{\nu-2} - \frac{1}{q} z_b^{-\nu+1} J_{\nu-1}(qz_b)$
8	$z^{\nu+1}$	$\frac{1}{q} z_b^{\nu+1} J_{\nu+1}(qz_b)$

Table 2: The functions $\tilde{f}(z)$ used for our benchmark exercise and their Fourier-Bessel transforms $I(q)$ specified in (4.3). Cases 1a, 5a, 6a, and 7a are special cases of 1b, 5b, 6b, and 7b, respectively, but are handled with different integration settings (see equation (4.7) and table 3). Here I_ν and K_ν are the modified Bessel functions of the first and second kind, and ${}_2F_1$ is the Gaussian hypergeometric function.

4.2 Benchmarks: grids and precision

To assess the performance of our algorithm, we compute a number of Fourier-Bessel integrals whose exact form is known analytically. The integrals considered are

$$I(q) = \int_0^{z_b} dz J_\nu(qz) \tilde{f}(z) \quad \text{with } z_b = \begin{cases} \infty & \text{for cases 1a to 7a,} \\ 10 & \text{for cases 7b and 8,} \end{cases} \quad (4.3)$$

where $\tilde{f}(z)$ and $I(q)$ for the different cases are given in table 2. Unless specified otherwise in table 3, the integrals are evaluated for

$$\nu = \begin{cases} 0, 0.5, 1, 1.5, 2 & \text{with } J_{\nu-1} \text{ calls,} \\ 1, 1.5, 2, 2.5, 3 & \text{with } J_\nu \text{ calls,} \\ 2, 2.5, 3 & \text{with } J_{\nu+1} \text{ calls,} \end{cases} \quad (4.4)$$

$$q = 0.01, 0.1, 1, 2, 3, 5, 10, 15, 20, 25, 30 \quad (4.5)$$

The different ‘‘calls’’ specified in (4.4) refer to the master equations (3.2) and (3.5) of our method, i.e. the $J_{\nu-1}$, J_ν , and $J_{\nu+1}$ calls respectively correspond to a nonzero f_0 , f_1 , and f_2 in these equations.

We find grid settings both for intermediate or for high precision. Specifically, we obtain a

case	parameters	variable transform	remarks
1a	$\kappa = 1.5$	exp sqrt , $m = 1.5\kappa$	$\nu \leq 2.5$
1b	$\kappa = 1.5, \mu = 1$	exp sqrt , $m = \kappa$	$\nu \leq 2.5$
2	$\kappa = 1.5, \mu = 2.5$	exp sqrt , $m = 1.5\kappa$	
3	$\lambda = 2$	exp , $m = 4\lambda$	not $\nu = 0.5$
4	$\lambda = 2$	————— ” —————	$q \leq 10$
5a	$b = 1.2$	inv pow , $z_0 = 1, \alpha = 0.5$	$q \leq 10$
5b	$b = 1.2, \mu = 2.5$	inv pow , $z_0 = 1, \alpha = 1$	$q \leq 10$
6a		inv pow , $z_0 = 1, \alpha = 0.5$	not $\nu = 0.5$
6b		————— ” —————	only $\nu \geq 0.5$, not using $J_{\nu+1}$ call
7a		————— ” —————	only $\nu \geq 1$
7b		————— ” —————	also for $q = 0.001, 50, 100, 200, 300$
8		trivial transform $z = u$	also for $q = 0.001, 50, 100, 200, 300$

Table 3: Details for computing the integrals in table 2. The variable transforms are specified in table 1 and discussed in section 3.2.2.

relative integration error ε of

$$\varepsilon \leq 5 \times 10^{-4} \quad \text{with} \quad \begin{cases} [0, 1, \infty]_{(20,25)} & \text{for cases 1a to 7a,} \\ [0, \infty]_{(45)} & \text{for cases 1b to 7a,} \\ [0, 10]_{(24)} & \text{for cases 7b and 8,} \end{cases} \quad (4.6)$$

and

$$\varepsilon \leq 10^{-6} \quad \text{with} \quad \begin{cases} [0, 0.1, \infty]_{(30,44)} & \text{for case 1a,} \\ [0, 1, \infty]_{(30,44)} & \text{for cases 1b to 7a,} \\ [0, 10]_{(34)} & \text{for cases 7b and 8.} \end{cases} \quad (4.7)$$

These grid settings and the parameters of variable transforms in table 3 are not optimised for each individual integrand, but have been chosen with as little variation as needed to achieve the accuracy goals of 5×10^{-4} or 10^{-6} . In practical applications, one will often deal with less variation in the shape of integrands and in the value of ν . One can then perform a more systematic optimisation of grid settings, as we will do for TMD-like functions in section 5.

We note that in cases 5a and 5b the integral $I(q)$ decreases exponentially with q , whilst in case 4 it decreases like a Gaussian in q . We limit the benchmark to $q \leq 10$ in these cases. For larger value the accuracy degrades rather quickly with our grid settings, which is not too surprising because the integrals become extremely small as a result of numerical cancellations. For $\nu = 0$, the integrand of case 1a behaves like $-z \ln(z)$ at $z \rightarrow 0$ and hence has a divergent first derivative in that limit. This puts higher requirements on the discretisation. In particular, the grid $[0, \infty]_{(45)}$ yields an accuracy of only $\varepsilon \approx 3 \times 10^{-3}$, which is quite inferior to what we obtain with the same grid for cases 1b to 7a. In such a situation, splitting the integration

grid	$[0, \infty]_{(45)}$	$[0, 1, \infty]_{(20,25)}$		$[0, 1, \infty]_{(40,50)}$		
method	LU	(CC, LU)	(LU, LU)	(CC, LU)	(LU, LU)	(SV, LU)
q range	low	low	intermediate	low	high	intermediate
new q [μ s]	45	12	18	60	100	1500
same q [μ s]	1.9	0.8	1.3	2.5	3.6	4.1

Table 4: Indicative computation times of the integration call for $J_{\nu-1}$ (which includes integration by parts). The second row specifies the integration method used in each subinterval. The q ranges are $0.095 \dots 0.1$ (low), $14.25 \dots 15$ (intermediate), and $38 \dots 40$ (high). Timings have been obtained on a recent laptop with an Intel[®] Core[™] i7-1355U processor, 32 GiB memory, and code compiled with g++ version 11.4.0.

interval into subgrids gives more flexibility and allows one to achieve significantly better accuracy for a given number of points. We will confirm this trend in section 5.2.2.

Notice also that we omit the value $\nu = 0.5$ in our benchmark for cases 3 and 6a. In these cases, one has an integrand behaving like $z^\mu J_\nu(qz)$ with $\mu + \nu = 0.5$ at small z , for which we expect our method to be less accurate as discussed in section 3.1. This is borne out by our numerical study: the relative integration error for $\nu = 0.5$ in cases 3 and 6a is $\varepsilon \leq 2 \times 10^{-3}$ for the grids $[0, 1, \infty]_{(20,25)}$ and $[0, \infty]_{(45)}$, and $\varepsilon \leq 3 \times 10^{-4}$ for the grid $[0, 1, \infty]_{(30,44)}$. Although this is worse than the benchmark accuracy in (4.6) and (4.7), it shows that our method can handle these cases as well.

4.3 Computation time

Indicative computation times needed for integration calls under different conditions are given in table 4. The first two grids are those in our benchmark exercise of the previous subsection; and the grid with $(n_1, n_2) = (40, 50)$ may be used for estimating the integration error of the grid with $(n_1, n_2) = (20, 25)$, as will be discussed in section 5.3. The times in the table do *not* include the time required for computing the integrand on the grid points (step 1b in section 3.3), since that time crucially depends on the function for the integrand and not on our algorithm.

As discussed in section 4.1, the integration method used in the first of two subintervals depends on q . At sufficiently low q , quadrature can be used, whilst for large q the matrix B becomes well conditioned and the LU decomposition can be employed. For intermediate q values, the LU method can be used for less fine grids, but it will become unstable for finer grids, when the SV decomposition must be taken instead.

The *absolute* times in the table should not be over-interpreted, since they refer to a particular computer (where they fluctuate at the level of 20% between different runs). Running the same code on a range of other laptops and desktop PCs, we find that some times are larger than those in the table by a factor up to 5, whilst in a few cases calls are faster by a factor up to 1.4.

Independently of the used computer, we observe a clear hierarchy for the timing of calls under different conditions, and thus for the different elements of our algorithm:

- integration is significantly faster if the q value is the same as in the previous call,
- times for integration at a new value of q increase faster with the number of grid points than times for integration at the same value of q ,

- quadrature is faster than the Levin method, and within the Levin method, an SV decomposition takes more time than an LU decomposition (especially for the q update),
- for a comparable total number of grid points, using subgrids reduces the computation time.

These findings are in line with our expectations formulated in sections 3.2.1 and 3.3. We also note that the time for initialising the integration routine for a specific grid and ν value (step 2 in section 3.3) is well below $100 \mu\text{s}$ in all cases. As expected, this is negligible for the overall computing time budget.

The times in the table are for $J_{\nu-1}$ calls, i.e. they require integration by parts and hence include the matrix multiplication (3.25). Correspondingly, the integration calls for J_ν or $J_{\nu+1}$ are slightly faster, namely between 10% to 20% for integration without update of q .

The integration calls discussed so far are for a single discretised function. For convenience, BESTLIME also provides calls that take one value of q but several discretised functions as arguments and return the vector of integration results. We find no significant difference in timing between N single-function calls (at the same q) and a single call with N functions at once.

5 Numerical studies for TMD-like functions

In this section, we explore in some detail how our method performs for integrals that appear in TMD cross sections. Up to a global factor, such cross sections are proportional to

$$I(q) = \int_0^\infty dz J_0(qz) z W(z, Q) \quad (5.1)$$

where $W(z, Q)$ is product of TMDs evolved to the scale Q . For brevity, we do not display the additional dependence on longitudinal momentum fractions. We will also consider the cumulative q spectrum

$$K(q) = \frac{1}{2\pi} \int d^2\tilde{q} \theta(q - \tilde{q}) I(\tilde{q}) = \int_0^q d\tilde{q} \tilde{q} I(\tilde{q}) = q \int_0^\infty dz J_1(qz) W(z, Q). \quad (5.2)$$

Notice that the integrands in (5.1) and (5.2) have the same behaviour at $z \rightarrow 0$.

We recall that q is a measured transverse momentum and z is a distance between parton fields in the plane transverse to the collision axis in the process. We will therefore give q in units of GeV and z in units in GeV^{-1} (using a system in which the speed of light is unity).

5.1 Integrands

In this subsection, we specify different forms of $W(z, Q)$ used in our numerical study. A reader not familiar with TMDs (but interested in Fourier-Bessel transforms) may skip over the details, but should note two important features of the integrand: (i) it is non-analytic at $z = 0$, and (ii) its leading behaviour at large z is either given by an exponential $\exp(-\kappa z)$ or by a Gaussian $\exp(-\lambda^2 z^2)$.

Our purpose is not a detailed phenomenological investigation of TMDs, but to understand the interplay between their qualitative behaviour and our integration algorithm. We therefore use leading-order evolution and tree-level short-distance matching for the TMDs. For details and references, we refer to [1, chapter 2]. The product of two evolved TMDs has the form

$$W(z, Q) = [f_{\text{np}}(z)]^2 \exp[-2S(z, Q)], \quad (5.3)$$

where

$$\begin{aligned}
S(z, Q) &= \int_{\mu_z}^Q \frac{d\mu}{\mu} \left[4C_F \frac{\alpha_s(\mu)}{2\pi} \ln \frac{Q}{\mu} - 3C_F \frac{\alpha_s(\mu)}{2\pi} \right] \\
&= \left[\frac{c_1}{\alpha_s(Q)} - c_2 \right] \ln \frac{\alpha_s(\mu_z)}{\alpha_s(Q)} - c_1 \left[\frac{1}{\alpha_s(Q)} - \frac{1}{\alpha_s(\mu_z)} \right]
\end{aligned} \tag{5.4}$$

with coefficients

$$c_1 = 8\pi C_F / \beta_0^2, \quad c_2 = 3C_F / \beta_0, \quad \beta_0 = 11 - 2n_f/3, \quad C_F = 4/3 \tag{5.5}$$

and with one-loop running of the strong coupling:

$$\alpha_s(\mu) = \frac{2\pi}{\beta_0 \ln(\mu/\Lambda)}. \tag{5.6}$$

The scale parameter Λ is chosen such that $\alpha_s(M_Z) = 0.13$ at the mass of the Z boson. For simplicity, we take $n_f = 5$ flavours everywhere; a more realistic treatment would not affect the qualitative behaviour of our integrands. The initial conditions for evolution are formulated at the scale

$$\mu_z = b_0 \sqrt{1/z^2 + 1/z_{\max}^2}, \quad b_0 = 2e^{-\gamma} \approx 1.12, \quad z_{\max} = 0.5 \text{ GeV}^{-1}. \tag{5.7}$$

For $z \rightarrow 0$, we have a non-analytic behaviour in z , namely

$$\exp[-2S(z, Q)] \sim \left(\frac{z\Lambda}{b_0} \right)^{8C_F/\beta_0} \left(\ln \frac{b_0}{z\Lambda} \right)^{2c_1/\alpha_s(Q)} \approx \left(\frac{z\Lambda}{b_0} \right)^{1.4} \left(\ln \frac{b_0}{z\Lambda} \right)^{1.14/\alpha_s(Q)}. \tag{5.8}$$

Note that if $f_{\text{np}}(z)$ is sufficiently regular at $z = 0$, the function $zW(z)$ appearing in the integral (5.1) has a finite first derivative at that point.

We performed all numerical studies for three values of Q , namely

$$Q = 2 \text{ GeV}, 20 \text{ GeV}, 100 \text{ GeV}, \tag{5.9}$$

with corresponding values $\alpha_s(2 \text{ GeV}) \approx 0.33$, $\alpha_s(20 \text{ GeV}) \approx 0.17$, and $\alpha_s(100 \text{ GeV}) \approx 0.13$. The resulting power of $\ln(1/z)$ in (5.8) is about 3.5, 6.7, and 8.9, respectively and thus rather high for the two larger Q values.

For the TMDs at scale μ_z , we consider two different forms that have been used in phenomenological analyses. The first one is

$$\begin{aligned}
f_{\text{np, Yukawa}}(z) &= \cosh \left[\left(\frac{2c^2}{\kappa} - \frac{\kappa}{4} \right) z \right] / \cosh \left[\left(\frac{2c^2}{\kappa} + \frac{\kappa}{4} \right) z \right], \quad \kappa = 0.642 \text{ GeV}, \\
& \quad c = 0.521 \text{ GeV}
\end{aligned} \tag{5.10}$$

and corresponds to equation (3.7) and the first line of table 12 in [6]. At large z this has a Yukawa-type behaviour like $\exp(-\kappa z/2)$. The second form has a Gaussian behaviour and reads

$$f_{\text{np, Gauss}}(z) = (1 - c^2 z^2) \exp(-\lambda^2 z^2/2), \quad \lambda = 0.374 \text{ GeV}, \quad c = 0.117 \text{ GeV}. \tag{5.11}$$

This was used in the study [23], see equation (34) and table XI in that paper. Notice that we define the parameters κ and λ such that the *squared* TMDs and hence the integrands in (5.1) and (5.2) decrease like $\exp(-\kappa z)$ or $\exp(-\lambda^2 z^2)$.

In addition to these ‘‘Yukawa’’ and ‘‘Gauss’’ TMDs, we also consider the ‘‘toy TMD’’ investigated in [8], which corresponds to

$$zW_{\text{toy}}(z) = \frac{1}{\Gamma(\beta^2/\sigma^2)} \left(\frac{\beta z}{\sigma^2}\right)^{\beta^2/\sigma^2} \exp\left[-\frac{\beta z}{\sigma^2}\right]. \quad (5.12)$$

This has the same form as the first entry in our table 2, with an exponential decay parameter $\kappa = \beta/\sigma^2$. The function $W_{\text{toy}}(z)$ takes its maximum when $1/z$ is equal to

$$Q = \frac{\beta}{\beta^2 - \sigma^2}, \quad (5.13)$$

which in [8] was taken as a representative of the physical scale Q of a hard process in this simplified TMD setup. We choose the parameters in (5.12) as

$$\beta/\sigma^2 = \kappa = 0.642 \text{ GeV}, \quad \beta = 1/\kappa + 1/Q, \quad (5.14)$$

thus taking the same value of κ as in (5.10) for all Q .

Unless specified otherwise, the plots in the present section are obtained with the following interpolation grids:

$$\begin{array}{ll} \text{exp sqrt grid with } [0, z_1, \infty]_{(16,32)} & \text{for the toy and Yukawa TMDs,} \\ \text{exp grid with } [0, z_1, \infty]_{(16,32)} & \text{for the Gauss TMD.} \end{array} \quad (5.15)$$

It is natural to specify the mass parameters m in the grid transformations (see table 1) as multiples of the characteristic exponential decay parameter of the integrands. We therefore define

$$\begin{array}{ll} r_\kappa = m/\kappa & \text{for the toy and Yukawa TMDs,} \\ r_\lambda = m/\lambda & \text{for the Gauss TMD.} \end{array} \quad (5.16)$$

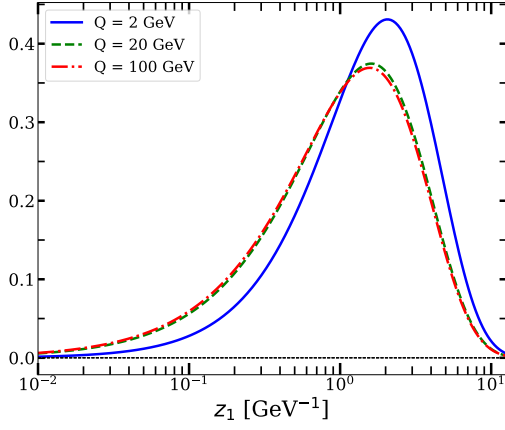
Our default grid parameters are

$$\begin{array}{lll} z_1 = 0.05, & r_\kappa = 3 & \text{for the toy and Yukawa TMDs,} \\ z_1 = 0.05, & r_\lambda = 5 & \text{for the Gauss TMD} \end{array} \quad (5.17)$$

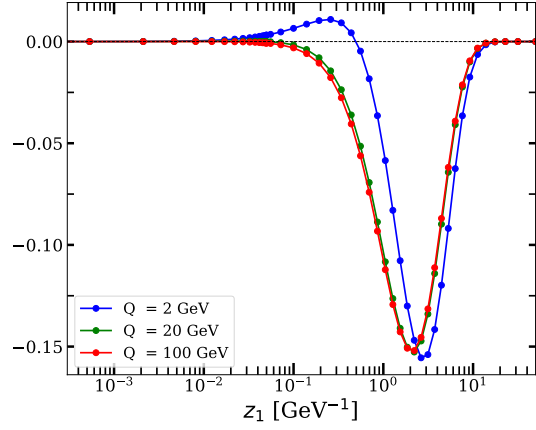
and have been chosen such that one obtains good integration accuracy for all three Q values in (5.9), see table 5 and the plots in section 5.2.3.

The functions $zW(z)$, which multiply $J_0(qz)$ in the integral $I(q)$, are plotted on the l.h.s. of figure 4. When computing $I(q)$, integration by parts is used as specified in (3.5), and the resulting function $f_1(z)$ that appears in the master equation of the Levin method (3.2) is shown on the r.h.s. of the figure. We see non-trivial structures of $f_1(z)$ appearing as a consequence of taking the derivative and weighting with powers of $z/(1+z)$. The points on the curves for $f_1(z)$ correspond to the interpolation grids just specified.

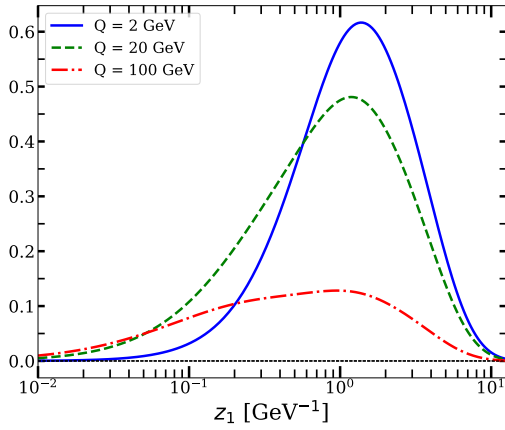
The Fourier-Bessel transform $I(q)$, which gives the transverse-momentum spectrum of the TMD process, is shown in figure 5. We observe that the transform becomes negative at some value $q \sim Q$. This is a clear indication that TMD factorisation does not describe the cross section in such a region. We recall from the introduction that the evaluation of $I(q)$ may however be necessary even in that region, in order to achieve a smooth transition between the TMD regime and the regime in which the cross section can be computed in terms of collinear parton distributions and fixed-order perturbative cross sections.



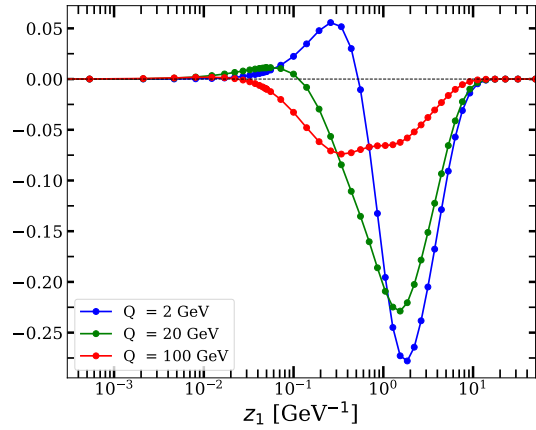
(a) $zW(z)$, toy TMD



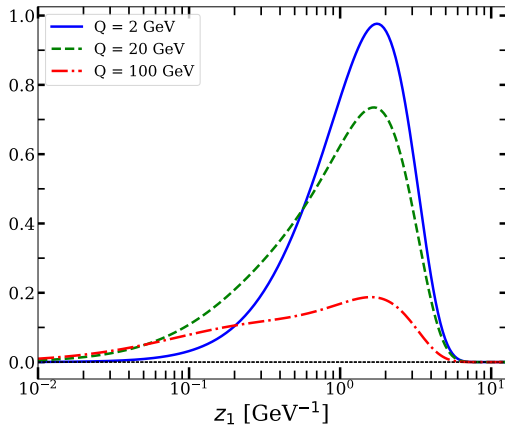
(b) $f_1(z)$, toy TMD



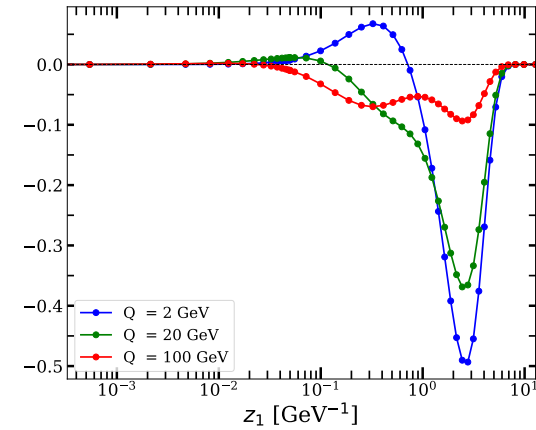
(c) $zW(z)$, Yukawa TMD



(d) $f_1(z)$, Yukawa TMD



(e) $zW(z)$, Gauss TMD



(f) $f_1(z)$, Gauss TMD

Figure 4: Left: the transformed function $zW(z)$ in (5.1) for different values of Q and the three choices of TMDs specified in the text. Right: the corresponding function $f_1(z)$ in our method, see equations (3.2) and (3.5). The points on the curves correspond to the interpolation grids specified by (5.15) and (5.17).

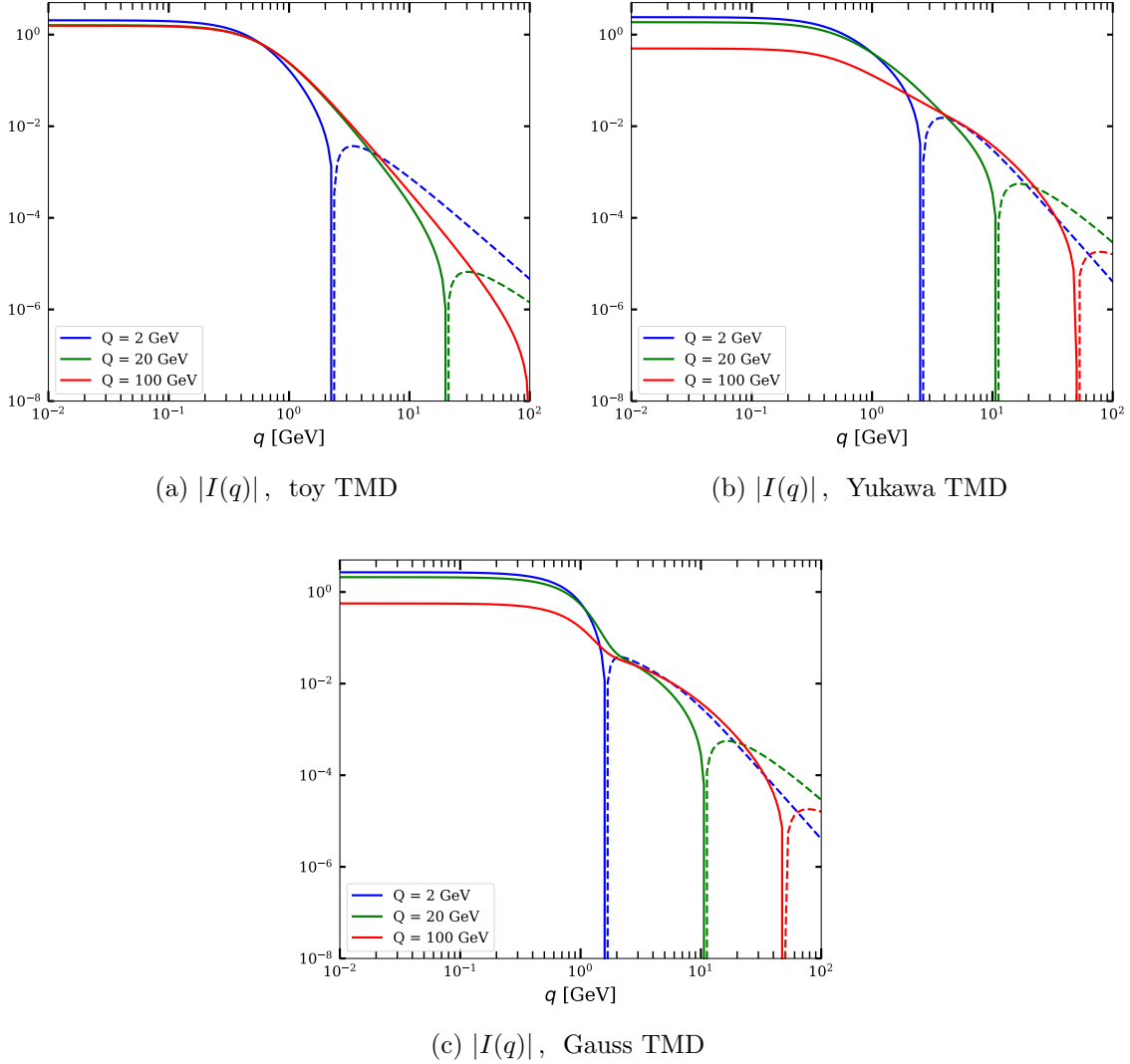


Figure 5: Absolute values of the Fourier-Bessel transform $I(q)$ for the functions $zW(z)$ shown on the l.h.s. of figure 4. Dashed lines indicate that $I(q)$ is negative. The curve for $Q = 100$ GeV in panel (a) has a zero crossing at q between 100 and 101 GeV.

5.2 Choosing interpolation grids

We now compare the performance of different settings for the interpolation grids in our method. We generally find that high accuracy is easier to reach for $K(q)$ than for $I(q)$, which is why we mostly focus on $I(q)$ in the following.

To quantify the performance of a particular grid setting for a given choice of $W(z)$, we evaluate the Fourier-Bessel integrals for a set of logarithmically spaced values q_i between 0.01 GeV and 100 GeV. We then determine the root mean square of the relative integration error ε , averaging over all q_i that are not too close to the point q_0 where $I(q)$ has a zero crossing. Specifically, we define

$$\varepsilon_{\text{rms}}^2 = \langle \varepsilon^2 \rangle_{q_i \notin R}, \quad \text{with } R = (q_0 - \Delta, q_0 + \Delta), \quad (5.18)$$

where

$$\Delta = \begin{cases} 1 \text{ GeV} & \text{for } Q = 2 \text{ GeV}, \\ 5 \text{ GeV} & \text{for } Q = 20 \text{ GeV}, \\ 10 \text{ GeV} & \text{for } Q = 100 \text{ GeV}. \end{cases} \quad (5.19)$$

To compute the integration error, we take the analytic form of the Fourier-Bessel transform for the toy TMD (see table 2) and the result of an adaptive Gauss-Kronrod integrator for the Yukawa and Gauss TMDs.⁵

5.2.1 Variable transformations

We begin with a comparison between different variable transformations, fixing the grid structure to the form $[0, z_1, \infty]_{16,32}$. For each transformation we need to choose parameters (z_1, r_κ) or (z_1, r_λ) . We do this by performing a parameter scan in these values, with $z_1 \in [0.01, 0.3]$ in steps of 0.01 and with r_κ or r_λ varying from 0.25 to 8 in steps of 0.25. The parameters that give the smallest value of ε_{rms} are listed in table 5.

The relative integration error for the best parameter setting is shown in figure 6 as a function of q . We see that for the TMDs with an exponential falloff (toy and Yukawa TMD) the `exp sqrt` transform performs somewhat better than the `exp` transform. In turn, for the Gauss TMD, the `exp` transform performs much better than the `Gauss` transform. We note that in both cases, the preferred transformation is the one that leads to a stronger decrease of the integrand for $u \rightarrow 0$ (which corresponds to $z \rightarrow \infty$). We use this preferred transformation in all subsequent comparisons.

5.2.2 Number of subgrids

Let us now compare the accuracy of our algorithm with one, two, or three subgrids for a comparable total number of points. As in the previous subsection, we determine the best parameter settings for each grid by a parameter scan; the resulting values are given in table 5. We note in passing that for a single subgrid, the preferred values of r_κ or r_λ are much larger than with two or more subgrids.

More importantly, we find that for our integrands and q values, two subgrids are strongly preferred, as seen in figures 7 and 8. We hence adopt this setting for the subsequent investigations. We also tried settings with two subgrids and a different partition (n_1, n_2) for the number of grid points, finding no significant improvement compared to the choice (16, 32).

5.2.3 Transformation parameters and number of grid points

Our method would be of limited practical use if its accuracy changed rapidly with the choice of grid parameters, since this would require a detailed parameter scan for each new integrand. Fortunately, this is not the case, as we will show now.

Figures 9 to 11 show the dependence of the relative integration error on the parameters z_1 and r_κ or r_λ . They give the *worst* accuracy for all q_i values away from the zero crossing of $I(q)$, i.e.

$$\varepsilon_{\text{max}} = \max_{q_i \notin R}(\varepsilon) \quad \text{with } R = (q_0 - \Delta, q_0 + \Delta), \quad (5.20)$$

where Δ is given in (5.19). We obtain very similar plots for ε_{rms} defined in (5.18). Note that ε_{max} is a more stringent measure for the performance of a parameter setting.

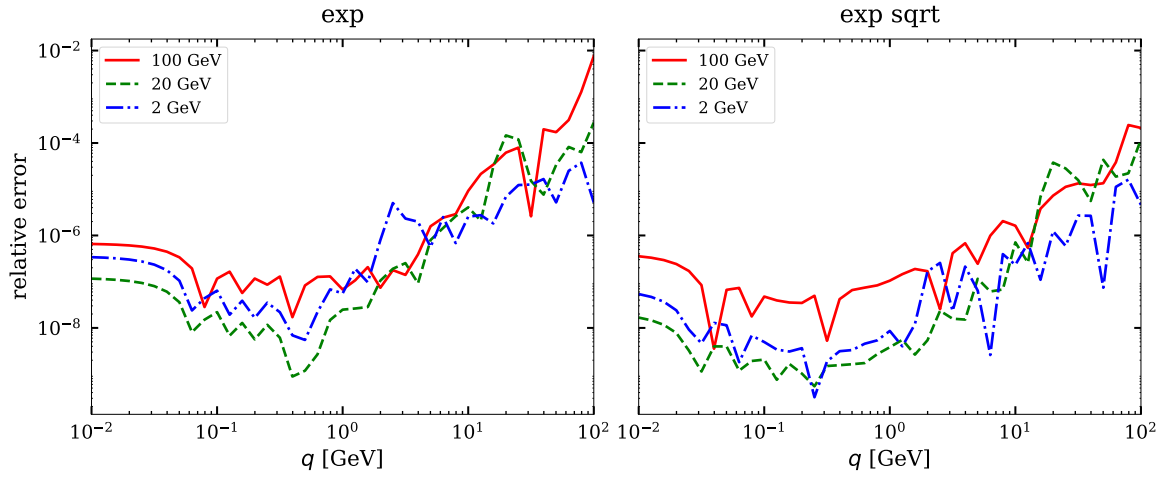
⁵We use the routine `scipy.integrate.quad` of SciPy version 1.7.3, which employs the QAGS algorithm of the QUADPACK library [24]. The relative target accuracy is set to 10^{-12} .

toy TMD				
Q[GeV]	exp	exp sqrt		
	(z_1, r_κ)	r_κ	(z_1, r_κ)	(z_1, z_2, r_κ)
2	(0.15, 1.0)	7.0	(0.1, 2.0)	(0.1, 1.0, 1.5)
20	(0.15, 1.0)	4.0	(0.1, 2.0)	(0.1, 1.5, 1.5)
100	(0.05, 1.5)	6.0	(0.05, 3.0)	(0.05, 0.5, 1.0)

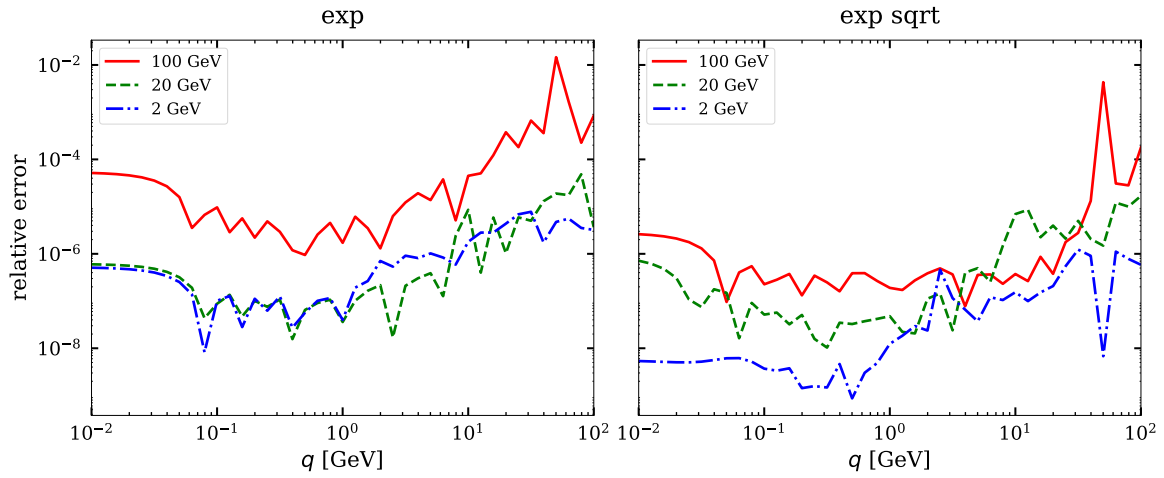
Yukawa TMD				
Q[GeV]	exp	exp sqrt		
	(z_1, r_κ)	r_κ	(z_1, r_κ)	(z_1, z_2, r_κ)
2	(0.1, 1.5)	8.0	(0.1, 2.0)	(0.1, 1.0, 1.5)
20	(0.15, 1.5)	8.0	(0.1, 2.0)	(0.1, 0.8, 1.5)
100	(0.05, 1.0)	10.0	(0.05, 4.0)	(0.05, 0.8, 6.0)

Gauss TMD				
Q[GeV]	Gauss	exp		
	(z_1, r_λ)	r_λ	(z_1, r_λ)	(z_1, z_2, r_λ)
2	(0.15, 1.5)	8.0	(0.1, 3.0)	(0.2, 3.0, 5.0)
20	(0.15, 1.5)	7.0	(0.1, 4.0)	(0.1, 1.0, 4.0)
100	(0.05, 2.0)	4.0	(0.05, 5.0)	(0.15, 1.2, 7.0)

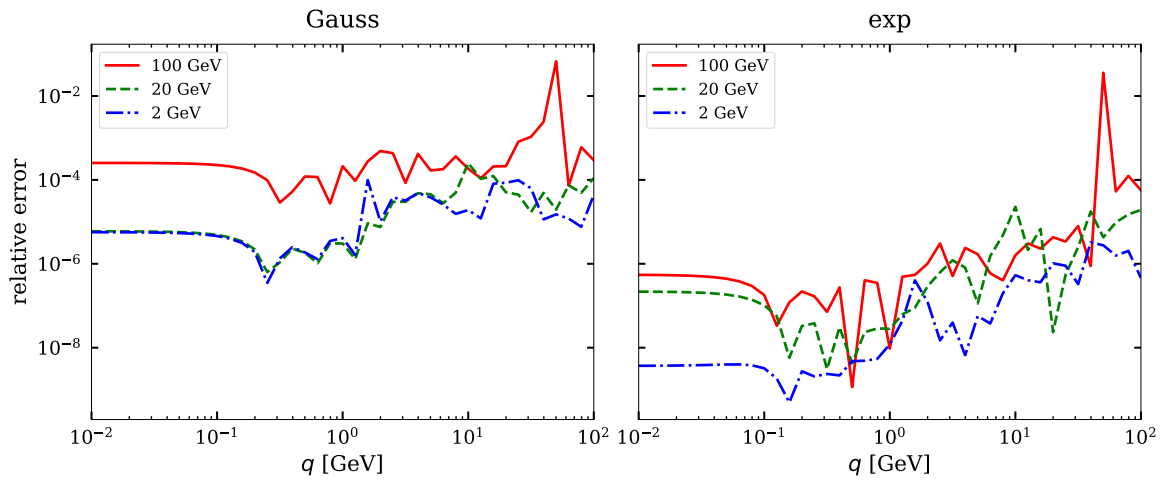
Table 5: Grid parameter values used for the plots in figures 6 to 8. These values give the best average integration error ε_{rms} in a parameter scan. The labels **exp**, **exp sqrt**, and **Gauss** refer to the variable transformations in table 1. The corresponding grids have the structure $[0, \infty]_{(48)}$ for one parameter, $[0, z_1, \infty]_{(16,32)}$ for two parameters, and $[0, z_1, z_2, \infty]_{(16,16,16)}$ for three parameters. z_1 and z_2 are given in units of GeV^{-1} .



(a) Toy TMD

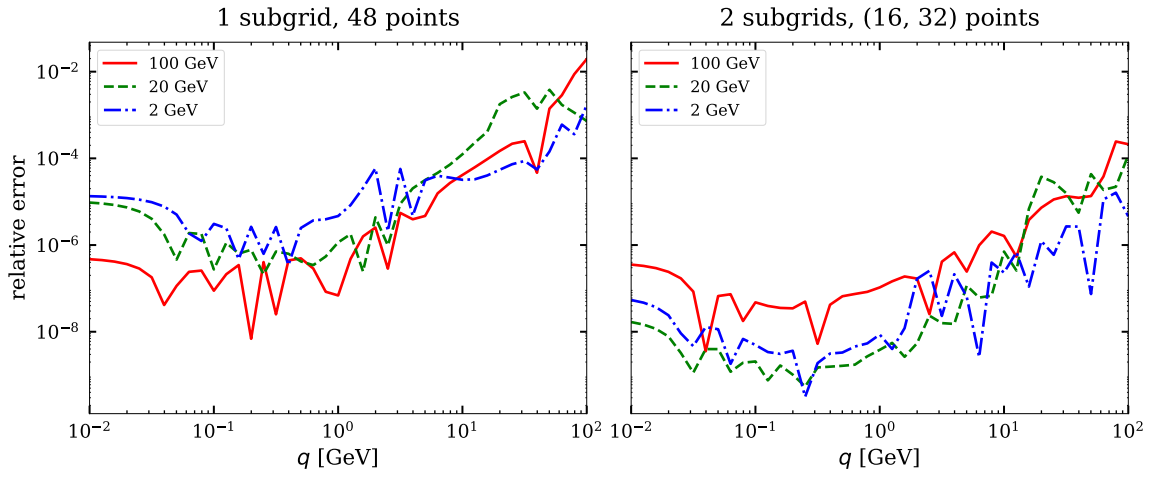


(b) Yukawa TMD

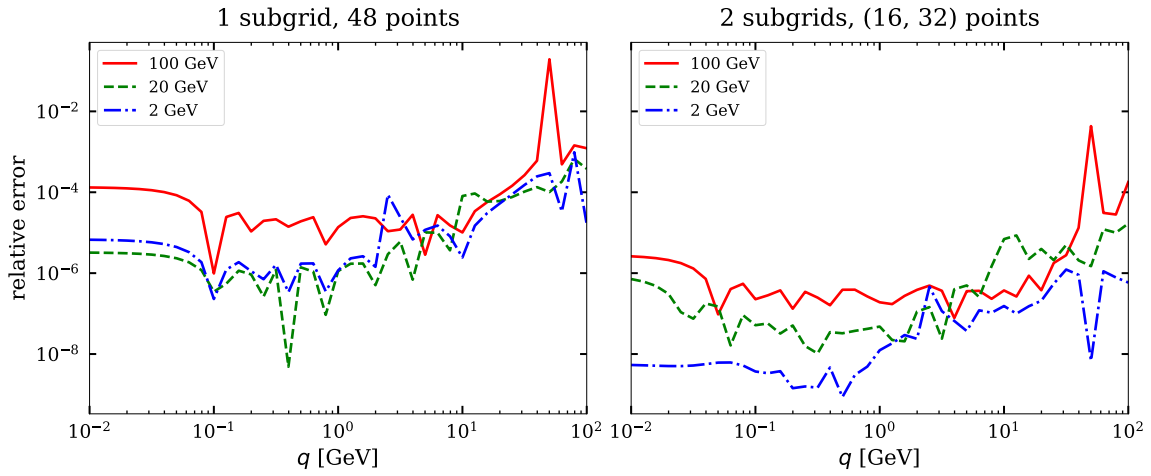


(c) Gauss TMD

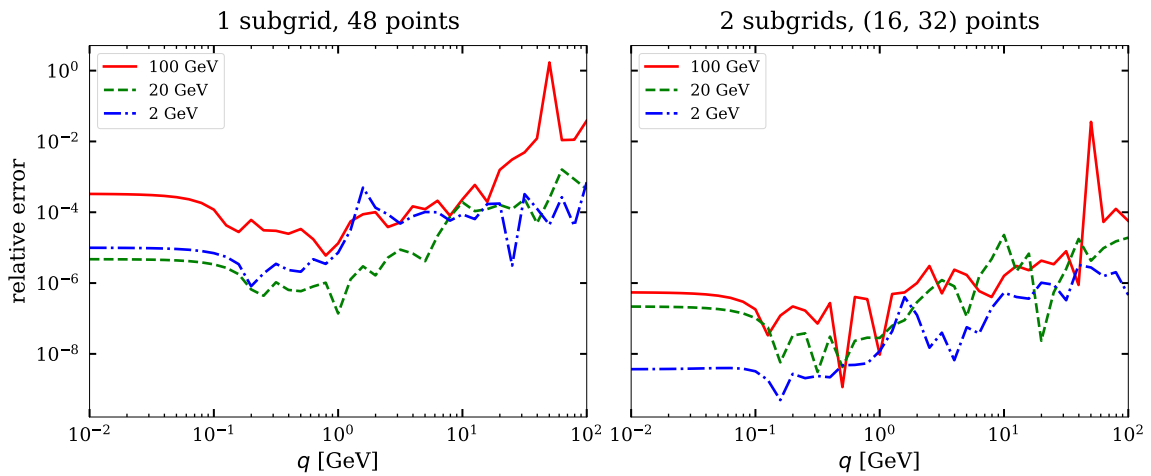
Figure 6: Relative integration error achieved with different variable transforms on grids of the form $[0, z_1, \infty]_{(16,32)}$. Details are given in the text.



(a) toy TMD

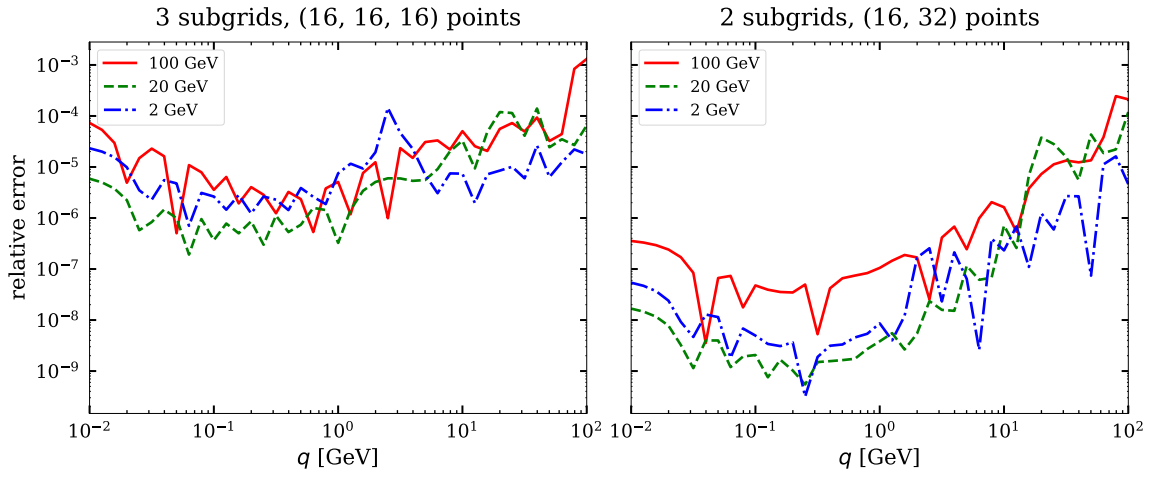


(b) Yukawa TMD

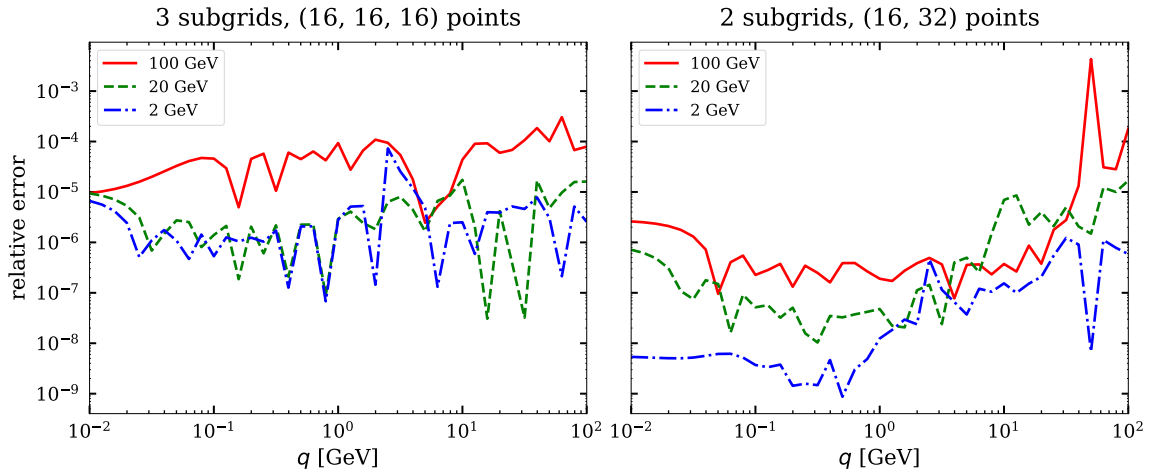


(c) Gauss TMD

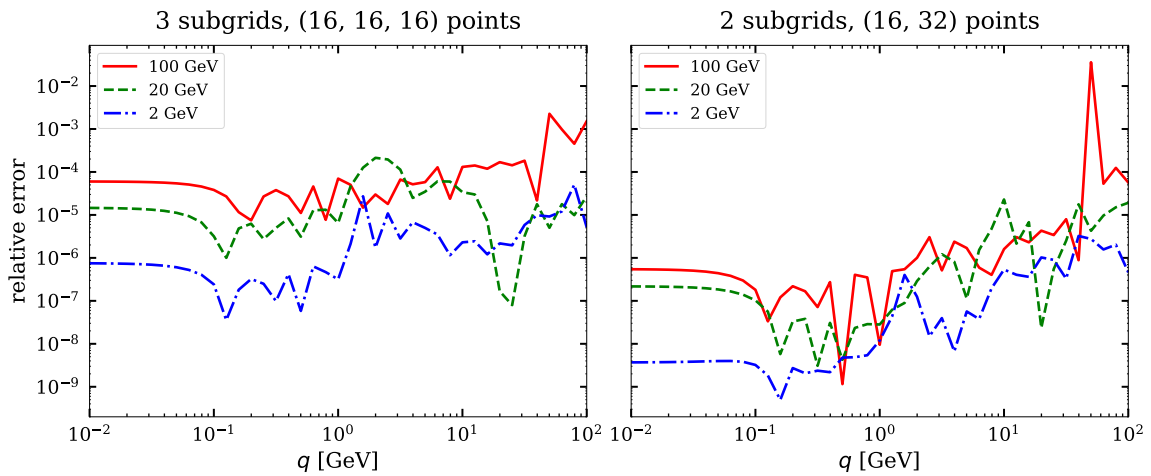
Figure 7: Relative integration error for grids of the form $[0, \infty]_{(48)}$ (left) and $[0, z_1, \infty]_{(16,32)}$ (right). The variable transform for a given TMD is as in the right panels of figure 6.



(a) toy TMD



(b) Yukawa TMD



(c) Gauss TMD

Figure 8: The same as figure 7, but for grids of the form $[0, z_1, z_2, \infty]_{(16,16,16)}$ (left) and $[0, z_1, \infty]_{(16,32)}$ (right).

We see in figures 9 and 10 that the best accuracy for $I(q)$ at $Q = 2$ or 20 GeV is obtained with z_1 between 0.05 and 0.15 GeV $^{-1}$ and with r_κ or r_λ between 2 and 4 . For $Q = 100$ GeV, the region of favourable parameters is somewhat shifted, with z_1 between 0.05 and 0.10 GeV $^{-1}$ and with r_κ or r_λ between 4 and 6 . The parameter region of good accuracy for $K(q)$ is much wider in r_κ or r_λ and includes the good region for $I(q)$. Corresponding plots for the toy TMD are similar to those for the Yukawa TMD and not shown here.

With fewer grid points, namely $(12, 24)$ instead of $(16, 32)$, we find that the favourable parameter regions become smaller, as is shown in the left panels of figure 11. Still, a relative accuracy of 10^{-3} or better can be achieved in the same parameter region that is preferred for $(16, 32)$ points. In the right panels of figure 11 we see that with even more points, namely $(24, 48)$, the favourable parameter region becomes much wider, although for $Q = 100$ there is still a clear preference for low z_1 . The corresponding plots for the Yukawa and the toy TMD look quite similar and are not shown here.

5.3 Estimating the integration error

To determine whether a particular grid setup in our method is satisfactory, one needs a practical method to estimate the integration accuracy. A straightforward way to achieve this is to re-compute the integral with twice as many points on each subgrid, keeping all other settings the same. We have evaluated the corresponding error estimates for the grids $[0, z_1, \infty]_{(16,32)}$ and $[0, \infty]_{(48)}$, both for the the best and for the worst parameter settings identified in our parameter scans. A selection of our results is shown in figure 12.

In general we find that the error estimates so obtained are extremely close to the actual integration errors. The only notable exception to this statement is shown in the top left panel, where we see that for most q values the error is *underestimated* by doubling the number of points. Since this problem appears in a region where the actual relative error is well below 10^{-6} , we consider it to be of minor importance in practice. We therefore do not pursue this issue further here.

We also observe that sometimes the error estimate fails only at specific q values, as seen in the bottom left panel. This happens when the difference between approximate and exact integrals has a zero crossing as a function of q . As long as one monitors the error estimate also in the vicinity of such points, this should not pose any problem.

5.4 Comparison with the method of Kang et al.

Let us finally compare our method with the algorithm of Kang et al. [8], which implements the Ogata method [5] with a particular optimisation of the parameter h that controls the density of integration nodes. We use the C++ implementation of the algorithm that links to the GSL library, see <https://github.com/UCLA-TMD/Ogata> for details. The optimisation algorithm requires an estimate for the value of x at which the function $x^2 W(x/q)$ takes its maximum; we verified that our results are stable with respect to variations of this parameter. The other input parameter to the algorithm is the number N of function calls to $W(z)$.

For our method, we take the preferred parameter transform for each TMD, together with a grid $[0, z_1, \infty]_{(n_1, n_2)}$ with our default grid parameters (5.17). For a total number N of grid points, and thus of calls to the function $W(z)$, we take $n_1 = \text{floor}(N/3) + 1$ and $n_2 = N - \text{floor}(N/3)$ points on the respective subgrids. We recall that the grid parameters in (5.17) were determined for $(n_1, n_2) = (16, 32)$, i.e. for $N = 47$.

When comparing the accuracy of the two algorithms at the same value of N , one should bear in mind that with our method the computation of $W(z)$ at N values of z allows one to evaluate the Fourier-Bessel transform for a broad range of q values, which is not the case for

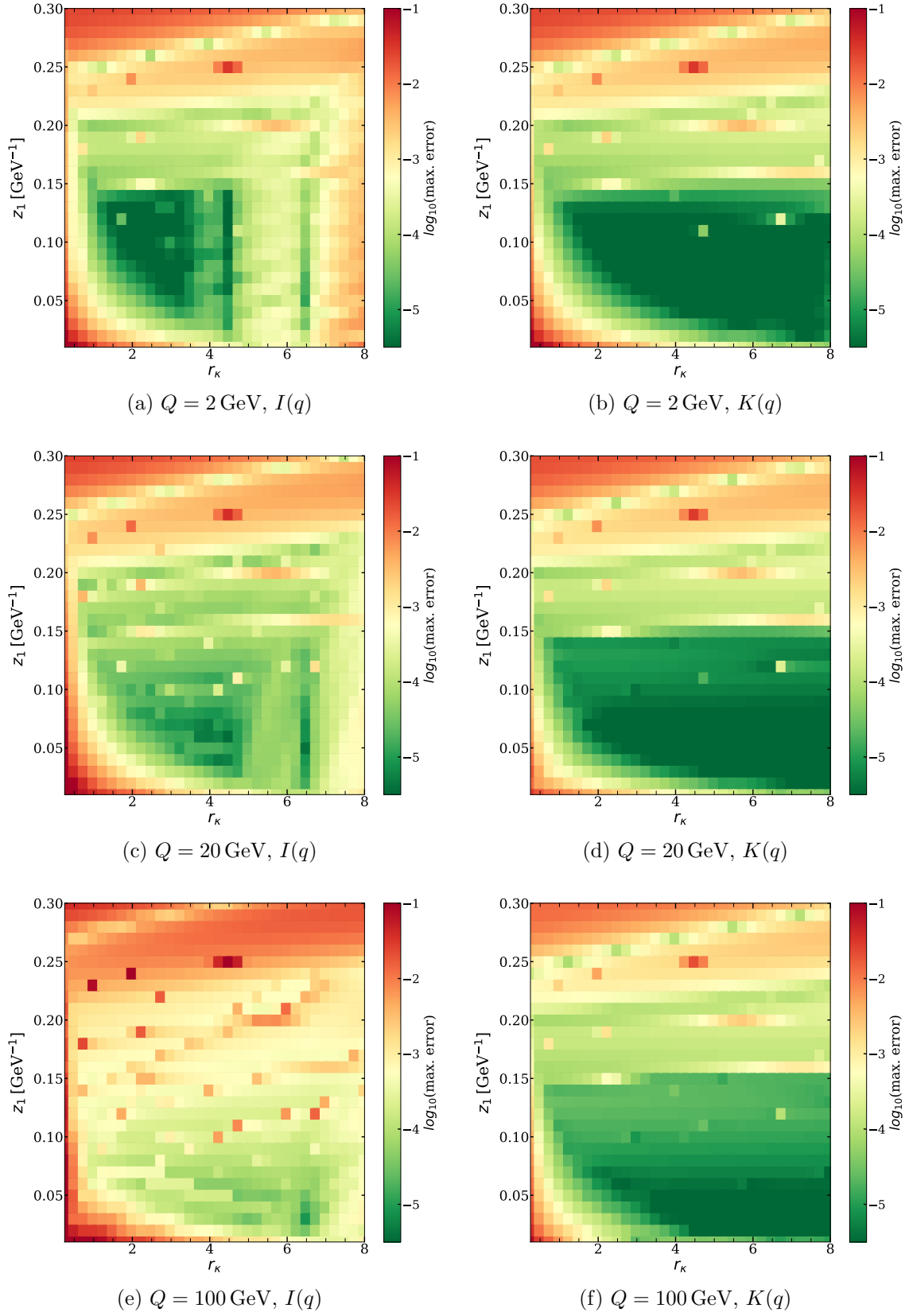


Figure 9: The relative integration error ε_{\max} defined in (5.20), evaluated for the Yukawa TMD as a function of the grid parameters with our default grid structure $[0, z_1, \infty]_{(16,32)}$. The accuracy for $I(q)$ is shown on the left and the one for $K(q)$ on the right.

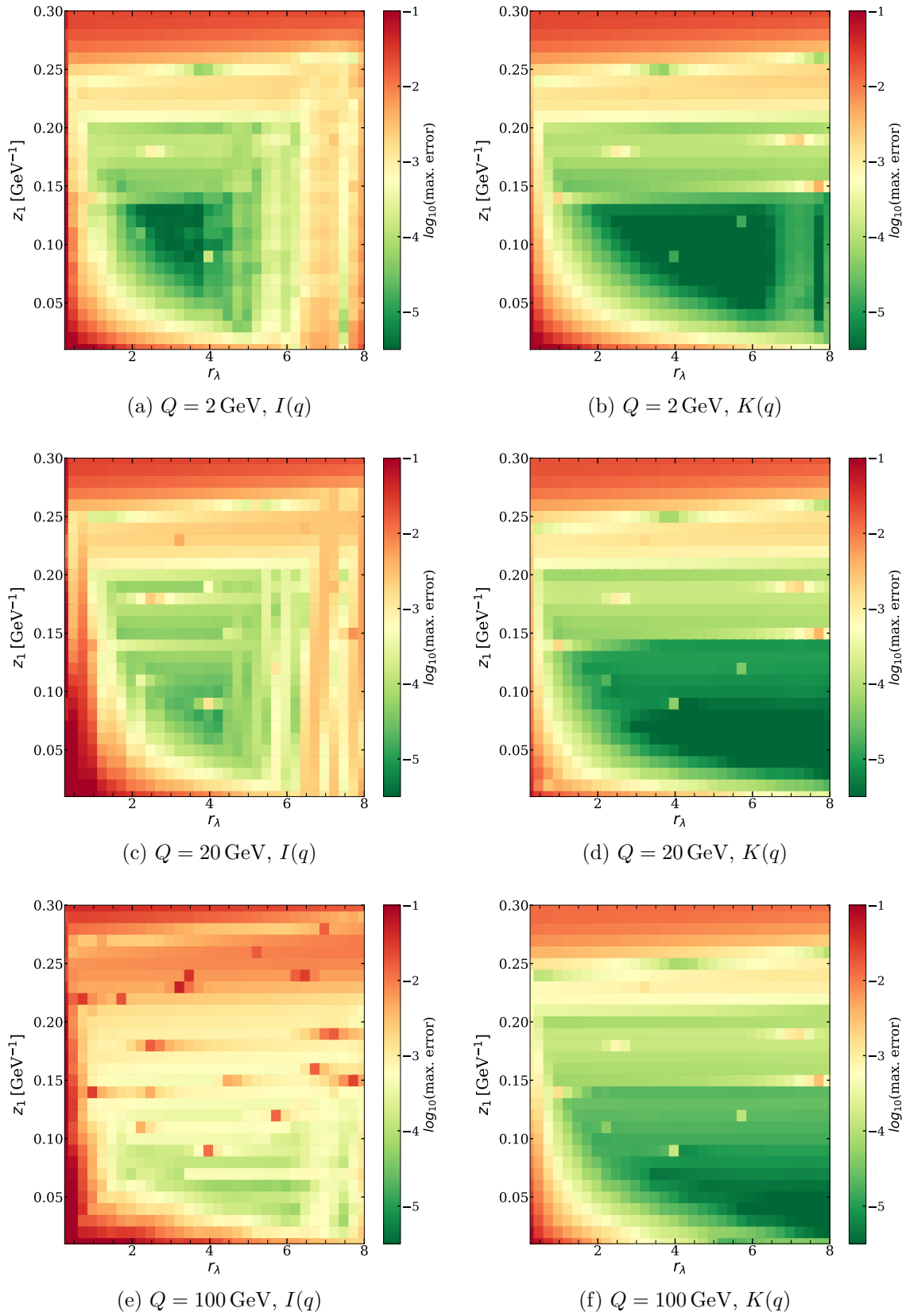


Figure 10: As figure 9, but for the Gauss TMD.

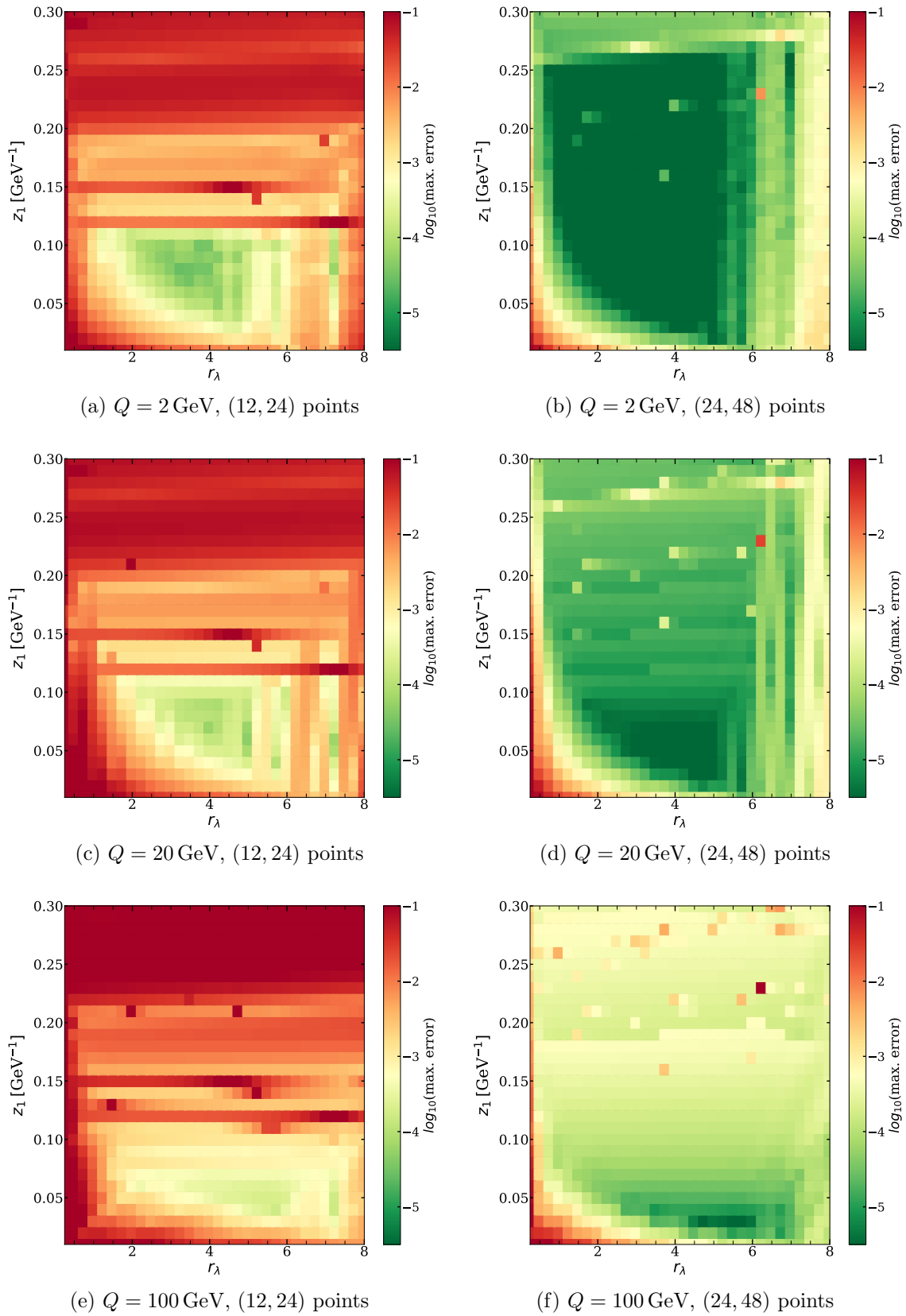
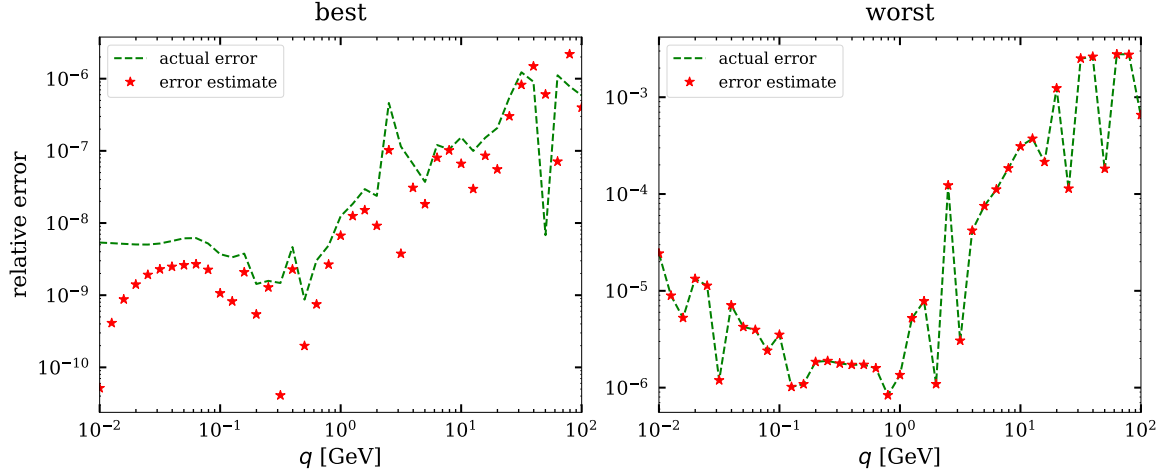
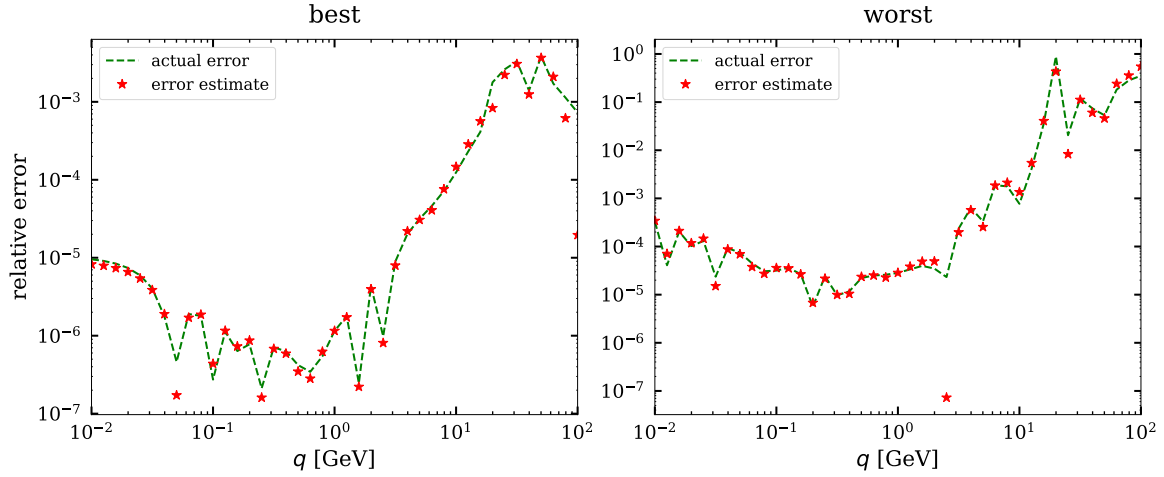


Figure 11: The relative integration error ε_{\max} of $I(q)$ for the Gauss TMD, evaluated with fewer or more grid points than in the left panels of figure 10.



(a) Yukawa TMD, $Q = 2 \text{ GeV}$, two subgrids $[0, z_1, \infty]_{(16,32)}$



(b) Toy TMD, $Q = 20 \text{ GeV}$, one subgrid $[0, \infty]_{(48)}$

Figure 12: Actual and estimated relative integration accuracy, as described in the text. The left panels are for the best setting of the corresponding parameter scan and the right panels for the worst one. The worst setting in the upper row is $(z_1, r_\kappa) = (0.03, 1.0)$, the worst setting in the lower row is $r_\kappa = 0.5$. The best settings are given in table 5.

the Ogata method. We nevertheless use N as a measure of the computational cost in both cases.

The following plots show the accuracy achieved for the toy and Gauss TMDs. The corresponding accuracy for the Yukawa TMD is typically between these two cases, both for our method and the one of [8]. We omit this in our plots for the sake of clarity.

We see in figure 13 that for low q the algorithm of [8] works very well. It often performs better than our method for small N . The situation is very different for $q = 20$ GeV and $q = 100$ GeV, as shown in figure 14. With $N = 60$ points our method achieves relative errors below 10^{-4} , except for the toy TMD at $q = Q = 100$ GeV, where $I(q)$ is close to its zero crossing. By contrast, the algorithm of [8] requires a much higher number of nodes for $q = 20$ GeV (well above 100 for the toy TMD), and at $q = 100$ GeV, no satisfactory result is obtained for the toy TMD even with 320 nodes.

We observe that the intermediate parameter h_u in the optimisation procedure of Kang et al. grows linearly with q until it reaches its maximum allowed value $h_{\max} = 2$. As discussed in section 2 of [8], the value of h_u used in the algorithm is increasingly far away from its optimum as q increases, and a reliable result can then only be achieved by increasing the number N of function calls.

In summary, we find that both methods require more grid points as q increases, but that these requirements are much less severe for our method.

6 Formally divergent integrals

In this section, we take a closer look at Fourier-Bessel integrals from 0 to ∞ with integrands that do not decrease at large z . The integrals we have considered so far are either absolutely convergent, or they can be defined as

$$\int_0^\infty dz J_\nu(z) \tilde{f}(z) = \lim_{z_b \rightarrow \infty} \int_0^{z_b} dz J_\nu(z) \tilde{f}(z). \quad (6.1)$$

The situation is more complicated if $\tilde{f}(z)$ grows like \sqrt{z} or faster at large z . An example is the case $\nu = 0$ and $\tilde{f}(z) = z$, where

$$\int_0^{z_b} dz J_0(qz) z = \frac{z_b}{q} J_1(qz_b) \quad (6.2)$$

diverges at $z_b \rightarrow \infty$ for any $q > 0$, whereas the integral up to ∞ can be defined as a distribution

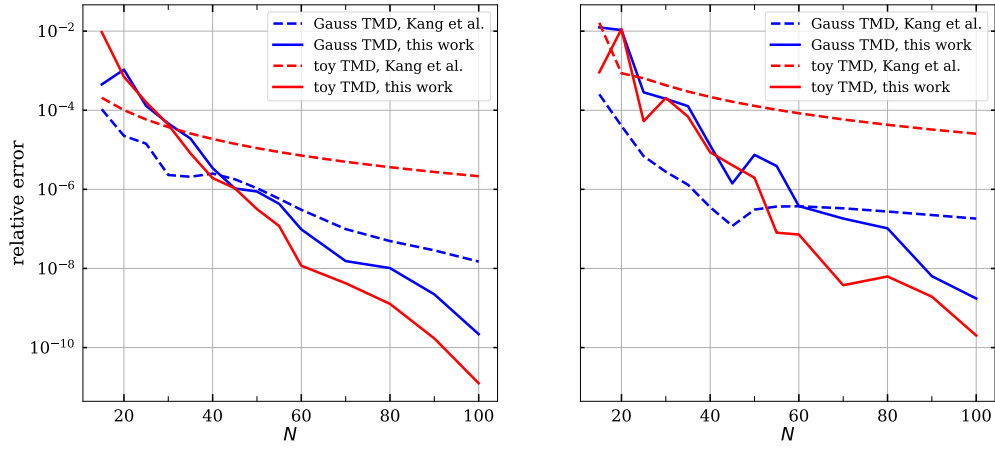
$$\int_0^\infty dz J_0(qz) z = \frac{\delta(q)}{q} = 2\delta(q^2). \quad (6.3)$$

The latter relation can be obtained from the representation of a two-dimensional δ distribution as the Fourier transform of a constant.

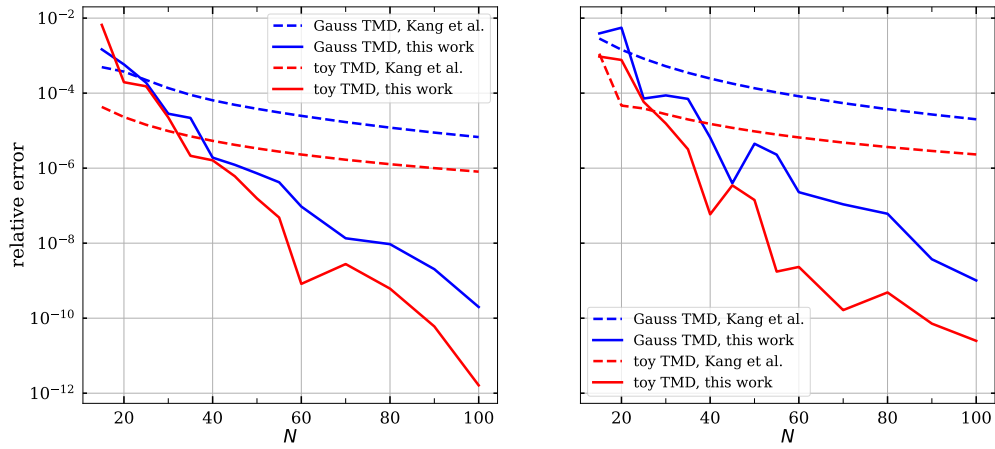
In the context of TMD studies, one encounters Fourier-Bessel transforms with functions $\tilde{f}(z)$ increasing even faster than z . Writing the fixed-order perturbative cross section up to order α_s^n as a Fourier-Bessel integral, one gets an integrand of the form $J_0(qz)$ times

$$\tilde{f}(z) = z \sum_{k=0}^{2n} c_k \ln^k(zQ) \quad (6.4)$$

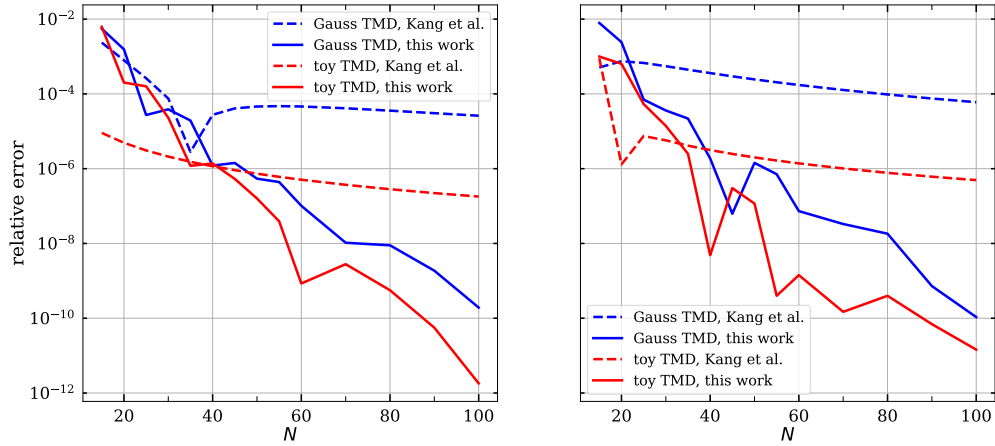
with coefficients c_k that are independent of z . The corresponding integral can be defined in the sense of distributions, see [25, appendix C] for a systematic investigation and [26, appendix B] for an earlier reference.



(a) $Q = 2 \text{ GeV}$, $q = 0.01 \text{ GeV}$ (left) and $q = 2 \text{ GeV}$ (right)

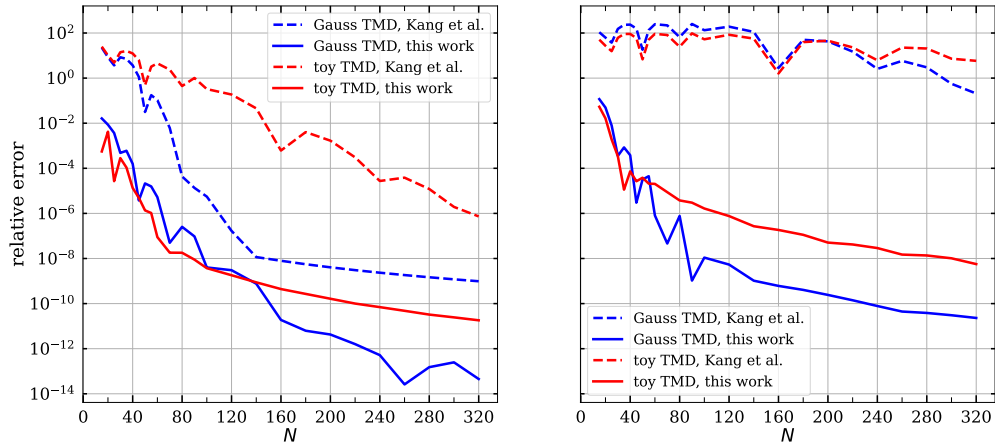


(b) $Q = 20 \text{ GeV}$, $q = 0.01 \text{ GeV}$ (left) and $q = 2 \text{ GeV}$ (right)

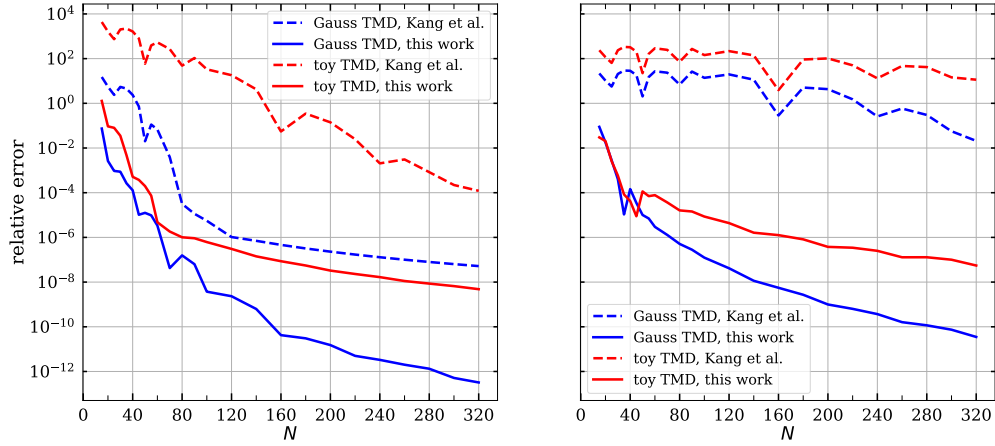


(c) $Q = 100 \text{ GeV}$, $q = 0.01 \text{ GeV}$ (left) and $q = 2 \text{ GeV}$ (right)

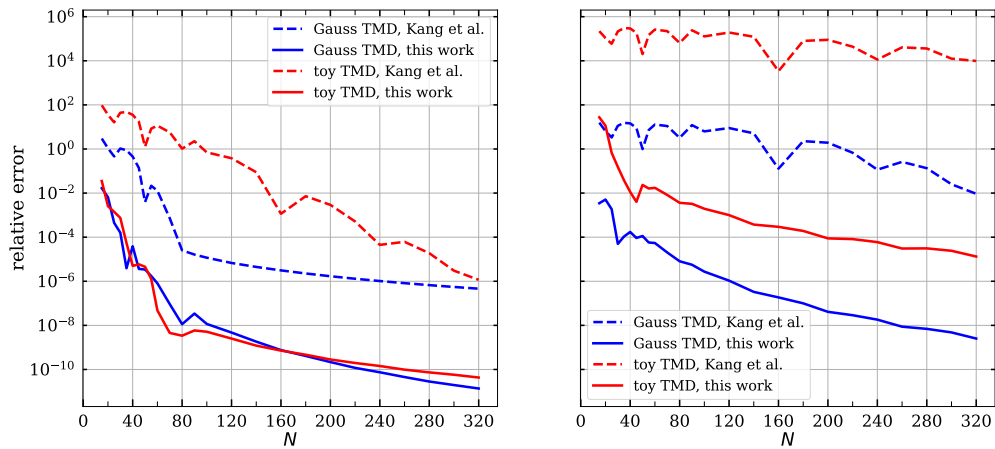
Figure 13: Comparison of our method with the algorithm of Kang et al. at $q = 0.01 \text{ GeV}$ (left) and $q = 2 \text{ GeV}$ (right) for different values of Q . The relative integration error is evaluated for N calls to the function $W(z)$, with N varying in steps of 5 or 10. Continuous curves are shown as a guide for the eye.



(a) $Q = 2$ GeV, $q = 20$ GeV (left) and $q = 100$ GeV (right)



(b) $Q = 20$ GeV, $q = 20$ GeV (left) and $q = 100$ GeV (right)



(c) $Q = 100$ GeV, $q = 20$ GeV (left) and $q = 100$ GeV (right)

Figure 14: As figure 13 but for $q = 20$ GeV (left) and $q = 100$ GeV (right). N varies in steps of 20 for $N \geq 100$.

As shown in the papers just quoted, the Fourier-Bessel transform of (6.4) can be carried out analytically, but this is no longer true for more complicated cases. For instance, the method of [4] involves a smooth interpolation between the form (6.4) at $q \sim Q$ and an expression including all-order resummation at $q \ll Q$. In this scheme, the function f depends on both z and q . It generically has a rather complicated form, and numerical integration is required to compute its Fourier-Bessel transform.

These considerations motivate us to extend our method to integrands that increase with z . We do this for general $\nu \geq 0$, which presents only a modest overhead compared with the case $\nu = 0$ required for the physics application just sketched.

6.1 Defining the integral

In the following we consider functions that satisfy

$$z^\nu \left(z \frac{d}{dz} \right)^k \tilde{f}(z, q) \xrightarrow{z \rightarrow 0} \text{const}, \quad z^{-3/2} \left(z \frac{d}{dz} \right)^k \tilde{f}(z, q) \xrightarrow{z \rightarrow \infty} 0 \quad \text{for } k = 0, 1, 2, \quad (6.5)$$

where it is understood that *const* may be finite or zero. If \tilde{f} depends on q , we also require that

$$z^\nu \frac{d}{dq} \tilde{f}(z, q) \xrightarrow{z \rightarrow 0} \text{const}, \quad z^{-3/2} \frac{d}{dq} \tilde{f}(z, q) \xrightarrow{z \rightarrow \infty} 0 \quad (6.6)$$

and

$$\frac{d}{dz} \frac{d}{dq} \tilde{f}(z, q) = \frac{d}{dq} \frac{d}{dz} \tilde{f}(z, q). \quad (6.7)$$

The integral of interest is

$$I(q) = \int_0^\infty dz J_\nu(qz) \tilde{f}(z, q) \quad (6.8)$$

with $\nu \geq 0$. The relation (A.2) for Bessel functions of the first kind implies

$$J_\nu(qz) = \frac{1}{z} \frac{1}{q^{\nu+1}} \frac{d}{dq} [q^{\nu+1} J_{\nu+1}(qz)], \quad (6.9)$$

which gives

$$I(q) = \frac{1}{q^{\nu+1}} \int_0^\infty dz \frac{d}{dq} \left[q^{\nu+1} J_{\nu+1}(qz) \frac{\tilde{f}(z, q)}{z} \right] - \int_0^\infty dz J_{\nu+1}(qz) \frac{d}{dq} \frac{\tilde{f}(z, q)}{z} \quad (6.10)$$

when inserted into (6.8). Interchanging differentiation and integration, we get

$$I(q) = \frac{1}{q^{\nu+1}} \frac{d}{dq} \left[q^{\nu+1} \int_0^\infty dz J_{\nu+1}(qz) \frac{\tilde{f}(z, q)}{z} \right] - \int_0^\infty dz J_{\nu+1}(qz) \frac{d}{dq} \frac{\tilde{f}(z, q)}{z}. \quad (6.11)$$

The conditions (6.5) and (6.6) guarantee the convergence of (6.11), but not the one of (6.8). If \tilde{f} grows so fast that the integral in (6.8) is divergent, then we *define* that integral by (6.11). Obviously, (6.11) cannot be used at $q = 0$. In appendix D we show how (6.11) can be extended to a distribution in q , with a plus-prescription and a δ distribution at $q = 0$. In the remainder of this section we consider the region $q > 0$.

Let us rewrite (6.11) such that explicit differentiation w.r.t. q is not necessary. We start by inserting

$$J_{\nu+1}(qz) = \frac{1}{q} \frac{1}{z^{\nu+2}} \frac{d}{dz} [z^{\nu+2} J_{\nu+2}(qz)] \quad (6.12)$$

into (6.11) and use integration by parts in both terms. Together with the limiting behaviour of the Bessel functions at small and large z , the conditions (6.5) and (6.6) ensure that the boundary terms vanish, so that we get

$$\begin{aligned} I(q) &= -\frac{1}{q^{\nu+1}} \frac{d}{dq} \left[q^\nu \int_0^\infty dz J_{\nu+2}(qz) z^{\nu+2} \frac{d}{dz} \frac{\tilde{f}(z, q)}{z^{\nu+3}} \right] \\ &\quad + \frac{1}{q} \int_0^\infty dz J_{\nu+2}(qz) z^{\nu+2} \frac{d}{dz} \frac{d}{dq} \frac{\tilde{f}(z, q)}{z^{\nu+3}}. \end{aligned} \quad (6.13)$$

Using the product rule for the q derivative in the first term, we get

$$I(q) = -\frac{1}{q^{\nu+1}} \int_0^\infty dz \frac{d}{dq} \left[q^\nu J_{\nu+2}(qz) \right] z^{\nu+2} \frac{d}{dz} \frac{\tilde{f}(z, q)}{z^{\nu+3}}, \quad (6.14)$$

where we have used the condition (6.7). Remarkably, terms that involve the q dependence of \tilde{f} have disappeared. In this sense, our procedure can be regarded as local in q . The two relations in (A.1) imply

$$\frac{d}{dq} J_{\nu+2}(qz) = z J_{\nu+1}(qz) - \frac{\nu+2}{q} J_{\nu+2}(qz), \quad (6.15)$$

which allows us to replace the remaining q derivative in (6.14). The result is

$$I(q) = \frac{1}{q^2} \int_0^\infty dz [2J_{\nu+2}(qz) - qz J_{\nu+1}(qz)] z^{\nu+2} \frac{d}{dz} \frac{\tilde{f}(z, q)}{z^{\nu+3}}. \quad (6.16)$$

We now use (6.12) and integrate by parts once more. The boundary terms vanish again by virtue of (6.5) and (6.6), so that

$$I(q) = \frac{1}{q^2} \int_0^\infty dz J_{\nu+2}(qz) z^{\nu+2} \frac{d}{dz} \left[\frac{2\tilde{f}(z, q)}{z^{\nu+3}} + z \frac{d}{dz} \frac{\tilde{f}(z, q)}{z^{\nu+3}} \right]. \quad (6.17)$$

This can be brought into the standard form (3.2),

$$I(q) = \frac{1}{q^2} \int_0^\infty dz J_{\nu+2}(qz) \left(\frac{1+z}{z} \right)^{\nu+2} f_1(z) \quad (6.18)$$

with

$$f_1(z) = \frac{z^\nu}{(1+z)^{\nu+2}} \left[z^2 \frac{d^2}{dz^2} \tilde{f}(z) - (2\nu+3) z \frac{d}{dz} \tilde{f}(z) + (\nu+3)(\nu+1) \tilde{f}(z) \right], \quad (6.19)$$

where from now on we drop the q dependence of \tilde{f} again, as we do in the rest of this paper. With the conditions in (6.5), the function f_1 is finite or zero at the integration boundaries, so that the integral (6.18) exists in the usual sense and can be evaluated using our adaptation of Levin's method in (3.2) and (3.3).

Discretisation. For discretising the integrand, we introduce the scaled function

$$g(z) = \left(\frac{z}{1+z} \right)^\nu \frac{\tilde{f}(z)}{(1+z)^2}, \quad (6.20)$$

which according to (6.5) is finite or zero at the integration boundaries. Inserting this into (6.19), we get

$$\begin{aligned} f_1(z) &= \left(z \frac{d}{dz} \right)^2 g(z) - 2 \left[\nu + \frac{\nu+2}{1+z} \right] z \frac{d}{dz} g(z) \\ &\quad + \left[\nu^2 - 1 + \frac{(2\nu+1)(\nu+2)}{1+z} + \frac{(\nu+1)(\nu+2)}{(1+z)^2} \right] g(z). \end{aligned} \quad (6.21)$$

For the variable transform from z to u used for discretisation, we require that

$$z \frac{du}{dz} \xrightarrow{z \rightarrow \infty} 0, \quad (6.22)$$

which is fulfilled for all cases in table 1. This allows us to approximate the derivatives in (6.21) using Chebyshev interpolation:

$$z \frac{d}{dz} g(z) \Big|_{z=z_j} \approx \sum_k D_{jk}^{(1)} g(z_k), \quad \left(z \frac{d}{dz} \right)^2 g(z) \Big|_{z=z_j} \approx \sum_k D_{jk}^{(2)} g(z_k), \quad (6.23)$$

with

$$D_{jk}^{(1)} = z_j \frac{du}{dz}(z_j) D_{jk}^u, \quad D_{jk}^{(2)} = \sum_l D_{jl}^{(1)} D_{lk}^{(1)}. \quad (6.24)$$

In close analogy with (3.25), we can thus use (6.21) to compute $f_1(z_j)$ by multiplying $g(z_k)$ with a matrix. This matrix depends only on ν and the interpolation grid and can hence be precomputed.

Generalisation. We note that using the relation

$$J_\nu(qz) = \frac{1}{z^j} \frac{1}{q^\nu} \left(\frac{1}{q} \frac{d}{dq} \right)^j [q^{\nu+j} J_{\nu+j}(qz)] \quad (6.25)$$

with a suitable value of j , it is straightforward to generalise the previous method to functions \tilde{f} growing like $z^{3/2}$ or faster as $z \rightarrow \infty$. We checked explicitly that with $j = 2$ and two steps of integration by parts, one obtains a representation of (6.8) as an integral over $J_{\nu+3}(qz)$ times a function depending on $(d/dz)^k \tilde{f}$ with $k = 0, 1, 2, 3$.

6.2 Numerical accuracy

The evaluation of the integral (6.18) using the discretised version of (6.20) and (6.21) is implemented as a separate class for “special integrals” in BESTLIME. The integration is performed using the J_ν call of the standard Bessel integrator of the library.

The timing of integration calls for the special integrator agrees within 10% with the timing of $J_{\nu-1}$ calls for the standard integrator. This is plausible, because in both cases the discretised integrand is multiplied by a matrix for differentiation, before being passed to the algorithm that implements Levin’s method.

Let us investigate the accuracy of our method for the functions $\tilde{f}(z) = z \ln^k(z^2 Q^2/b_0^2)$, which form a basis of the fixed-order perturbative expression (6.4). The constant b_0 is defined in

(5.7) and gives a simpler form of the Fourier-Bessel transform. The exact result for $I(q)$ at $q > 0$ is readily obtained by evaluating (6.11) analytically, which can be done using

$$(\ln z)^k = (d/dz)^k z^\mu \Big|_{\mu=0} \quad (6.26)$$

and

$$\int_0^\infty dz J_{\nu+1}(qz) z^\mu = \frac{\Gamma(\frac{\nu}{2} + \frac{\mu}{2} + 1)}{\Gamma(\frac{\nu}{2} - \frac{\mu}{2} + 1)} \frac{2^\mu}{q^{\mu+1}}. \quad (6.27)$$

Explicit results can also be found in [25, appendix C]. In the following, we set the hard scale to $Q = 100$ GeV.

We find that for $k \leq 4$, quite good integration accuracy can be achieved with the `inv pow` transformation that we already used for the benchmark integrals in section 4.2. For higher powers of the logarithm, the results become however increasingly inaccurate unless one takes a very large number of grid points. A much better performance for all k is obtained with the `log pow` transformation in table 1. For $\nu = 0$ and k up to 8 (corresponding to a perturbative calculation up to α_s^4 in the TMD context), we take a

$$\text{log pow grid with } [0, 0.05, \infty]_{(n_1, n_2)}, \quad \alpha = 0.2, \quad z_{\text{lo}} = 10^{-8}, \quad z_{\text{hi}} = 0.1 \quad (6.28)$$

and

$$(n_1, n_2) = \begin{cases} (16, 32) & \text{for } k = 1, 2, 3, 4, \\ (32, 48) & \text{for } k = 5, 6, 7, 8, \end{cases} \quad (6.29)$$

where the transformation parameters and the subinterval division have been determined by a parameter scan similar to the one presented in section 5.2.3. The resulting integration accuracy is shown in figure 15a and 15b. We plot the accuracy only up to $q = 90$ GeV, because for some values of k the integrals have a zero crossing near $q = 100$ GeV.

In figure 15c and figure 15d we show that our method also works well for $\nu > 0$. The grid used for these cases is a

$$\text{log pow grid with } [0, 0.1, \infty]_{(24, 48)}, \quad \alpha = 0.25, \quad z_{\text{lo}} = 5 \times 10^{-7}, \quad z_{\text{hi}} = 0.1. \quad (6.30)$$

We note that with increasing order ν of $J_\nu(qz)$, the region close to $z = 0$ is increasingly suppressed in the integral, so that a single grid setting for different ν is a compromise to some extent.

The derivation of our master formulae (6.18) and (6.19) is of course also valid if the original integral (6.8) is convergent. In this case, we can compare the respective performance of our standard method from section 3 and of the method developed here. This is done in figure 16 for the toy TMD specified in (5.12) to (5.14). Shown is the accuracy for the “special integrator” described in the present section and for the $J_{\nu-1}$ call of our standard integrator. The curves in figure 16b are for an integral involving $J_1(qz)$, so that we can also compare with the J_ν call of our standard integrator. Whilst we see no pronounced difference in performance at intermediate q values, there is some trend for the special integrator to be slightly less precise at very small or very large q . This may be due to the fact that two numerical derivatives are taken in that case. The results in figure 16 are for an

$$\text{exp sqrt grid with } [0, 0.05, \infty]_{(16, 32)}, \quad m = r_\kappa \kappa, \quad r_\kappa = 4, \quad (6.31)$$

which coincides with our default settings in (5.15) to (5.17) except for the value of r_κ . With our default choice $r_\kappa = 3$, the discrepancy between the special and standard integrators becomes even larger at small q . A more thorough comparison between the methods should cover a broader range of integrands and allow different grid settings for the different methods. We do not pursue this here, because the main purpose of the special integrator is to evaluate integrals that cannot be handled with the standard one.

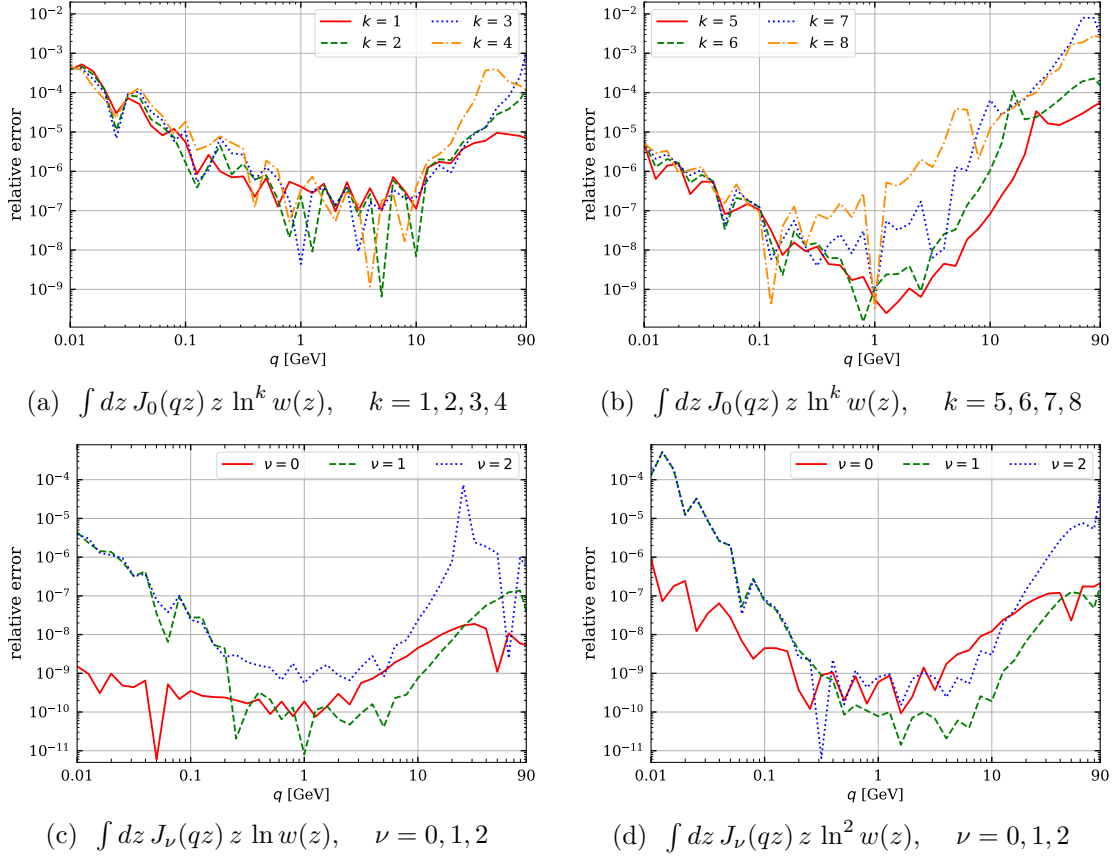


Figure 15: Relative accuracy of the integral (6.8) evaluated via (6.18) and (6.19) for different functions. The integrands are specified in the legends, where we abbreviate $w(z) = (zQ/b_0)^2$. The grid settings are specified in the text.

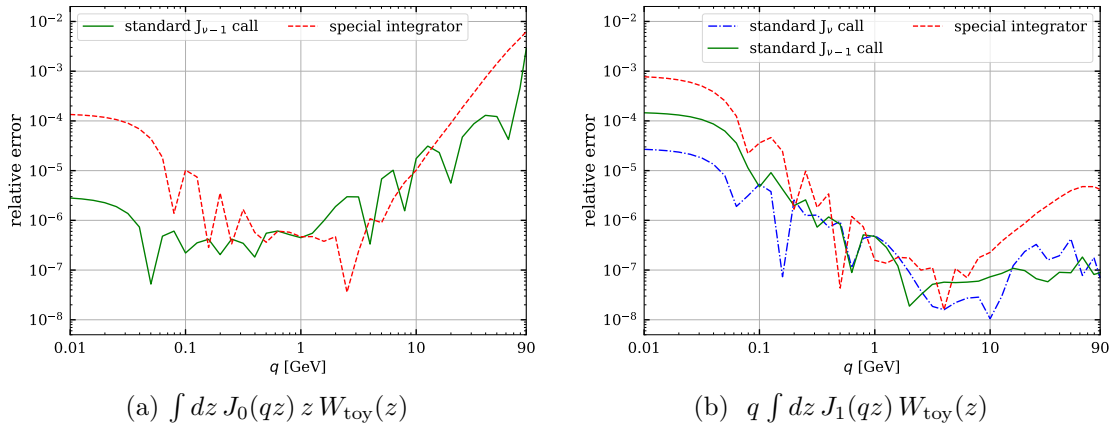


Figure 16: Comparison of the accuracy obtained with different integration methods for the q spectrum (left) and the cumulative q spectrum (right) of the cross section computed with the toy TMD in (5.12). More detail is given in the text.

7 Summary

We have presented a method to compute Fourier-Bessel transforms, $\int dz J_\nu(qz) \tilde{f}(z)$, with z ranging from 0 to ∞ or being restricted to a smaller interval. The method works for general index $\nu \geq 0$ of the Bessel function. The function $\tilde{f}(z)$ may be non-analytic at $z = 0$ (details are given in section 3.1), and for $z \rightarrow \infty$ it should decrease or tend to a constant.

Our method is a modification of an algorithm by Levin [13]. For $\nu \geq 1$ the integration problem is transformed to the system of ODEs given in (3.4), and integration by parts provides access to Bessel functions of order $\nu < 1$ as specified in (3.5). The system of ODEs is solved by collocation, with Chebyshev polynomials in a transformed variable $u(z)$ as basis functions. The resulting matrix equation is handled with standard linear algebra methods. The derivative required for integration by parts is evaluated by approximating $\tilde{f}(z)$ with the same Chebyshev polynomials. As a complement, we use Clenshaw-Curtis quadrature in z intervals where qz does not exceed the first zero of $J_\nu(x)$. This avoids most of the cases in which this matrix equation is poorly conditioned, so that its solution would require a numerically expensive singular value decomposition. The details of our algorithm are laid out in section 3.3 and implemented in the C++ library BESTLIME, which can be downloaded from [16].

The method requires a number of presets to be decided by the user. The first one is a variable transform $u(z)$ that maps the integration interval in z onto a finite interval in u and should be adapted to the large- z behaviour of $\tilde{f}(z)$. The z -grid on which $\tilde{f}(z)$ must be evaluated is then specified by the number of points, with the possibility of dividing the total integration range into several subintervals. As we have shown, such a subdivision is beneficial for both the accuracy and the computational cost of integration. This set of choices is admittedly more involved than for other methods (the Ogata method [5] for instance requires a step parameter h and the total number N of function evaluations). On the other hand, we found that with about 50 to 80 grid points, a high integration accuracy can be reached for a wide range of grid parameters and over a wide range of q , so that a detailed tuning of the grid settings should in general not be necessary. Settings that we found to be satisfactory are given in section 4.2 for a wide class of functions, and in equations (5.15) to (5.17) for integrands appearing in TMD cross sections.

In fixed-order perturbative TMD calculations one encounters functions $\tilde{f}(z)$ that grow with z , such that the corresponding Fourier-Bessel integrals do not converge. As shown in section 6 and appendix D, these integrals can be defined in the distributional sense, and their regular parts at $q > 0$ can be rewritten such that they can be evaluated numerically with our method. We obtain good accuracy for $\tilde{f}(z) = z \ln^k z$ with k up to 8, which is the highest power appearing at order α_s^4 .

As explained in section 3.3, our method is most efficient for computing Bessel-weighted integrals of several functions $\tilde{f}(z)$ at the same value of q . Changing the value of q requires somewhat more computation time for linear algebra manipulations, but does *not* necessitate a new evaluation of the function(s) $\tilde{f}(z)$, since the grid in z does not depend on q . This presents an important advantage if the function $\tilde{f}(z)$ is expensive to compute. In an ongoing separate project, we found that computing two-fold Fourier-Bessel transforms $\int dz_1 \int dz_2 J_{\nu_1}(q_1 z_1) J_{\nu_2}(q_2 z_2) \tilde{f}(z_1, z_2)$ can be done accurately and efficiently with the implementation of our method in BESTLIME.

Acknowledgements

It is a pleasure to thank Frank Tackmann, Alexey Vladimirov, and Pavel Nadolsky for useful discussions. The implementation of our method in BESTLIME is heavily drawing on the CHILIPDF library [18,19], which is under development. We gratefully acknowledge the contri-

butions of our collaborators Florian Fabry, Peter Plöfl, Riccardo Nagar, and Frank Tackmann to that project. Special thanks go to Riccardo Nagar and Frank Tackmann for their consent to releasing the present code before a full release of CHILIPDF.

This work is in part supported by the Deutsche Forschungsgemeinschaft (DFG, German Research Foundation) – grant number 409651613 (Research Unit FOR 2926) and grant number 491245950. O.G. is supported by the German Academic Scholarship Foundation.

A Useful relations for Bessel and Lommel functions

In this appendix, we collect results about Bessel and Lommel functions that are used in the main body of our work.

A.1 Bessel functions

The properties of Bessel functions are well documented in the literature. The following relations can for instance be found in [27, Chapter 10].

Relations. Functions of different order are related by

$$\begin{aligned} Z_\nu(x) &= \frac{x}{2\nu} \left[Z_{\nu-1}(x) + Z_{\nu+1}(x) \right], \\ \frac{d}{dx} Z_\nu(x) &= \frac{1}{2} \left[Z_{\nu-1}(x) - Z_{\nu+1}(x) \right], \end{aligned} \quad (\text{A.1})$$

which implies

$$\frac{d}{dx} \left[x^\nu Z_\nu(x) \right] = x^\nu Z_{\nu-1}(x) \quad (\text{A.2})$$

and

$$\frac{d}{dx} \left[x^{-\nu} Z_\nu(x) \right] = -x^{-\nu} Z_{\nu+1}(x), \quad (\text{A.3})$$

where Z_ν stands for J_ν or Y_ν , i.e. for the Bessel functions of the first or the second kind. The two sets of functions are related by

$$Y_\nu(x) = \frac{\cos(\nu\pi) J_\nu(x) - J_{-\nu}(x)}{\sin(\nu\pi)} \quad (\text{A.4})$$

for non-integer ν . For $n \in \mathbb{Z}$, one can take the limit $\nu \rightarrow n$ of the r.h.s. to define Y_n .

Behaviour at large arguments. The leading asymptotic behaviour for $x \rightarrow \infty$ of $J_\nu(x)$ and $Y_\nu(x)$ consists of oscillations and a global decrease like $x^{-1/2}$, namely

$$J_\nu(x) \sim \sqrt{\frac{2}{\pi x}} \cos\left(x - \nu \frac{\pi}{2} - \frac{\pi}{4}\right), \quad Y_\nu(x) \sim \sqrt{\frac{2}{\pi x}} \sin\left(x - \nu \frac{\pi}{2} - \frac{\pi}{4}\right). \quad (\text{A.5})$$

Series representations. For $\nu \geq 0$ one has

$$\begin{aligned} x^\nu J_\nu(x) &= x^{2\nu} \sigma(x^2), \\ x^\nu Y_\nu(x) &= \begin{cases} \sigma(x^2) + x^{2\nu} \ln(x) \sigma(x^2) & \text{for } \nu \in \mathbb{Z}, \\ \sigma(x^2) + x^{2\nu} \sigma(x^2) & \text{for } \nu \notin \mathbb{Z}, \end{cases} \end{aligned} \quad (\text{A.6})$$

where we use our generic notation $\sigma(x^2)$ for a power series in x^2 , explained after equation (2.20).

Fourier-Bessel transform. The Fourier-Bessel transform of order ν

$$I(q) = \int_0^\infty dz z J_\nu(qz) W(z) \quad (\text{A.7})$$

is its own inverse:

$$W(z) = \int_0^\infty dq q J_\nu(qz) I(q). \quad (\text{A.8})$$

This can be expressed in terms of the closure relation

$$\int_0^\infty dq q J_\nu(qy) J_\nu(qz) = \frac{\delta(y-z)}{z}. \quad (\text{A.9})$$

Equations (A.7) to (A.9) require that $\nu \geq -1/2$.

A.2 Lommel functions

The literature about Lommel functions is much more sparse than for Bessel functions. This holds especially for the Lommel functions of the second kind, which are relevant for the discussion in section 2.3. We therefore provide some more detail here and in particular derive a representation in terms of power series. Unless explicitly mentioned, the following relations can be found in [27, Chapter 11.9] or in [28, Chapter 8.57].

The Lommel functions of the first and second kind, $s_{\mu,\nu}(x)$ and $S_{\mu,\nu}(x)$, solve the second-order differential equation

$$x^2 w''(x) + x w'(x) + [x^2 - \nu^2] w(x) = x^{\mu+1}. \quad (\text{A.10})$$

The Lommel functions of first kind are given in terms of a power series as

$$s_{\mu,\nu}(x) = x^{\mu+1} \sigma(x^2) \quad (\text{A.11})$$

and oscillate like the Bessel functions for large x . For the Lommel functions of the second kind one has

$$\begin{aligned} S_{\mu,\nu}(x) &= s_{\mu,\nu}(x) + 2^{\mu-1} \Gamma\left(\frac{\mu+\nu+1}{2}\right) \Gamma\left(\frac{\mu-\nu+1}{2}\right) \\ &\quad \times \left[\sin\left((\mu-\nu)\frac{\pi}{2}\right) J_\nu(x) - \cos\left((\mu-\nu)\frac{\pi}{2}\right) Y_\nu(x) \right]. \end{aligned} \quad (\text{A.12})$$

If $\mu + \nu$ or $\mu - \nu$ is a negative odd integer, several coefficients of the power series in (A.11) become infinite, as do the Γ functions in (A.12). The function $S_{\mu,\nu}$ can be defined by a limiting procedure in these cases, as shown in [29, Chapter 3.4] or [30, Chapter 10.73].

Relations. The Lommel functions of the second kind satisfy

$$S_{\mu,\nu}(x) = S_{\mu,-\nu}(x) \quad (\text{A.13})$$

and

$$\begin{aligned} S_{\mu,\nu}(x) &= \frac{x}{2\nu} \left[(\mu + \nu - 1) S_{\mu-1,\nu-1}(x) - (\mu - \nu - 1) S_{\mu-1,\nu+1}(x) \right], \\ \frac{d}{dx} S_{\mu,\nu}(x) &= \frac{1}{2} \left[(\mu + \nu - 1) S_{\mu-1,\nu-1}(x) + (\mu - \nu - 1) S_{\mu-1,\nu+1}(x) \right], \end{aligned} \quad (\text{A.14})$$

which implies

$$\frac{d}{dx} \left[x^\nu S_{\mu,\nu}(x) \right] = (\mu + \nu - 1) x^\nu S_{\mu-1,\nu-1}(x). \quad (\text{A.15})$$

Notice the close analogy of these relations with (A.1) and (A.2). The identity

$$S_{\mu+2,\nu}(x) = x^{\mu+1} - (\mu + \nu + 1)(\mu - \nu + 1) S_{\mu,\nu}(x) \quad (\text{A.16})$$

implies that

$$S_{\nu+1,\nu}(x) = x^\nu, \quad S_{-\nu+1,\nu}(x) = x^{-\nu}, \quad (\text{A.17})$$

and by recursion

$$x^{-\nu} S_{\nu+1+2k,\nu}(x) = \sum_{j=0}^k c_{\nu,k,j} x^{2j}, \quad x^\nu S_{-\nu+1+2k,\nu}(x) = \sum_{j=0}^k c_{-\nu,k,j} x^{2j} \quad (\text{A.18})$$

for $k \in \mathbb{N}$, with coefficients $c_{\nu,k,j}$ whose explicit form we do not need.

Behaviour at large arguments. For $x \rightarrow \infty$, the Lommel functions of the second kind have an asymptotic expansion

$$x^\nu S_{\mu,\nu}(x) \sim x^{\mu+\nu-1} \sigma(x^{-2}), \quad (\text{A.19})$$

where the first term in the series σ is equal to 1. This expansion is also valid for the special cases mentioned below equation (A.12).

Series representation. As in the case of Bessel functions, we assume $\nu \geq 0$. Combining (A.6), (A.11), and (A.12), one obtains a series representation

$$x^\nu S_{\mu,\nu}(x) = \begin{cases} \sigma(x^2) + x^{\mu+\nu+1} \sigma(x^2) + x^{2\nu} \ln(x) \sigma(x^2) & \text{for } \nu \in \mathbb{Z}, \\ \sigma(x^2) + x^{\mu+\nu+1} \sigma(x^2) + x^{2\nu} \sigma(x^2) & \text{for } \nu \notin \mathbb{Z}, \end{cases} \quad (\text{A.20})$$

provided that neither $\mu + \nu$ nor $\mu - \nu$ is a negative odd integer. For these exceptional values of μ and ν , we need separate derivations. We limit ourselves to values satisfying

$$\mu + \nu > -1, \quad (\text{A.21})$$

which is sufficient for the discussion in section 2.3. This leaves us with the possibility that $\mu - \nu$ is a negative odd integer. We then can distinguish two cases:

- $\nu \in \mathbb{Z}$. Then $\mu + \nu$ is a positive odd integer, because we impose (A.21). We can therefore use the second representation in (A.18) and find that $x^\nu S_{\mu,\nu}(x)$ is a polynomial in x^2 .
- $\nu \notin \mathbb{Z}$. In this case we can use a representation derived in [29, Chapter 3.4] and also in [30, Chapter 10.73]. It has the form

$$\begin{aligned} x^\nu S_{\nu-1,\nu}(x) &= x^{2\nu} \sigma(x^2) + 2^{\nu-1} \Gamma(\nu) \left[x^\nu J_\nu(x) \ln \frac{x}{2} - \frac{\pi}{2} x^\nu Y_\nu(x) \right] \\ &= \sigma(x^2) + x^{2\nu} \sigma(x^2) + x^{2\nu} \ln(x) \sigma(x^2) \end{aligned} \quad (\text{A.22})$$

and is valid for all $\nu > 0$. Starting from this, we can repeatedly apply the recursion relation (A.16) to obtain

$$x^\nu S_{\mu=\nu-1-2k,\nu}(x) = d_{\mu,\nu} x^\nu S_{\nu-1,\nu}(x) + x^{\mu+\nu+1} \sigma(x^2) \quad \text{for } k = 1, 2, 3, \dots, \quad (\text{A.23})$$

where $d_{\mu,\nu}$ is some number and the series multiplying $x^{\mu+\nu+1}$ is in fact a polynomial.

Putting everything together, we find that one can always write

$$x^\nu S_{\mu,\nu}(x) = \sigma(x^2) + x^{\mu+\nu+1} \sigma(x^2) + x^{2\nu} \sigma(x^2) + x^{2\nu} \ln(x) \sigma(x^2) \quad (\text{A.24})$$

for $\mu + \nu > -1$ and $\nu \geq 0$. If $\mu + \nu$ is a positive odd integer, then the r.h.s. reduces to a polynomial in x^2 . Otherwise, the term with $\ln(x)$ is present if ν is an integer or if $\nu - \mu$ is a negative odd integer.

B Integrands with a Gaussian decrease in z

In section 2.3.2 we solved the system (2.16), (2.17) of differential equation for functions f_1 or f_2 with an exponential decrease at large arguments. Let us do the same for the case of functions with a Gaussian decrease. We treat the functions f_1 and f_2 in turn, since the corresponding solutions are slightly different.

We start with $f_2 = 0$ and

$$f_1(z) = c_1 z^{\mu+\nu} \exp(-\lambda^2 z^2 - \kappa z), \quad (\text{B.1})$$

where $\lambda > 0$, whilst κ may be positive, negative, or zero. With the ansatz

$$h_i(z, q) = \hat{h}_i(z, q) \exp(-\lambda^2 z^2 - \kappa z) \quad (i = 1, 3) \quad (\text{B.2})$$

the system (2.16), (2.17) of ODEs becomes

$$\begin{pmatrix} c_1 z^{\mu+\nu} \\ 0 \end{pmatrix} = - \begin{pmatrix} 2\lambda^2 z \hat{h}_1 \\ q \hat{h}_1 + 2\lambda^2 z^2 \hat{h}_3 \end{pmatrix} - \kappa \begin{pmatrix} \hat{h}_1 \\ z \hat{h}_3 \end{pmatrix} + \begin{pmatrix} d\hat{h}_1/dz + qz\hat{h}_3 \\ zd\hat{h}_3/dz - 2\nu\hat{h}_3 \end{pmatrix}, \quad (\text{B.3})$$

which can in turn be solved with the ansatz

$$\begin{aligned} \hat{h}_1(z, q) &= z^{\mu+\nu-1} \sum_{k=0}^{\infty} b_{1,k}(q) z^{-k}, \\ \hat{h}_3(z, q) &= z^{\mu+\nu-3} \sum_{k=0}^{\infty} b_{3,k}(q) z^{-k}. \end{aligned} \quad (\text{B.4})$$

We find that for each k in the sums, the first term on r.h.s. of (B.3) is leading at large z , whilst the second term is down by z^{-1} and the third term is down by z^{-2} . One can therefore solve for the coefficients recursively, starting with

$$b_{1,0} = -c_1/(2\lambda^2), \quad b_{3,0} = -qb_{1,0}/(2\lambda^2). \quad (\text{B.5})$$

We now turn to the case where $f_1 = 0$ and

$$f_2(z) = c_2 z^{\mu+\nu} \exp(-\lambda^2 z^2 - \kappa z). \quad (\text{B.6})$$

If we make again the ansatz (B.2), the system (2.16), (2.17) of ODEs takes the form

$$\begin{pmatrix} 0 \\ c_2 z^{\mu+\nu} \end{pmatrix} = - \begin{pmatrix} 2\lambda^2 z \hat{h}_1 - qz\hat{h}_3 \\ 2\lambda^2 z^2 \hat{h}_3 \end{pmatrix} - \kappa \begin{pmatrix} \hat{h}_1 \\ z \hat{h}_3 \end{pmatrix} + \begin{pmatrix} d\hat{h}_1/dz \\ zd\hat{h}_3/dz - 2\nu\hat{h}_3 - q\hat{h}_1 \end{pmatrix}. \quad (\text{B.7})$$

We now set

$$\begin{aligned} \hat{h}_1(z, q) &= z^{\mu+\nu-2} \sum_{k=0}^{\infty} b_{1,k}(q) z^{-k}, \\ \hat{h}_3(z, q) &= z^{\mu+\nu-2} \sum_{k=0}^{\infty} b_{3,k}(q) z^{-k}, \end{aligned} \quad (\text{B.8})$$

such that the three terms on the r.h.s. of (B.7) are leading, subleading in z^{-1} , and subleading in z^{-2} , respectively. One can then solve for the coefficients iteratively, starting with

$$b_{3,0} = -c_2/(2\lambda^2), \quad b_{1,0} = qb_{3,0}/(2\lambda^2). \quad (\text{B.9})$$

C Chebyshev interpolation

In this appendix, we collect formulae for Chebyshev interpolation that are relevant in our method. We use the same notation as in [18, 19], where references or derivations for the following results can be found.

We start with functions defined on the interval $[-1, 1]$, as is customary in the discussion of Chebyshev polynomials. The generalisation to any other finite interval is trivial and given at the end of this appendix.

Functions with support $t \in [-1, 1]$. The Chebyshev polynomials of the first kind, $T_k(t)$, can be defined by

$$T_k(\cos \theta) = \cos(k\theta), \quad (\text{C.1})$$

where $k \geq 0$ is an integer. Using the multiple-angle formula for the cosine, one readily verifies that $T_k(t)$ is a polynomial in t of order k . The set of all $T_k(t)$ is orthonormal with respect to the integration measure $1/\sqrt{1-t^2}$.

For a given integer N , the *Chebyshev points* are given by

$$t_j = \cos \theta_j, \quad \theta_j = \frac{j\pi}{N} \quad \text{with } j = 0, \dots, N. \quad (\text{C.2})$$

They form a descending series from $t_0 = 1$ to $t_N = -1$ and obey the reflection property $t_{N-j} = -t_j$. The polynomial $T_N(t)$ assumes its maxima $+1$ and minima -1 at the Chebyshev points, as is easily seen from (C.1). We note that the density of Chebyshev points increases from the centre toward the end points of the interval $[-1, 1]$. This feature is crucial to avoid Runge's phenomenon for equispaced interpolation grids.

The *Chebyshev interpolant* $p_N(t)$ of a function $f(t)$ is the unique polynomial that satisfies

$$p_N(t_j) = f(t_j) \quad \text{for } j = 0, \dots, N \quad (\text{C.3})$$

at the Chebyshev points t_j . It can be written in the form

$$p_N(t) = \sum_{k=0}^N \beta_k c_k T_k(t) \quad (\text{C.4})$$

with coefficients

$$c_k = \frac{2}{N} \sum_{j=0}^N \beta_j T_k(t_j) f(t_j), \quad (\text{C.5})$$

where $\beta_0 = \beta_N = 1/2$ and $\beta_j = 1$ otherwise.

For functions $f(t)$ that are sufficiently regular in the interval $[-1, 1]$ (including the end points), one can show that the difference $|f(t) - p_N(t)|$ uniformly tends to zero on the full interval in the limit $N \rightarrow \infty$. A precise statement of this convergence theorem can be found in [18, section 2]. We note that a function is *not* sufficiently regular for the purpose of this theorem if its first derivative diverges at an endpoint of the interval. This explains our insistence on a finite first derivative of h_1 and h_3 in the discussion of section 2.3.

Differentiation. Given the Chebyshev interpolant $p_N(t)$ for a function $f(t)$, one can approximate the derivative $f'(t) = df/dt$ of the function by the derivative dp_N/dt of its interpolant. Note that in general df/dt is not equal to dp_N/dt at the Chebyshev points; this is obvious because one cannot compute the exact values of $f'(t_j)$ from the discrete set of function values $f(t_j)$. At the Chebyshev points, the derivative of the interpolating polynomial can be computed as

$$\frac{d}{dt}p_N(t_j) = \sum_{k=0}^N D_{jk} f(t_k) \quad (\text{C.6})$$

with a differentiation matrix given by

$$\begin{aligned} D_{00} &= -D_{NN} = \frac{2N^2 + 1}{6}, \\ D_{jj} &= -\frac{\cos \theta_j}{2 \sin^2 \theta_j} && \text{for } j \neq 0, N, \\ D_{jk} &= \frac{\beta_k}{\beta_j} \frac{(-1)^{j+k}}{t_j - t_k} && \text{for } j \neq k. \end{aligned} \quad (\text{C.7})$$

Note that the matrix multiplication (C.6) maps a vector $f(t_k) = \text{const}$ onto the zero vector, as it must be because the derivative of a constant function is zero.

Integration. Approximating a function by its Chebyshev interpolant, one can derive an integration rule

$$\int_{-1}^1 dt f(t) \approx \sum_{\substack{k=0 \\ \text{even}}}^N \frac{2\beta_k c_k}{1 - k^2} = \sum_{j=0}^N w_j f(t_j) \quad (\text{C.8})$$

with weights

$$w_j = \frac{4\beta_j}{N} \sum_{\substack{k=0 \\ \text{even}}}^N \beta_k \frac{\cos(k\theta_j)}{1 - k^2}. \quad (\text{C.9})$$

This is known as *Clenshaw-Curtis quadrature*. A detailed discussion of its accuracy, as well as a comparison with Gauss quadrature, is given in [17, chapter 19] and in [31].

Functions with support $u \in [u_a, u_b]$. It is easy to generalise the preceding results to an arbitrary finite interval in the variable u by introducing the linear transformation

$$u(t) = \frac{u_a - u_b}{2} t + \frac{u_a + u_b}{2}. \quad (\text{C.10})$$

With the Chebyshev points

$$u_j = u(t_j) = \frac{u_a - u_b}{2} \cos \frac{j\pi}{N} + \frac{u_a + u_b}{2} \quad (\text{C.11})$$

in the new variable, we obtain the following rules for differentiation and for integration:

$$\frac{d}{du} f(u_j) \approx \sum_{k=0}^N D_{jk}^u f(u_k), \quad D_{jk}^u = \frac{2}{u_a - u_b} D_{jk} \quad (\text{C.12})$$

with D_{jk} from (C.7) and

$$\int_{u_a}^{u_b} du f(u) \approx \sum_{j=0}^N w_j^u f(u_j), \quad w_j^u = \frac{u_b - u_a}{2} w_j \quad (\text{C.13})$$

with w_j from (C.9).

D Fourier-Bessel integrals as distributions

In this appendix, we show how the formally divergent integrals discussed in section 6 can be defined in the distributional sense.

For a given ν and a function $g(q)$, we define the plus-distribution $[g(q)]_+^{q_0}$ by its action on a test function, which we require to be of the form $q^{\nu+1}\varphi(q)$:

$$\int_0^\infty dq q^{\nu+1} \varphi(q) [g(q)]_+^{q_0} = \int_0^\infty dq q^{\nu+1} [\varphi(q) - \theta(q_0 - q)\varphi(0)] g(q). \quad (\text{D.1})$$

This can also be written as

$$[g(q)]_+^{q_0} = \lim_{\epsilon \rightarrow 0} \left[\theta(q - \epsilon) g(q) - \frac{\delta(q)}{q^{\nu+1}} \int_\epsilon^{q_0} d\tilde{q} \tilde{q}^{\nu+1} g(\tilde{q}) \right], \quad (\text{D.2})$$

where it is understood that the limit $\epsilon \rightarrow 0$ should be taken *after* integrating over q with a test function. Note that the factor $1/q^{\nu+1}$ in (D.2) does not give rise to singularities because we consider test functions proportional to $q^{\nu+1}$. Alternatively, one can write $\delta(q)/q^{\nu+1} = (\nu+2)\delta(q^{\nu+2})$ and integrate over $q^{\nu+2}$ in (D.1).

If $g(q)$ decreases faster than $1/q^{\nu+2}$ at large q , then the upper integration limit q_0 in the subtraction term of (D.1) and (D.2) can be set to ∞ . Otherwise, q_0 must be finite.

For $\nu = 0$ our definition is equivalent to the one in [25, appendix C] if the latter is applied to two-dimensional test functions $\varphi(\vec{q})$ with azimuthal symmetry.

We now extend our previous definition (6.11) to the distributional form

$$\begin{aligned} I(q) &= \int_0^\infty dz J_\nu(qz) \tilde{f}(z, q) \\ &= \left[\frac{1}{q^{\nu+1}} \frac{d}{dq} K(q) \right]_+^{q_0} + \frac{\delta(q)}{q^{\nu+1}} K(q_0) - \int_0^\infty dz J_{\nu+1}(qz) \frac{d}{dq} \frac{\tilde{f}(z, q)}{z}, \end{aligned} \quad (\text{D.3})$$

where

$$K(q) = q^{\nu+1} \int_0^\infty dz J_{\nu+1}(qz) \frac{\tilde{f}(z, q)}{z}. \quad (\text{D.4})$$

Using (D.2), we can rewrite (D.3) as

$$\begin{aligned} I(q) &= \lim_{\epsilon \rightarrow 0} \left[\frac{\theta(q - \epsilon)}{q^{\nu+1}} \frac{d}{dq} K(q) + \frac{\delta(q)}{q^{\nu+1}} \left(K(q_0) - \int_\epsilon^{q_0} d\tilde{q} \frac{d}{d\tilde{q}} K(\tilde{q}) \right) \right] \\ &\quad - \int_0^\infty dz J_{\nu+1}(qz) \frac{d}{dq} \frac{\tilde{f}(z, q)}{z} \\ &= \lim_{\epsilon \rightarrow 0} \left[\frac{\theta(q - \epsilon)}{q^{\nu+1}} \frac{d}{dq} K(q) + \frac{\delta(q)}{q^{\nu+1}} K(\epsilon) \right] - \int_0^\infty dz J_{\nu+1}(qz) \frac{d}{dq} \frac{\tilde{f}(z, q)}{z}. \end{aligned} \quad (\text{D.5})$$

This makes it explicit that the dependence on q_0 cancels, as it must be. If $K(0) = 0$, one can take the $\epsilon = 0$ limit for each individual term on the r.h.s. The distributional part proportional to $\delta(q)$ then disappears, and $I(q)$ is an ordinary function.

If \tilde{f} is independent of q , one readily finds

$$\int_0^q d\tilde{q} \tilde{q}^{\nu+1} I(\tilde{q}) = K(q). \quad (\text{D.6})$$

The representation in (D.3) and (D.4) thus generalises the relation between the differential and cumulative q spectra in (5.1) and (5.2) to distributions and to $\nu \neq 0$.

As a simple illustration let us set $\tilde{f}(z) = z$ and $\nu = 0$. One then has $K(q) = 1$, and our definition (D.3) gives $I(q) = \delta(q)/q$ in agreement with (6.3).

Inverse Fourier-Bessel transform If \tilde{f} is independent of q , then (D.3) is an extension of the ordinary Fourier-Bessel transform. We now show that, in accordance with the relations (A.7) and (A.8) for ordinary functions, the Fourier-Bessel transform of $I(q)$ gives back $\tilde{f}(z)/z$, provided that

$$q^2 K(q) \xrightarrow{q \rightarrow 0} 0, \quad q^{-1/2-\nu} K(q) \xrightarrow{q \rightarrow \infty} 0. \quad (\text{D.7})$$

We do not investigate here for which functions $\tilde{f}(z)$ these conditions are satisfied, but we note that they do hold for the case $\tilde{f}(z) = z \ln^k z$ that we studied in section 6.

Taking the Fourier-Bessel transform of (D.3) and using (D.1) with $\varphi(q) = J_\nu(qy)/q^\nu$, we get

$$\begin{aligned} \tilde{I}(y) &= \int_0^\infty dq q J_\nu(qy) I(q) \\ &= \int_0^\infty dq \left[\frac{J_\nu(qy)}{q^\nu} - \theta(q_0 - q) J_\nu^{(0)} \right] \frac{d}{dq} K(q) + J_\nu^{(0)} K(q_0) \end{aligned} \quad (\text{D.8})$$

with

$$J_\nu^{(0)} = \lim_{q \rightarrow 0} \frac{J_\nu(qy)}{q^\nu} = \left(\frac{y}{2}\right)^\nu \frac{1}{\Gamma(1+\nu)}. \quad (\text{D.9})$$

Integration by parts gives

$$\tilde{I}(y) = - \int_0^\infty dq K(q) \frac{d}{dq} \frac{J_\nu(qy)}{q^\nu}, \quad (\text{D.10})$$

where the boundary terms have vanished by virtue of (D.7). Using (A.3) and (A.9), we finally obtain the desired result

$$\tilde{I}(y) = y \int_0^\infty dq q J_{\nu+1}(qy) \int_0^\infty dz J_{\nu+1}(qz) \frac{\tilde{f}(z)}{z} = \frac{\tilde{f}(y)}{y}. \quad (\text{D.11})$$

References

- [1] R. Boussarie et al., *TMD Handbook*, [arXiv:2304.03302](#).
- [2] M. A. Ebert, J. K. L. Michel, I. W. Stewart and Z. Sun, *Disentangling long and short distances in momentum-space TMDs*, *JHEP* **07** (2022) 129 [[arXiv:2201.07237](#)].
- [3] M. G. A. Buffing, M. Diehl and T. Kasemets, *Transverse momentum in double parton scattering: factorisation, evolution and matching*, *JHEP* **01** (2018) 044 [[arXiv:1708.03528](#)].
- [4] P. Cal, R. von Kuk, M. A. Lim and F. J. Tackmann, *The q_T spectrum for Higgs production via heavy quark annihilation at $N^3LL' + aN^3LO$* , [arXiv:2306.16458](#).
- [5] H. Ogata, *A numerical integration formula based on the Bessel functions*, *Publ. Res. Inst. Math. Sci.* **41** (2005) 949–970.
- [6] I. Scimemi and A. Vladimirov, *Analysis of vector boson production within TMD factorization*, *Eur. Phys. J. C* **78** (2018) 89 [[arXiv:1706.01473](#)].
- [7] J. Isaacson, Y. Fu and C. P. Yuan, *Improving ResBos for the precision needs of the LHC*, [arXiv:2311.09916](#).

- [8] Z.-B. Kang, A. Prokudin, N. Sato and J. Terry, *Efficient Fourier Transforms for Transverse Momentum Dependent Distributions*, *Comput. Phys. Commun.* **258** (2021) 107611 [[arXiv:1906.05949](https://arxiv.org/abs/1906.05949)].
- [9] N. Baddour and U. Chouinard, *Theory and operational rules for the discrete Hankel transform*, *J. Opt. Soc. Am. A* **32** (2015) 611.
- [10] N. Baddour, *The Discrete Hankel Transform*, in *Fourier Transforms – Century of Digitalization and Increasing Expectations*. IntechOpen, 2019. <https://doi.org/10.5772/intechopen.84399>.
- [11] S. Venkat, J. Arrington, G. A. Miller and X. Zhan, *Realistic Transverse Images of the Proton Charge and Magnetic Densities*, *Phys. Rev. C* **83** (2011) 015203 [[arXiv:1010.3629](https://arxiv.org/abs/1010.3629)].
- [12] D. Levin, *Procedures for computing one- and two-dimensional integrals of functions with rapid irregular oscillations*, *Math. Comp.* **38** (1982) 531.
- [13] D. Levin, *Fast integration of rapidly oscillatory functions*, *Journal of Computational and Applied Mathematics* **67** (1996) 95.
- [14] J. Li, X. Wang, T. Wang and S. Xiao, *An improved Levin quadrature method for highly oscillatory integrals*, *Applied Numerical Mathematics* **60** (2010) 833.
- [15] J. Li, X. Wang, T. Wang, S. Xiao and M. Zhu, *On an improved-Levin oscillatory quadrature method*, *Journal of Mathematical Analysis and Applications* **380** (2011) 467.
- [16] M. Diehl and O. Grocholski, *BestLime: a C++ library for computing Fourier- Bessel transforms with Levin's integration method*, 2024. [10.5281/zenodo.11113672](https://zenodo.org/record/11113672).
- [17] L. N. Trefethen, *Approximation Theory and Approximation Practice*. Society for Industrial and Applied Mathematics, 2012. <https://people.maths.ox.ac.uk/trefethen/ATAP>.
- [18] M. Diehl, R. Nagar and F. J. Tackmann, *ChiliPDF: Chebyshev interpolation for parton distributions*, *Eur. Phys. J. C* **82** (2022) 257 [[arXiv:2112.09703](https://arxiv.org/abs/2112.09703)].
- [19] M. Diehl, R. Nagar, P. Plößl and F. J. Tackmann, *Evolution and interpolation of double parton distributions using Chebyshev grids*, *Eur. Phys. J. C* **83** (2023) 536 [[arXiv:2305.04845](https://arxiv.org/abs/2305.04845)].
- [20] W. H. Press, S. A. Teukolsky, W. T. Vetterling and B. P. Flannery, *Numerical Recipes*. Cambridge University Press, Cambridge, MA, 2007. <https://numerical.recipes/book.html>.
- [21] Gaël Guennebaud and Benoît Jacob and others, *Eigen v3*, 2010. <https://eigen.tuxfamily.org>.
- [22] *GNU Scientific Library Documentation*. <https://www.gnu.org/software/gsl/doc/html/index.html>.
- [23] A. Bacchetta, F. Delcarro, C. Pisano, M. Radici and A. Signori, *Extraction of partonic transverse momentum distributions from semi-inclusive deep-inelastic scattering, Drell-Yan and Z-boson production*, *JHEP* **06** (2017) 081 [[arXiv:1703.10157](https://arxiv.org/abs/1703.10157)]. [Erratum: *JHEP* 06, 051 (2019)].

- [24] R. Piessens, E. de Doncker-Kapenga, C. Überhuber and D. Kahaner, *QUADPACK. A subroutine package for automatic integration*. Springer, 1983, [10.1007/978-3-642-61786-7](https://doi.org/10.1007/978-3-642-61786-7).
- [25] M. A. Ebert and F. J. Tackmann, *Resummation of Transverse Momentum Distributions in Distribution Space*, *JHEP* **02** (2017) 110 [[arXiv:1611.08610](https://arxiv.org/abs/1611.08610)].
- [26] P. M. Nadolsky, *Multiple parton radiation in hadroproduction at lepton hadron colliders*, Ph.D. thesis, Michigan State U., 2001. [arXiv:hep-ph/0108099](https://arxiv.org/abs/hep-ph/0108099).
- [27] F. W. J. Olver, A. B. Olde Daalhuis, D. W. Lozier et al., *NIST Digital Library of Mathematical Functions*. Release 1.1.12 of 2023-12-15. <https://dlmf.nist.gov>.
- [28] I. S. Gradshteyn, I. M. Ryzhik, D. Zwillinger and V. Moll, *Table of integrals, series, and products*. Academic Press, Amsterdam, 2014, [10.1016/C2010-0-64839-5](https://doi.org/10.1016/C2010-0-64839-5).
- [29] Y. L. Luke, *Integrals of Bessel Functions*. McGraw-Hill, New York, 1962. Reprinted in 2014.
- [30] G. N. Watson, *A Treatise on the Theory of Bessel Functions*. Cambridge University Press, Cambridge, UK, 2nd ed., 1944. Reprinted in 1995.
- [31] L. N. Trefethen, *Is Gauss Quadrature Better than Clenshaw-Curtis?*, *SIAM Review* **50** (2008) 67.